HERA Luminosity Upgrade

W. Bartel[b], E.Gianfelice[b], N.Holtkamp[a], E. Lohrmann[a], J. Maidment[b], B.Parker[b], D.Pitzl$c$, F. Willeke[b], HERA-Zeus Upgrade Group[b],

[a] Universität Hamburg
[b] Deutsches Elektronen-Synchrotron DESY, Notkestrasse 85, D-22603 Hamburg, FRG
[c] Inst. for Particle Physics, ETH— Zürich,

Abstract: Ways to increase the luminosity of HERA beyond the design luminosity of $L = 1.5\ 10^{31} cm^{-2} sec^{-1}$ have been explored and investigated: A new design of the interaction region and upgrade of the injector chain. Most promising appears to be a redesign of the IR based on new types of septum magnets. This promises to increase the luminosity by a factor of four if beam deflection and focusing components are integrated in the colliding beam detector. The consequences of such elements for the detectors have been studied.

Contents

1 Introduction

by E. Lohrmann

1.1 Luminosity Upgrade

The HERA e-p storage ring started operating in June 1992. Since then the delivered luminosity has been steadily increasing: The integrated luminosities were $1pb^{-1}$ in 1993,$6pb^{-1}$ in 1994 and 12 pb-1 in 1995 In 1995 a peak luminosity of $L_{peak} = 7 \cdot 10^{30}/cm^2/s$ has been reached,to be compared with the design luminosity of $1.5 \cdot 10^{31}/cm^2/s$. At beam currents of up to $30mA$ for electrons and $55mA$ for protons,the specific luminosity is about two times larger than the design value. As circulating currents increase, there is therefore a very good prospect to reach or slightly surpass the design luminosity. In addition, other improvements in the machine will lead to an increase of the efficiency, so that in the end the machine could deliver an estimated integrated luminosity of $40 - 50pb^{-1}/year$, leading to $200 - 250pb^{-1}$ in a reasonable running time. So far about $20pb^{-1}$ have been collected.

The experiments H1 and ZEUS have made good use of this luminosity. So far,for luminosity reasons,mostly phenomena at values of $Q^2 << M(W)^2$ have been explored,which allows a wide range of studies of QCD. Important results so far are the accurate measurement of F_2,the structure function of the proton, covering four orders of magnitude in both x and Q^2. Its Q^2 dependence can be described in terms of the GLAP evolution equations,which is a big step forward in the understanding of the proton. The large center of mass energy of HERA has also allowed a new look at diffraction, because its spacelike structure can be investigated in great detail.

A number of new QCD tests add to prove HERA a 'QCD-machine'. These results have attracted wide attention. A large international community of experimental physicists from 15 countries have driven this program vigorously,and encouraged by the QCD physics results, have improved the capabilities of the detectors for this type of physics. It must however be noted that this is 'low Q^2 -physics' compared with the electroweak scale of $Q^2 = M(W)^2$. The physics on the electroweak scale has so far been barely touched. This is the region HERA was built to explore. The unique features of HERA,like electron polarization and the capability to compare electron and positron running are relevant only in the electro-weak regime. New important tests of EW interactions will have to be done; in addition new phenomena outside the standard model are more likely to appear.

Whereas the LEP experiments have explored the standard model for time-like momentum transfers up to $Q^2 \geq 8000GeV^2$, HERA will look into space-like momentum transfers for $Q^2 \geq 10000GeV^2$. This work has not really begun and it needs large luminosity. So far H1 and ZEUS have each accumulated about charged current (CC)-events, which are characteristic EW interactions. This is to be compared with the number of events available in 'low Q^2' physics for the F_2 studies, which is of order of 0.5 Mio events. An integrated luminosity of $200pb^{-1}$ will give about 4000 CC events, which is still not a large number. In addition, increasing the luminosity will enhance the discovery potential of the machine. Since one investigates effectively electron-quark collisions, and since the quarks have their momentum distributed up to the proton momentum, an increase in luminosity makes statistically larger cm energies available. The effective center of mass energy increases about like $(luminosity)^0.25$. E.g. an increase of luminosity by a factor 4 beyond design will effectively increase the cm energy of the machine from 300 GeV to 420 Gev,and by the same factor increase the mass range which can be probed for discoveries.

All these questions have been studied in great detail in this workshop. They provide a strong motivation to operate HERA at the largest possible luminosity. In addition, the Scientific Council of DESY has, in its session of February 20, 1996, given a strong endorsement for a program of luminosity increase. The following measures are considered to increase the integrated luminosity:

i improve the efficiency of operation

ii improve the emittance of the proton beam by a new proton preaccelerator

iii decrease the beta function at the interaction point

Measures i) and ii) will allow to make optimum use of the machine in its present configuration. Measure iii) can potentially increase the luminosity by another factor 3-4. However, it will involve changes also in the experiments. It requires to position beam deflecting and focusing elements as close to the interaction point as possible. The scheme proposed here requires the beam elements to be placed well inside the H1/ZEUS experiments. Apart from the need to provide the investment and planning for this project, it will require nontrivial changes in these experiments. In addition it will impair certain instrumental capabilities which have been built to investigate 'low Q^2' physics. For example the beam telescopes,which measure protons and neutrons at very small angles, will remain important, and one would like to keep as much of their capability as possible in the new luminosity scheme.

Because of this interrelation of machine- and experiment issues, a joint design team has to work out the details of the proposed scheme. This should be the next step following this workshop.

1.2 Proton Beam Polarization

If polarized proton beams could be stored, this would, in conjunction with polarized electrons, open a number of novel studies of the spin structure of the proton. The physics potential has been studied in detail in this workshop. Accelerating and storing polarized protons in HERA is exceedingly difficult.Progress has been achieved by the studies of the Spin Collaboration, however it is presently not possible to assess realistically the feasibility and the cost of such a development project. The interest of the physics program with such a facility will have to be weighted against the large technical difficulties. If this looks favorable, it would encourage further studies.

1.3 Light and Heavy Ions in HERA

The physics case for storing deuterium and heavier ions in HERA has been studied in detail in this workshop.Deuterium is interesting, because it allows to study the neutron structure, required to obtain a complete picture of the structure of the nucleon.Storing heavy nuclei would open the way to novel studies of nuclear matter.The physics interest here calls for storing relatively heavy nuclei.

It is in principle possible to store nuclei with Z=A/2. In general, the luminosity will decrease with increasing atomic number A. The changes required in the machine are relatively straightforward. They have not been worked out in great detail, but rough studies indicate, that the cost of the modifications will be appreciable. No schedule for such an upgrade is set at the present time.

2 HERA Luminosity Upgrade Potential

by F. Willeke

2.1 General Remarks

The HERA electron proton collider is the first accelerator of its kind. Two species of charged particles which are stored in two different accelerator rings are brought into collisions. The accelerator is designed for the collisions of $30GeV$ electrons or positrons with $820GeV$ protons. Maximum beam currents are $58mA$ and $160mA$v respectively. Since no experience on such collisions was available, the HERA designers were conservative in the choice of the basic beam parameters and in the layout of the accelerator lattice. This was considered necessary to provide flexibility in case of unexpected difficulties with the collisions of unequal species.

The layout of the interaction point was a particular concern of the designers. They were faced with a number of difficulties and constraints. First, the luminosity depends on the beam size at the interaction point (IP). This is limited by aperture and by chromatic effects of the low β-quadrupole magnets. The beam size thus can only be made small by putting the low-β quadrupoles close to the IP. However, it is obvious that the two beams have first to be separated after collisions before focusing elements for the high energy proton beam can be placed. Thus a quick beam separation is important for high luminosity. But quick separation requires considerable magnetic fields which lead to strong synchrotron radiation from the lepton beam. This is a potential large source of backgrounds for the colliding beam detectors. A number of additional constraints had to be taken into account. The unavoidable dispersion generated in the separators had to be kept to a minimum to avoid strong synchro-betatron coupling by dispersion in the close-by rf cavities. Furthermore, the IR-straight section had to be made spin-transparent to allow for longitudinally polarized lepton beams.

To achieve small proton beam sizes at the IP is thus difficult. The beam sizes of the two beams have to be matched at the IP in order to limit the non-linearity of the beam-beam interaction seen by the proton beam. Given the rather small HERA lepton beam emittance, it turns out to be rather easy to adapt the lepton beam to whatever can be achieved by the protons. The HERA luminosity is thus limited by the ability to strongly focus the proton beam at the IP.

The compromise found between the various constraints to place the first focusing elements for the proton beam at a distance of $22m$ from the IP which allowed for β-functions of $\beta_x^* = 10m$ and $\beta_y^* = 1m$ at the IP. With the normalized beam emittance of $\varepsilon\gamma = 5\pi mradmm$ and the beam intensity of 10^{11} protons per bunch which was expected from the proton injector chain and the maximum lepton current of $I_e = 58mA$ which is limited by the installed rf power of $10.5MW$ a peak luminosity of

$$L_{peak} = 1.5 \cdot 10^{31} cm^{-2} sec^{-1} \tag{1}$$

was expected for HERA.

Experience of four years of colliding beam operation of HERA led to the following conclusions: The synchrotron radiation background in HERA is well tolerable if the beams and collimator positions are well tuned. The main source of residual synchrotron radiation background comes from tip-scattering from the upstream synchrotron radiation masks. Thus if the upstream synchrotron radiation masks could be avoided, a considerably larger amount of synchrotron radiation generated in the interaction region could be tolerated. This means that the beams could be separated more quickly, low β-quadrupoles for the protons could be placed closer to the IP and the luminosity could be increased by smaller β-functions of the protons at the IP. This is accomplished by separator magnets which are twice as strong as the present ones but which are placed inside the detector close to the IP. Then, the synchrotron radiation will pass through the IR and can be absorbed further downstream. No upstream masks need to placed and one only has to worry about backscattering form the downstream masks.

A second conclusion may be derived from recent HERA experience. The maximum tolerable beam-beam tuneshift levels assumed for the e-p collider in the original design are probably too conservative. As long as the proton beam size is well matched to the size of the lepton beam, the proton beam lifetime in collision is more than $100 hours$ and the background from lost protons in the IR is low. The beam-beam tuneshift of the lepton beam is also rather low and might be further increased. Therefore, a brighter proton beam from the injector chain would also help increasing the HERA luminosity.

Consequently, the present study concentrates on two upgrade projects:

- Redesign of the interaction regions with stronger and earlier beam separation in order to further reduce the β-functions of the proton beam.
- Study of the benefit and of the possibilities of increasing the injection energy of the DESYIII proton synchrotron in order to obtain brigher proton beams.

2.2 HERA Performance 1992-1995 and its Limitations

After commissioning in 1991, HERA started to deliver e-p luminosity to the colliding beam experiments H1 and ZEUS in 1992. Since its first year of running, the performance of HERA was steadily improved and the integrated luminosity could be increased by large factors from year to year. The maximum bunch intensity of the proton beam was always limited by the performance of the injector chain and losses in the beam transfer line. Furthermore, the proton beam lifetime in HERA during the 30min injection period and during the early part of the ramp is critical. Usually, the total amount of beam lost in HERA is 10%. Meanwhile, the DESYIII booster synchrotron, where the intensity and the brigthness of the proton beam is limited by space charge effects at injection energy operates at design parameters of 10^{11} protons per bunch and normalized beam emittances of $\varepsilon \cdot \gamma = 8\pi mradmm$ (90% of the beam). The PETRA accelerator has been steadily improved and is now able to deliver routinely about $80mA$ of beam which corresponds to $6 \cdot 10^{10}$ protons per bunch, 60% of the design value. The transfer between HERA and PETRA suffers from the small aperture available in the $40GeV$ proton beam line with a transfer efficiency of at most 90%. About 5% of the beam loss occurs during injection into HERA. From the remaining intensity another 5% is lost due to a beam lifetime of about $3hours$ while HERA is waiting during the 20min filling procedure. The losses during acceleration are usually small. As a result, presently $65mA$ which is $4.5 \cdot 10^{10}$ protons per bunch (180 bunches) can be made available for e-p collisions on average which is about 45% of the design value.

The intensity of the lepton beam suffered in the case of electrons from a breakdown of the beam lifetime due to interactions of the beam with the ion pumps. This problem disappeared when operation was switched to positrons. The beam intensity at this point is limited at about $45mA$ by rf power and reliability constraints. Thus the HERA intensity limitations are well understood. There are not of fundamental nature and measures are being taken for a step-by-step improvement programme.

The beam dimensions at the interaction points of both proton and electron beams are smaller than the desing values. In both accelerators it was possible to give up safety margins in the apertures which allowed for stronger focusing and smaller β-functions at the IP. The β-functions achieved sofar are $\beta^*_{xp} = 7m$; $\beta^*_{yp} = 0.7m$; $\beta^*_{xe} = 1m$; $\beta^*_{ye} = 1m$ which reduces the beam sizes by about 30% of the design. The fact, that the proton beam intensity is still below design has the side effect, that the proton beam emittance is also below design. Usually emittances smaller than $\varepsilon_N = 20\pi mrad\ mm$ can be achieved in HERA in luminosity operation. This is the reason why the specific luminosity is in excess of the design value by almost a factor of two and it gives luminosity peak values of $L_{peak} = 7 \cdot 10^{30} cm^{-2} sec^{-1}$, which is half the design values despite the low beam intensity.

The stability of both beams in collision is very good. This is true in particular for the protons where the beam lifetime during luminosity operation is in the order of several hundreds of hours and there is very little emittance growth ($\dot{\varepsilon}_N/\varepsilon_N = 0.03/hour$). This however requires well matched beam sizes at the IP in order to avoid an enhancement of the nonlinearity of the beam-beam interaction. Under these conditions and with beam-beam tune shifts in the order of $\Delta\nu = 10^{-3}$, the proton beam seems to be not too close to the beam-beam limit.

The stability of the positron beam is very good as well. Its lifetime is given by beam gas bremsstrahlung due to desorbed gas from the beam pipe walls. Due to unavoidable dispersion in the rf regions which are located in each of the straight sections next to the IP, synchrobetatron resonances are quite strong. They must be avoided which limits the availabe tune space. Good electron spin polarization requires a working point in between of $Q_x + 2Q_s = 0$ and $Q_x + 3Q_s = 0$ which causes the beam to blow up somewhat in collisions which causes a loss of luminosity of 10%. If the tunes are chosen far from resonances, the leptons may also be considered to be far from the beam-beam limit. The maximum tuneshift values in 1995 were around $\Delta\nu_y = 0.025$.

An important feature of HERA are the spin polarized lepton beams. Since 1995 HERA is operated with one spin rotators pair in the East straight section for longitudinally polarized beam for the HERMES experiments. The polarization degree is routinely above 60% and is not noticeably affected by the beam-beam interaction

The biggest challenge in HERA luminosity operation is to achieve reasonable reliability and availability of the total accelerator complex. On average, the time spent in luminosity operation is only 35% of the scheduled time. The rest of the time is needed for injection, ramping tuning, recovery from technical faults and trouble shooting. These results have to be compared to a maximum possible efficiency of the order of 70%.

2.3 HERA Luminosity Limitations and Constraints

The luminosity of the HERA e-p collider may be written as

$$L = \frac{N_e N_p N_B f_{rev}}{2\pi\sqrt{\sigma_{xp}^2 + \sigma_{xe}^2}\sqrt{\sigma_{yp}^2 + \sigma_{ye}^2}} \tag{2}$$

(N_p is the number of protons per bunch N_e is the number of leptons per bunch, N_B is the number of bunches, f_{rev} is the revolution frequency, $\sigma_{x,y,e,p}$ are the rms beam sizes for protons and leptons respectively). To show the limitations of the luminosity more clearly, this expression may be rewritten in terms of limited quantities and taking into account additional constraints. An important restriction is that the beam cross sections of protons and leptons have to match to limit the nonlinearity of the beam-beam interaction. This is particularly important for the proton beam to avoid emittance blow-up, bad lifetime and large backgrounds. Thus one has $\sigma_{zp}^* = \sigma_{ze}^* = \sigma_z^*$ (z denotes horizontal or vertical, p and e denote positrons or leptons respectively). Furthermore, the total beam current of the lepton beam will be always limited by the available rf power $N_e = I_e/(e \cdot N_B \cdot f_{rev})$. The number of protons per bunch will be ultimately limited by space charge effects in the injector chain. The maximum number of protons per bunch is therefore related to a maximum beam brightness N_p/ε_N. Furthermore, since the two beams have to be separated after collisions before focusing elements for the proton beam can be placed, the beam size at the IP is expected to be limited by the maximum β-function of the protons at the IR low β quadrupole magnets. Taking these considerations into account, the luminosity may be rewritten as

$$L = \frac{I_e \cdot N_p \cdot \gamma_p}{4\pi e\sqrt{\beta_{xp}^* \beta_{yp}^*}\sqrt{\varepsilon_{xN}\varepsilon_{yN}}} \tag{3}$$

One can see that the luminosity is independent of the number of bunches as long as the beam-beam tuneshift limitation of the proton beam is not touched

$$\Delta\nu_{x,y}^p = \frac{r_p I_e \sqrt{\beta_{x,y}^p}}{2\pi e f_{rev} N_B \varepsilon_N (\sqrt{\beta_x^p} + \sqrt{\beta_y^p})}. \tag{4}$$

Since we assume that we are not limited in the β-function of the lepton-beam, the e-beam-beam tuneshift can be always controlled by an appropriate choice of the lepton beam emittance. Fortunately HERA has a big built-in flexibility of focusing in the arcs.

$$\Delta\nu_{x,y}^e = \frac{r_e N_p \sqrt{\beta_{x,y}^p}}{2\pi\gamma_e\sqrt{\varepsilon_{x,y}^e}(\sqrt{\beta_x^p} + \sqrt{\beta_y^p})}. \tag{5}$$

In order to obtain polarized lepton beams, the vertical beam emittance of the lepton beam must be as small as possible. Therefore, the beam cross section at the IP will be flat ($\sigma_x \gg \sigma_y$). Under these circumstances the vertical beam size could be reduced by reducing the emittance of the protons with almost no increase of beam-beam tuneshift.

$$\Delta\nu_{x,y}^p = \frac{r_p I_e}{2\pi e f_{rev} N_B \sqrt{a}(\sigma_x + \sigma_y)} \tag{6}$$

a is a constant geometrical factor for a given lattice. Provided, that the local chromaticity created in the low β quadrupole is not becoming too large, the β-functions in the low β quadrupoles can be increased by the same factor and the β-function at the IP can be correspondingly made smaller without touching the aperture limitation. ($\varepsilon_N/\beta^* \simeq const = a$)

These considerations lead to the following conclusions: HERA luminosity can only be increased by

- reducing the β-functions at the IP by a IR geometry with the proton low-β quadrupoles closer to the IP. Improvement factors of up to four can be reached until a further reduction of the β-functions is limited by the proton bunch length.
- increasing the vertical beam brightness N_p/ε_{yN} by a reduction of the vertical beam emittance of a factor of two.

3 Study of a New Interaction Region for HERA

3.1 Parameters for Upgraded HERA Luminosity Operation

by F. Willeke

The parameters for luminosity operations for an upgraded HERA are optimized around the smallest achievable β-functions namely

$$\beta^*_{xp} = 2.1m;\ \beta^*_{yp} = 0.13m;\ \beta^*_{xe} = 0.75m;\ \beta^*_{ye} = 36m. \tag{7}$$

The value of the vertical β-function of the protons is limited by the proton bunch length. The horizontal β-function of the protons is limited by aperture and the β-functions of the lepton beam are limited by apertures and chromaticities. This will be shown in the following sections. In this study we require an aperture of $12.5\sigma_{x,y}$ for protons and leptons.

We will make the following assumptions on beam intensities, number of bunches, maximum tolerable beam-beam tune shift values and achievable beam emittances:

Electron/Positron Beam Intensity: The beam intensity in HERAe will be always limited by the available rf power. The presently installed rf power does not allow to store the design current of $58mA$ at a beam energy of $30GeV$. Therefore we plan for an 8th rf station with 14 5-cell room temperature cavities which will provide additional $1.5MW$ of rf power. With this system, the rf power will be just sufficient for storing the design current at slightly below the design energy of $30GeV$. We assume, that we will fill the machine with 180 bunches as in present operation. Some 174 are colliding bunches. Six non-colliding bunches are going to be used for background discrimination. Under these circumstances the number of positrons/electrons per bunch will be $N_e = 4.25 \cdot 10^{10}$.

Proton Beam Intensity: The DESYIII booster synchrotron is presently able to deliver a proton bunch intensity of up to $1.25 \cdot 10^{11}$ protons per bunch. Presently, the beam intensity in HERA is limited by instabilities and non-reproducibilities in PETRA and by tight apertures in the beam lines. These are no principle problems. A programme is underway to improve the proton acceleration chain. It is reasonable to assume, that the design bunch intensity of 10^{11} protons per bunch will be reached in the HERA proton ring eventually.

Proton Beam Emittance: The beam brightness N_p/ε_N is limited in DESYIII by space charge effects. The brightness of the proton beams presently exceeds the design values only slightly. We therefore think it is justified to assume the design emittance of $\varepsilon_{xN} = \varepsilon_{yN} = 5\pi mradmm$ for future HERA operation.

Electron/Positron Beam Emittance: In the old lattice, the limitation of the beam sizes at the IP is given by the limited ability to squeeze the proton beam at the IP. It will be shown below , that one can find a favorable geometry for which the vertical β function at the IP can be made as small as the bunch length. The corresponding beam size is that small, that matching the beam sizes can not be achieved by squeezing the electron β function any more unless one wants to place quadrupole magnets inside the colliding beam detector. Therefore it is necessary to make the electron beam emittance smaller by changing the lattice from 60^0 to 90^0 phase advance per FODO cell in the arcs. Under these circumstances, the emittance will be $\varepsilon_{ex} = 16.65nm\ rad$. An emittance ratio of $\varepsilon_{ey}/\varepsilon_{ex} = 0.13$ is necessary to match the vertical sizes of proton and lepton beams at the IP. This should be easily achievable.

Beam-Beam Tuneshifts: The beam-beam tune shift of the protons does not exceed $\Delta\nu_{xp} =$

	e-beam	p-beam
energy	$30 GeV$	$820 GeV$
bunch charge N	$4.18 \cdot 10^{10}$	$10 \cdot 10^{10}$
Beam Current	$58 mA$	$140 mA$
normalized emittance ε_N	$1.85 \cdot 10^{-11} m GeV^{-2}$	$5\pi \mu m\ rad$
horizontal emittance	$16.7 nmrad$	$6.1 nm\ rad$
emittance ratio	0.13	1
horizontal β at IP β_x^*	$0.75m$	$2.10m$
vertical β at IP β_y^*	$0.36m$	$0.13m$
beam size $\sigma_x \times \sigma_y$	$112 \mu m \times 28 \mu m$	$110 \mu m \times 27 \mu m$
beam-beam tune shift/IP $\Delta\nu_{x,y}$	.039, .031	.002, .0004
number of colliding bunches	174	
luminosity	$9.37 \cdot 10^{31} cm^{-2} s^{-1}$	
specific luminosity	$2.1 \cdot 10^{30} cm^{-2} s^{-1} mA^{-2}$	
luminosity increase factor	4.63	

Table 1: Parameters for Upgraded IR Lattice

0.002. This is considered within the limits. The vertical tune shift for protons is much less. The necessity to reduce the lepton beam emittance however pushes the lepton beam-beam tune shift close to $\Delta\nu_{xe} = 0.04$ which is quite a large number. It is considered to be close to the limit according to experience with other lepton colliders.

With these parameters, a luminosity of $L = 9.37 \cdot 10^{31} cm^{-2} sec^{-1}$ can be achieved. The parameters described in this section are summarized in table 3.1.

3.2 Layout of the Lattice

by F. Willeke

The purpose of a new HERA IR design is to achieve significantly smaller β-functions for protons and electrons at the IP. This is only possible if the beams are separated more quickly so that the low-β quadrupoles for the protons can be placed closer to the IP. Synchrotron radiation background generated by the beam separator magnets is the main concern if the separation field should become stronger. Since a large contribution from this background however comes from tip scattering at the upstream synchrotron radiation masks, the fields can be significantly increased if these masks can be avoided. This is the case, if the separation fields occur inside the colliding beam detectors. Then the synchrotron radiation can pass through the whole detector region without hitting an absorber. It then can be absorbed further downstream and one only has to worry about backscattered radiation.

Consequently, an agressive luminosity upgrade scheme is based on an air-coil dipole magnet inside the colliding beam detector. With an outer magnet diameter of 190mm we assume that it can be put at a distance of $1.2m$ from the IP. The magnets have a length of $L = 4.4m$ they provide a bending angle of $\theta = 8 mrad$ which corresponds to a bend radius of $\rho = 550m$. For the nominal beam energy of $E = 30GeV$, a bending field of $B = 0.182T$ is required. This fields corresponds to about the maximum field which can be achieved by an air coil magnet.

In the two separator magnets, a synchrotron radiation power of $P_{syn} = 19.2kW$ is generated. The critical energy is $E_{crit} = 109keV$. The corresponding synchrotron radiation fan must pass through the detector and the downstream magnets without striking any material. This requires quite large apertures in the separator magnet. The distance between the synchrotron radiation fan and the centre of the beam at the downstream end of the downstream separator is $90mm$. At the end of the separator magnet, the two beams are separated by $17mm$

Adjacent to the separator magnet are the focusing elements of the electron beam. The focusing is provided by a low-β doublet of conventional quadrupole magnets. These magnets are placed on the axis of the electron beam and they do not contribute to the separation dipole field and only little synchrotron radiation is generated. A speciality of these magnets is that their coils may not occupy any space in the magnet midplane in the ring-outward direction. This space must be kept free for the synchrotron radiation fan generated by the beam separation. This radiation must be absorbed further away from the IP in order to minimize the background from backscattered synchrotron radiation. The synchrotron radiation background of this arrangement will be discussed below. For the vertical low β quadrupole, a pole tip field of $B = 1\ T$ is required. The pole radius is $35mm$. The magnet $1.43m$ long and at its end, the two beams are already separated by $29mm$. The next element is the horizontal focusing quadrupole for the leptons. Since proton and lepton beams are already strongly separated, a large pole radius of $63mm$ is required to accomodate the proton beam. With a pole tip field of $B = 1\ T$ a length of $L = 2.075m$ is sufficient to provide the necessary focusing. At the end of this magnet, the beams are separated by $47mm$. The peak β-functions in this low-β-doublet are $\beta_{x-max} = 300m$ and $\beta_{y-max} = 100m$. The local chromaticity generated in this doublet is $\xi_x = -5.36$ and $\xi_y = -2.17$. The horizontal local chromaticity is quite large. It gives rise to a considerable off energy β-beat which must be carefully considered especially since a 90^0 phase advance is foreseen in the arcs. In fig 1 the proton and electron beam cross sections are shown respectively.

After $11m$ distance from the interaction point, the beams are separated by $58mm$. This is already sufficient separation for a septum-type quadrupole which focuses the protons vertically. This magnet is a new type of iron yoke half quadrupole with a cut in the mirror plate leaving only very little material between the two beams. This quadrupole allows a pole tip field of $B = 0.86\ T$. With a pole radius of $30mm$, a k-value of $k = 0.01m^{-2}$ is achieved. A length of $7.42m$ is required to provide about 65% of the necessary vertical focusing. In fig 2 the proton and electron beam envelopes are shown at the entrance of this magnet. The picture shows the countors of the half quadrupole poles and the mirror plate with the cut schematically. The rest of the vertical focusing is provided by a quadrupole with a septum coil. The electron beam passes in between the septum and the return yoke. This quadrupole has a pole radius of $r = 33mm$ and a pole tip field of $B = 1\ T$. A k-value of $k = 0.011m^{-2}$ is achieved. With a length of $L = 6.36m$, the vertical focusing is completed. At the begin of this magnets, the two beams are already separated by $122mm$ which leaves some $60mm$ thickness for the septum coil. A current density of $11amps/mm^2$ is required in this coil to generate the quadrupole field. Fig 3 shows the beam cross section at the entrance of this element. The $50mm$ wide septum coil is shown schematically. The end of this magnet is at $25.3m$ from the IP. The beams are now separated by $178mm$ so that a conventional quadrupole magnet is forseen for the horizontal focusing. This is accomplished by a ten meter long quadrupole magnet with a pole radius of

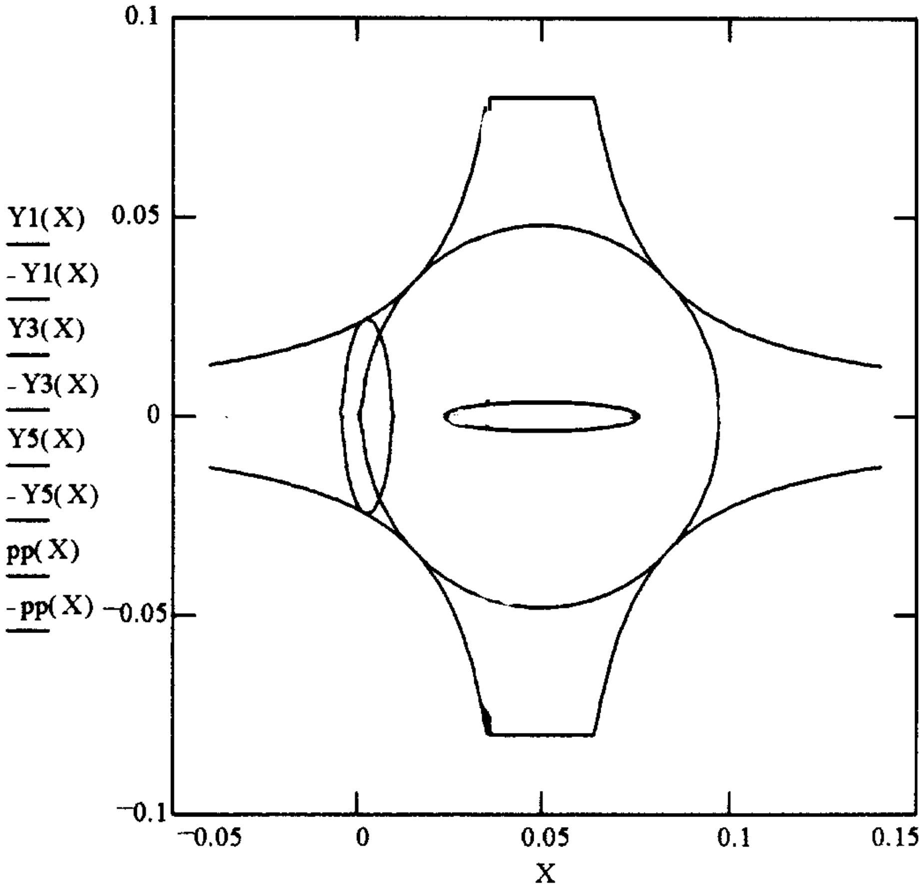

Figure 1: Beam sizes (12.5σ) at the end of the e-beam doublet.

$40mm$ and a pole tip field of 1 T. At $35.4m$ from the IP the focusing of the proton beam is accomplished. The maximum β functions in the proton low-β doublet are $\beta_{x-max} = 1807m$ and $\beta_{y-max} = 1639m$. Thus the local chromaticity generated in the doublet compares well with the values of the present HERA lattice. The apertures provide space for 12.5 rms beam sizes and thus has the same margin as the present beam optics.

A complete matching to the arc has not yet been performed. But no problems are expected here. fig 4 shows the β-function in a distance up to 50m from the IP. The geometry with the approximate dimensions of the magnetic elements (top view) is shown in fig 5 in an extended vertical scale.

In the present lattice, there is no compensation foreseen for the changing separator field if the positrons are ramped from $12GeV$ injection to the full energy. This problem can be solved in the following way: First, the proton rf frequency can be phase-locked to the electron rf at a proton beam energy of 400GeV. The two beams have then to be ramped up together to their full energy for which the geometry and the fields are matched. Since there is still a separator field mismatch at electron injection energy because the ratio of $30GeV/12GeV$ is different from $820GeV/400GeV$, some additional compensation of $\theta = 17\mu rad$ is required. This can be provided by the dipole component of the separator half quadrupole field which must be increased by 2%. The corresponding excess quadrupole magnet has to be compensated by the second vertically focusing quadrupole, which has a much smaller dipole component. The course of $beta$-functions is shown is figure 4 and a layout of the IR in extended vertical scale is

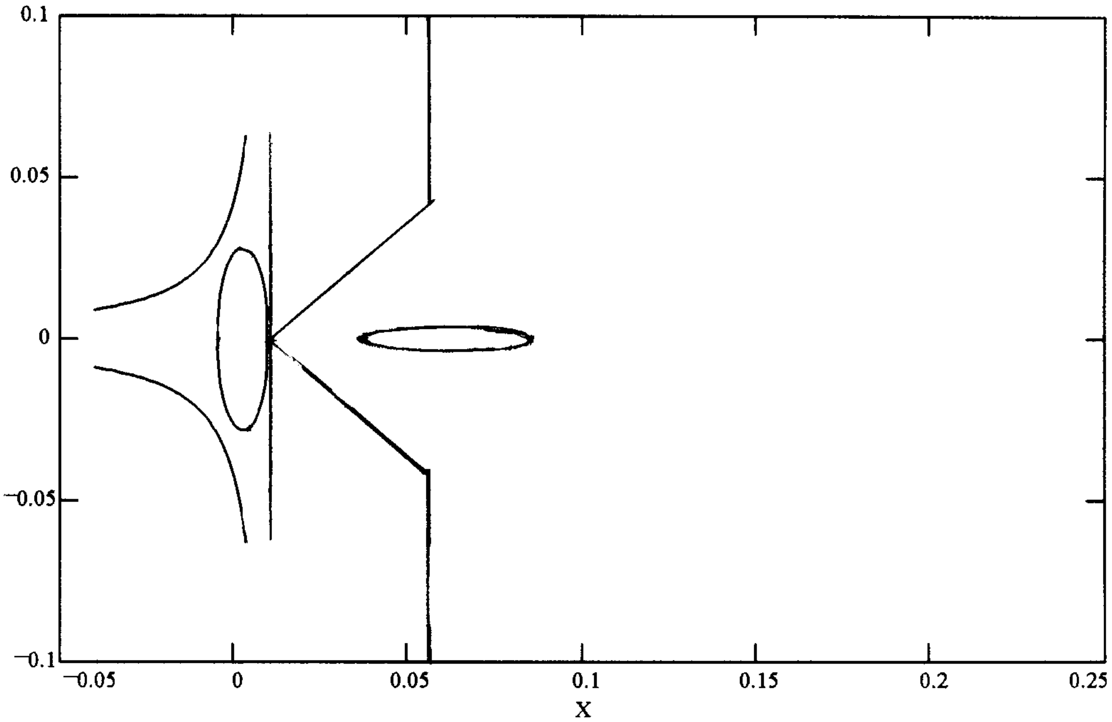

Figure 2: 12.5 σ beam sizes at the entrance of the septum quadrupole

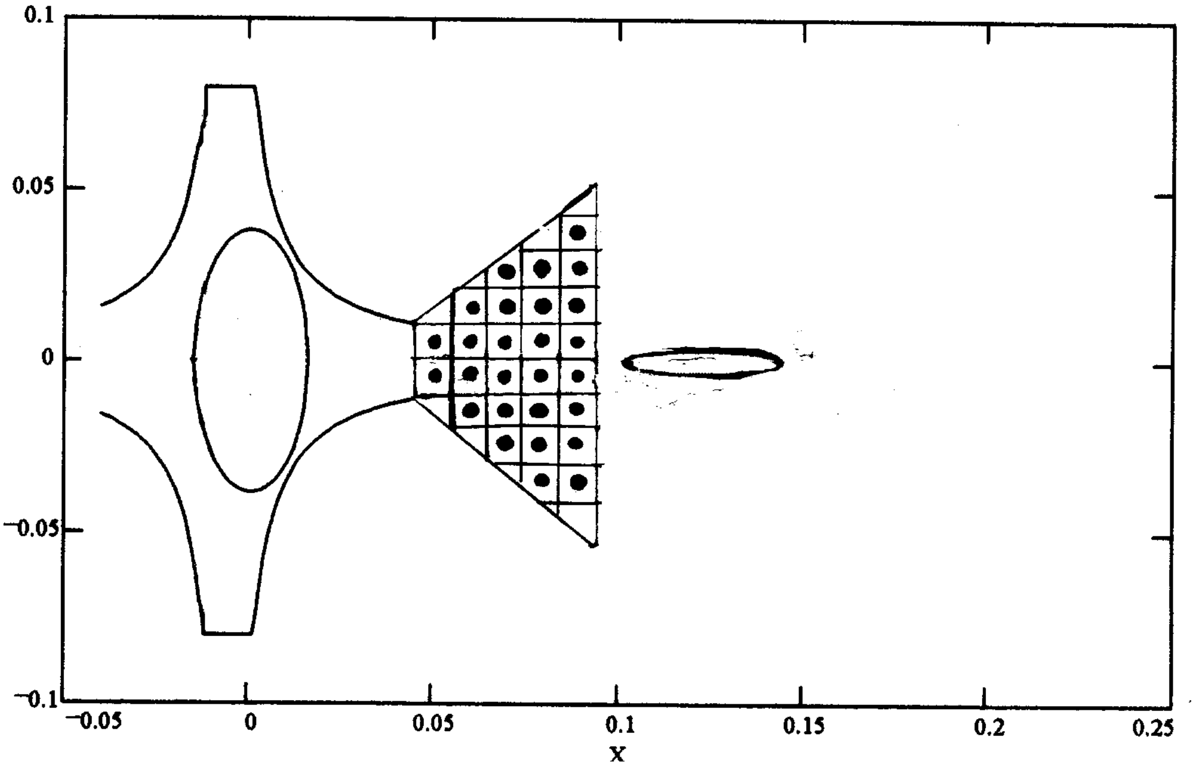

Figure 3: Beam sizes (12.5σ) at the end of the septum coil quadrupole

shown in figure 5.

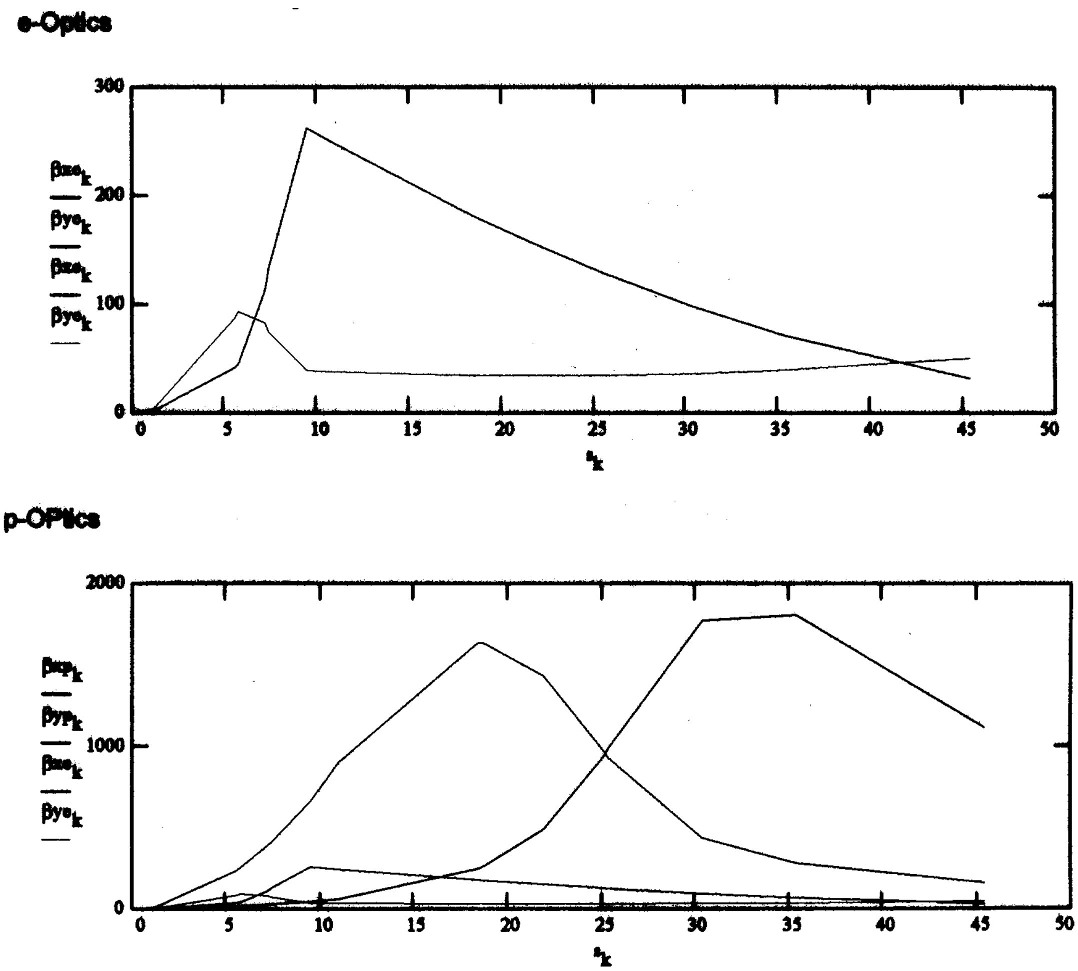

Figure 4: β-functions in meters in the IR region

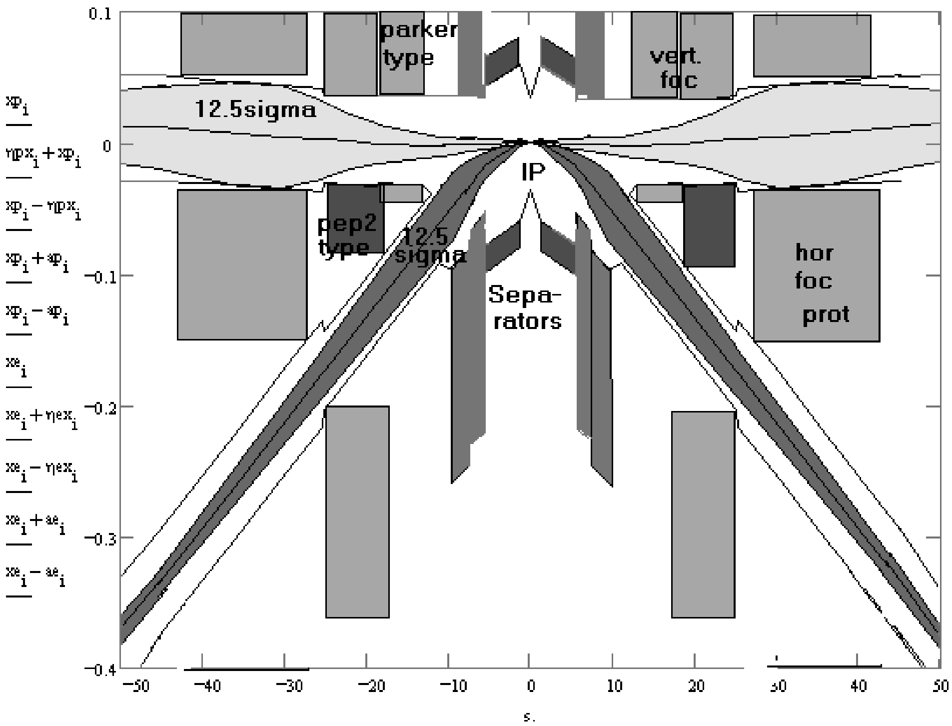

Figure 5: Geometry of the upgraded lattice in the IR. The plot shows the top view of the 12.5σ beam envelopes for proton and electron beam and the limiting magnet apertures. The IP is in the middle of the picture. The boxes represent the magnets which are starting from the IP: the separator magnet, the e-low β-quadrupole doublet, the mirror-plate septum quadrupole, the septum-coil quadrupole (both vertical focusing for protons) and the horizontally focusing quadrupole for the protons. Note that the vertical full scale is only 50cm, the horizontal scale is 100m

3.3 Improved Lattice Design Using a Combined Function Separator Magnet

by B. Parker and F. Willeke

A substantial improvement of the lattice design can be achieved by using a combined function magnet as a separator magnet. A magnet which provides some 35% of the necessary vertical low-β-focusing. A possible design of such a magnets is discussed below. The advantages of this most recent design are:

- The chromaticity of the electron beam is reduced by a large factor. Chromaticity generated in the IR is not an important issue any more.
- The field of the separator is concentrated in a volume occupied by the beam. The volume occupied by the synchrotron radiation fan has only low field. This allows a more economical magnet design.
- The particle beam enters the separator (upstream of the IP) in a high field ($\rho = 450m$). Close to the IP, the field is weaker since the beam has shifted transversely by 15mm($\rho = 650m$). This reduces the synchrotron light background for the luminosity measurement considerably.
- The coils on the ring-outside have to be replaced to produce a quadrupole field. This makes additional room for the synchrotron radiation fan and relaxes the tight aperture conditions in this element.

The disadvantage of the proposed novel solution is an unconventional magnet design, and net forces on the separator due to the detector solenoid field. Since this solution is rather new, these issues have not been studied yet in detail.

Based on such a combined function magnet separator, a self consistent design has been produced which is described below. The β-functions are somewhat relaxed compared to the lattice described in the previous section. Some tribute had to be paid to optics matching to the arcs and realistic magnet apertures. The luminosity improvement factor 4.55 which corresponds to a peak luminosity of $L = 9.2 \times 10^{31} cm^{-2} sec^{-1}$. A Table 2 with updated values is given below. The actual lattices and optics used in defining the magnet design requirements for the e-ring are shown in Fig.6 and for the p-ring in Fig.7. The lattice layout and optics functions are symmetric about the IP so only half of the interaction region magnets are presented.

In this subsection we give an overview of the lattice layout which is followed by more detail descriptions of the magnet parameters and required apetures in later subsections.

The first accelerator magnet starts 1.2 m from the IP and is a combined function (dipole + quadrupole) magnet to provide the horizontal bend for the e-beam to separate it from the p-beam in subsequent magnets and to provide early vertical focusing to help reduce the e-chromaticity. It is followed by a quadrupole doublet which is responsible for the main part of the e-focusing. Care is taken to pass all of the synchrotron radiation generated in the separator magnet completely through these quadrupoles.

The first dedicated p-focusing quadrupole starts at 11 m and incorporates a magnetic septum which isolates the high magnetic field region seen by the p-beam from a very low field region

	e-beam	p-beam
energy	$30\ GeV$	$820\ GeV$
bunch charge N	$4.18 \cdot 10^{10}$	$10 \cdot 10^{10}$
Beam Current	$58\ mA$	$140\ mA$
normalized emittance ε_N	$1.85 \cdot 10^{-11}\ mGeV^{-2}$	$5\pi\ \mu m\ rad$
horizontal emittance	$16.65\ nm\ rad$	$5.72\ nm\ rad$
emittance ratio	0.13	1
horizontal β at IP β_x^*	$0.83\ m$	$2.4\ m$
vertical β at IP β_y^*	$0.35\ m$	$0.13\ m$
beam size $\sigma_x \times \sigma_y$	$117\mu m \times 27\mu m$	$117\mu m \times 27\mu m$
beam-beam tune shift/IP $\Delta\nu_{x,y}$	.04, .03	.002, .0004
number of colliding bunches	174	
luminosity	$9.2 \cdot 10^{31}\ cm^{-2}s^{-1}$	
specific luminosity	$2.0 \cdot 10^{30}\ cm^{-2}s^{-1}mA^{-2}$	
luminosity increase factor	4.55	

Table 2: Parameters for Upgraded IR Lattice with Combined Function Magnet

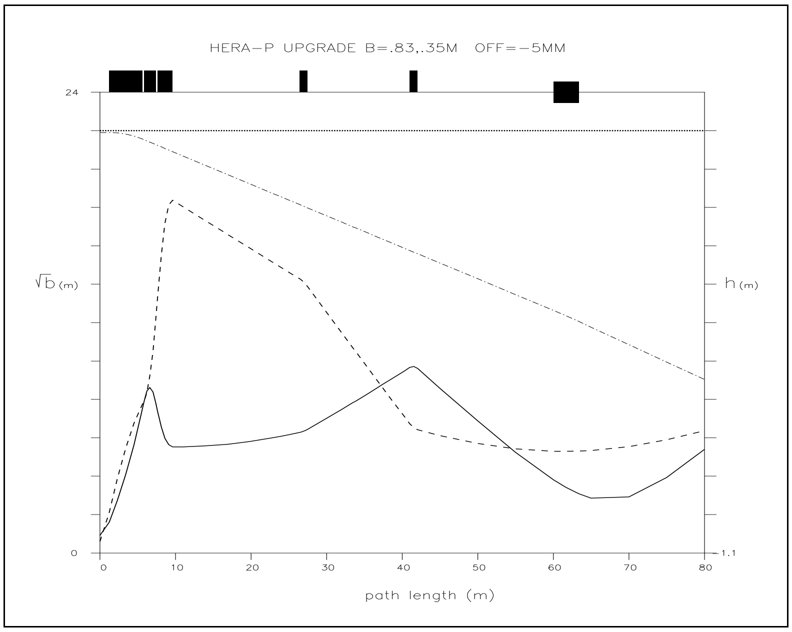

Figure 6: The e-optics for the near IP region are shown here. The horizontal $\times$ vertical $\beta^\star$ are 0.83×0.35 m respectively and the interaction point is shifted inward by 5 mm. Plotted here is $\sqrt{\beta}_{Hor}$ (solid line), $\sqrt{\beta}_{Ver}$ (dash line) and horizontal beam offset (dash-dot line). In the IR quadrupoles peak-β_{Hor}=74 m and peak-β_{Ver}=337 m. The magnets beyond 26 m can be used to help match to the optics and geometry of the arcs.

for the e-beam. This quadrupole is vertically focusing and is followed by a second vertically focusing quadrupole with a special coil structure.

In this second p-quadrupole all of the excitation current for one coil is made to pass through a limited region between the e- and p-beams. The configuration required is similar to that planned for the PEP-II B-Factory [1] and this special coil configuration yields the quadrupole

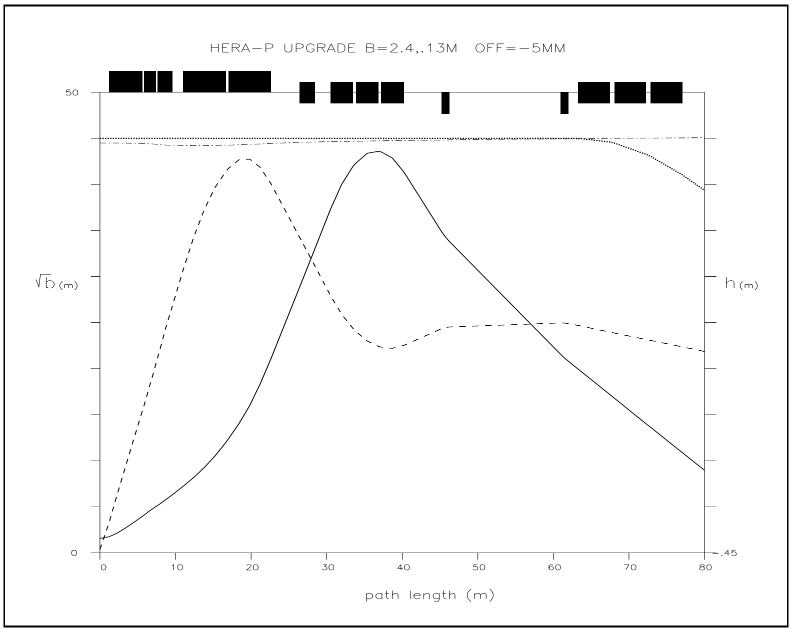

Figure 7: The p-optics for the near IP region are shown here. The horizontal $\times$ vertical $\beta^\star$ are 2.4×0.13 m respectively and the interaction point is shifted inward by 5 mm. Plotted here is $\sqrt{\beta}_{Hor}$ (solid line), $\sqrt{\beta}_{Ver}$ (dash line), horizontal beam offset (dash-dot line) and vertical beam offset (upper solid line). In the IR quadrupoles peak-β_{Hor}=1900. m and peak-β_{Ver}=1826. m. Additional magnets at 28. m and beyond 40. m can be used to help match to the optics and geometry of the arcs. Note on this plot the sign has been reversed for the vertical deflection given by the BU-dipoles starting at 63. m.

equivalent of a current septum for separating the high field region seen by the p-beam from the reduced field seen by the e-beam.

Together these first two septum magnets provide the bulk of the vertical focusing needed and act together to comprise the first lens of a focusing doublet for the p-beam. The horizontally focusing lens for the p-beam is made up from three already existing standard type quadrupoles which complete the horizontal focusing by 40 m.

There are a few additional secondary magnets, quadrupoles and dipoles, which are useful for optics matching and maintaining the present e- and p-ring geometry. These secondary magnets, whose requirements are not as stringent as the main magnets discussed so far, are addressed in a final subsection.

For aperture plots given in subsequent subsections we indicate the regions for $\pm 20\sigma$ for electrons $\pm 12.5\sigma$ for protons, $\pm(3\sigma{+}6$ mm) for synchrotron radiation and $\pm 5\sigma$ for neutral vector radiation cone coming from the e-p IP for a luminosity signal. The beam spot sizes are matched according to the parameters given in Table 2. The luminosity upgrade improvement achieved is a factor of 4.55. A vacuum beam pipe wall thickness no less than 1 mm is maintained in all magnets.

The synchrotron radiation criteria, $\pm(3\sigma{+}6$ mm) used in these plots is only meant to be representative (i.e. as a guide for the eye) as there has been no opportunity to simulate the actual distribution in the Monte Carlo. The synchrotron radiation profiles are plotted coming from the upstream edge of the first separator magnet (gives extreme ring outside limit) and from the middle of this same magnet. As an indicator of where septum masks are required, synchrotron radiation profiles are indicated from the downstream (gives ring inside limit) on two of the Figures.

3.4 Magnet Design

by B. Parker

3.4.1 Combined Function Separator Magnet

A conceptual design of an air coil dipole magnet is part of the ZEUS report and will not be further described here. Instead we describe an air coil combined function separator as necessary for the improved solution.

An air-coil combined function separator magnet (CFS) provides the bending required to separate the e- and p-beams. In addition if it some provides vertical focusing it is possible to significantly reduce the vertical β-peak in the e-optics and reduce the vertical chromaticity.

A bend of 8.2 mr is assumed with a gradient in the range of 4 to 5 T/m (4.6 T/m used in optics calculations) over a magnetic length of 4.4 m. The the beam separation and synchrotron radiation spread at downstream end of this magnet are shown in Fig.8. A good field region of ± 15 mm horizontally and vertically is required. Because of the 30/820 e/p magnetic rigidity ratios the CFS has only a small effect on the p-beam.

The coil positions indicated in Fig.8 are derived from a brute force approach to achieving the needed field configuration and can certainly be improved upon with further optimization. The required gradient of 4.6 T/m is achieved with a current density of 10.2 amps/mm^2 and has sufficient coil area that the power dissipated per magnet is 100 kW. Over the ± 15 mm horizontal region seen by the beam the gradient is constant to better than 1%. It should be possible to reduce the coil dimensions somewhat and thus to free up more physical aperture as indicated by calculations by Willeke for a somewhat more refined configuration. The example shown is included as a proof of principle.

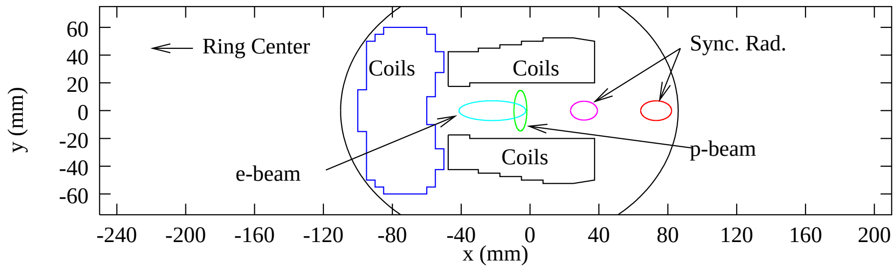

Figure 8: Aperture plot at downstream end of final separator dipole. On this and subsequent plots the coordinate system is such that ring center is to the left (negative numbers) and $\pm 20\sigma$ is indicated for the e-beam and $\pm 12.5\sigma$ for the proton beam. The extreme (ring outside) position of the synchrotron radiation cone is indicated as shown along with one intermediate position. The coil dimensions shown are subject to change and will most likely be reduced in size and moved somewhat further from the beams.

Note that compared to a pure dipole separator it is expected to be possible to eliminate the conductor at the magnet mid-plane on the ring outside to provide extra space for the synchrotron radiation fan.

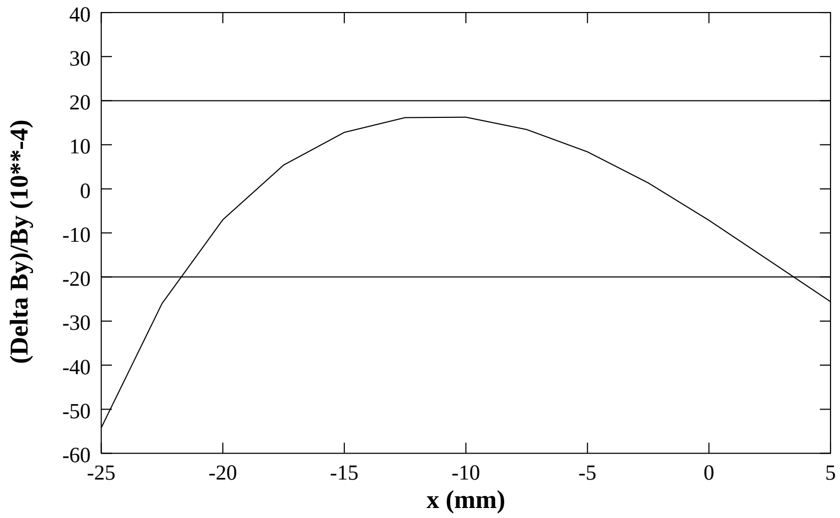

Figure 9: $\Delta B_y/B_y$ as a function of position along the horizontal axis. Note that the field quality is only four times worse that the typical $\pm 5\times 10^{-4}$ even for the preliminary configuration shown. Since on average the β-functions are much smaller in this magnet than in other e- and p-ring magnets, the indicated criteria of $\pm 20\times 10^{-4}$ might be a reasonable design target for this magnet.

3.4.2 Horizontally Focusing e-Ring Quadrupole

After exiting the CFS the beams enter a modified horizontally focusing quadrupole magnet. This quadrupole is centered on the e-beam. The beam positions at the end of this magnet are shown in Fig.10. In order to pass the synchrotron radiation from the separator magnet a gap must be provided in mid-plane of the ring outside coils. The magnetic aperture required for this magnet is driven by the requirement to allow $\pm 12.5\sigma$ for the protons at their outside position.

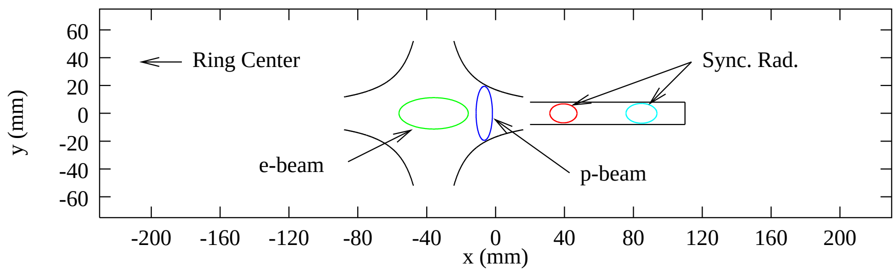

Figure 10: e- and p-beam positions at end of the first horizontally focusing e-ring dipole. This quadrupole is centered on the e-beam however the p-beam is still within the quadrupole aperture. The assumed 35 mm pole radius is indicated as well as a ± 8 mm vertical cutout to pass the synchrotron radiation from the separator magnets.

This magnet has a magnetic length of 1.6 m with a gradient of 28.6 T/m. With a pole radius of 35 mm the pole field reaches 1. T.

It might be possible to construct this magnet from parts of existing HERA QR-type magnets although with such a high pole tip field and compromised coil placement it could be desirable to design a new pole contour and lamination cross section for this magnet.

3.4.3 Vertically Focusing e-Ring Quadrupole

The next magnet outward form the IP is a vertically focusing quadrupole. This quadrupole is also centered on the e-beam. The beam positions at the end of this magnet are shown in Fig.11. As with the previous magnet the ring outside coil must be split along its mid-plane in order to pass the synchrotron radiation from the separator magnet. Here the magnet apeture requirements are completely dominated by the $\pm 12.5\sigma$ for the proton beam.

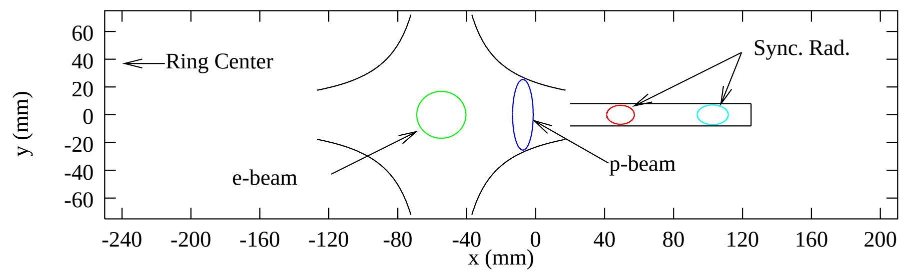

Figure 11: e- and p-beam positions at end of the first vertically focusing e-ring dipole. This quadrupole is centered on the e-beam however the p-beam is still within the quadrupole aperture. The assumed 50 mm pole radius is indicated as well as a ± 8 mm vertical cutout to pass the synchrotron radiation from the separator magnets.

This magnet has a magnetic length of 2.0 m with a gradient of 15.9 T/m. With a pole radius of 50 mm the pole field reaches 0.79 T.

It may be possible to construct this magnet using the laminations from existing HERA QS-type quadrupoles. Since a QS lamination is half that required for this magnet, a full magnet can be constructed that is half the length of a present QS quadrupole. New shorter coils, with the indicated mid-plane split, are however required.

3.4.4 Vertically Focusing Magnetic Septum Quadrupole

The e- and p-beams are separated into two vacuum beam pipes at the magnetic septum quadrupole (MSQ). The beam positions at the beginning of the MSQ are shown in Fig.12. The MSQ provides the same functionality as the QS mirror quadrupoles in the original HERA design. That is it allows having the strongest earliest possible focusing possible for the p-beam while providing an essentially field free region for the e-beam. The MSQ differs from the QS-magnet in that it has a radically cut away mirror plate which enables its placement much closer to the IP than is possible for a QS magnet. In addition because of its closer placement, where the proton beam spot is not as large, it can have a smaller apeture and this translates to having a higher gradient. Thus the net result is to have a stronger quadrupole placed closer to the IP which is precisely what is needed to achieve stronger more effective focusing of the p-beam.

The main challenge in designing the MSQ is to provide adequate field quality for the proton beam which is positioned close to the cutout section of the mirror plate. A scheme for achieving high field quality is outlined in the paper by M. Marx *et.al.*.[2] With proper shaping of the cutout region, a modest field quality, at the few $\times 10^{-3}$ level can be achieved at a fixed excitation current. The trick for achieving standard accelerator magnet field quality, $\Delta B/B \approx 5 \times 10^{-4}$ is to place a small correction coil in the vertex of the cutout as close as possible to the proton beam. In 2D filed calculations it is found that correction currents which are a very small fraction of the main excitation current lead to good results as shown in Fig.13.

Several correction coil configurations have been studied and the level of achievable correction is approximately the same for the various configurations. The main difference between the different configurations is the optimum amount of trim current. Configurations with the trim current deeper in the "notch" tend to require smaller correction currents for a given degree of field compensation. Smaller currents are desirable because they require less conductor cross-section and result in a thinner septum.

It is important to make the septum thin not only to reach the closest possible e-p beam separations but to limit the solid angle covered by the septum mask needed upstream of the septum to intercept synchrotron radiation coming from the separator magnet. Since this mask is the closest point to the experiment at which synchrotron radiation is absorbed the unavoidable backscatter from this mask could swamp central detector components if sufficient care is not taken to minimize its size. MSQ prototype testing is planned to be made at IHEP Protvino to optimize the trim coil configuration and to provide feedback on mechanical construction and end-field issues.

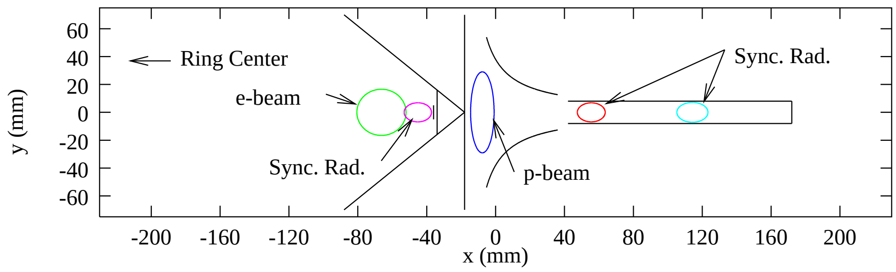

Figure 12: e- and p-beam positions at the start of the MSQ. The assumed 37 mm pole radius, and cut-away mirror with trim coil are indicated as well as a ± 8 mm vertical cutout to pass the synchrotron radiation from the separator magnets. Also indicated is the edge of the synchrotron radiation which passes just inside a collimater/mask just upstream of the septum.

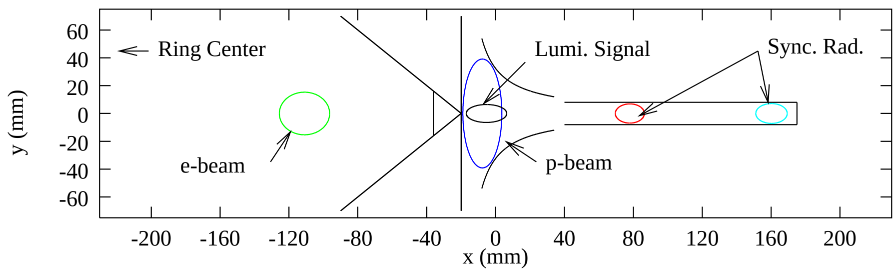

Figure 13: e- and p-beam positions at the end of the MSQ. The assumed 37 mm pole radius, and cut-away mirror with trim coil are indicated as well as a ± 8 mm vertical cutout to pass the synchrotron radiation from the separator magnets. Also indicated is the $\pm 5\sigma$ profile of the neutral vector radiation cone coming from the IP with the divergence of the e-beam at the IP. This is intended to give an indication of the divergence allowed by the MSQ for particles which could be used for a luminosity signal. Note that the $\pm 12.5\sigma$ p-beam + 1 mm assumed vacuum beam pipe (not shown) wall-thickness fills the available magnetic aperture.

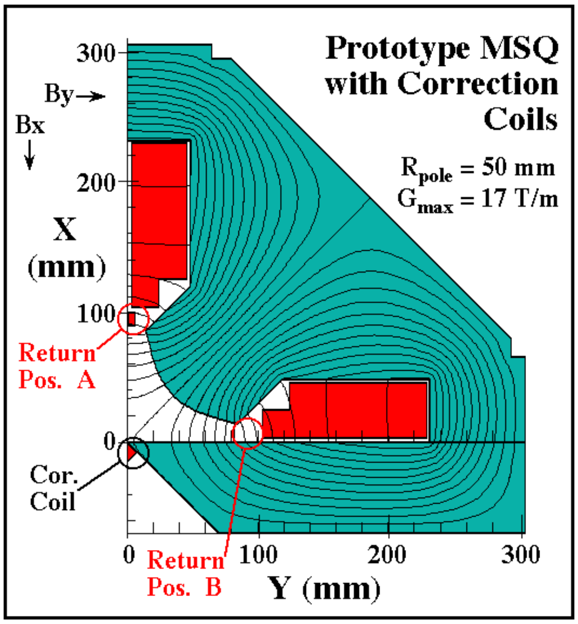

Figure 14: Prototype MSQ with correction coils. The physical geometry and lines of magnetic flux resulting from 2-dimensional calculations of a prototype MSQ. The prototype will be constructed from an existing spare HERA quadrupole and only half of the magnet is shown due to symmetry about the vertical axis. Please note that the coordinate system for this plot is rotated 90^circ with respect to the orientation given in Fig.13. Positions are indicated for the correction trim in the septum notch as well as two locations (A and B) for the return loop. In the final magnet only position B is allowed in order to pass the synchrotron radiation from the separator magnets.

This magnet has a magnetic length of 5.6 m with a gradient of 23.2 T/m. With a pole radius of 37 mm the pole field reaches 0.86 T.

The magnetic apeture of this magnet is by definition defined by the $\pm 12.5\sigma$ for the proton beam and the beam positions are shown in Fig.13 along with a $\pm 5\sigma$ for the neutral vector radiation cone from the IP. Once again the ring outside coil is opened up along its mid-plane to accommodate synchrotron radiation form the separator magnet. Monte Carlo simulations indicate that is probably necessary to pass the synchrotron radiation through the coil region in order that it can be absorbed further away from the IP and thus to reduce the solid angle for backscatter from the absorber to central detector components.

It is noted here that due to the use of a combined function magnet, i.e. dipole plus quadrupole, the e-beam initially sees a lower field as it enters the separator magnet from the IP and this results in a much softer synchrotron radiation spectrum impinging upon the septum mask and headed along the proton beam direction. This helps to reduce backscatter from the septum mask and to ease filtering/pre-absorber requirements for the luminosity monitor.

The apeture available for the neutral vector radiation cone from the IP is limited horizontally as shown in the MSQ to roughly ± 750 μrad and corresponds to $\pm 5\sigma$ of the divergence due to the angular spread of the e-beam at the IP. The MSQ defines the acceptance available for a luminosity monitor.

There is no existing HERA magnet lamination which adequately matches MSQ requirements. If the MSQ were to be made shorter, then a QR-type, 35 mm, profile could be considered

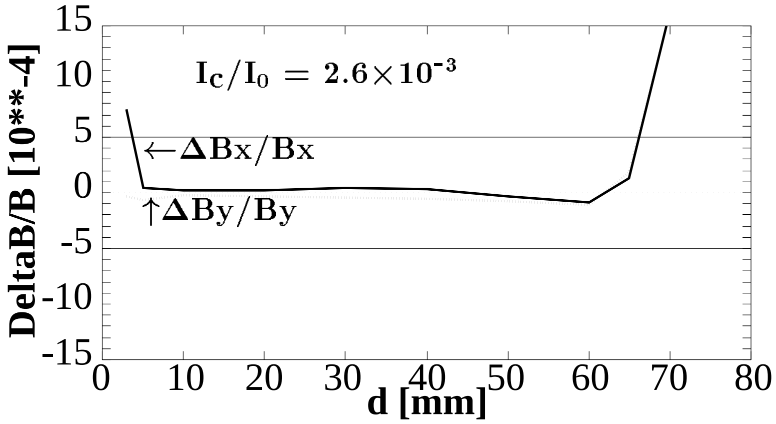

Figure 15: Typical results of MSQ field calculations for prototype configuration (pole radius = 50 mm) with trim correction of 2.6×10^{-3} of the main excitation current. $\frac{\Delta B}{B} = \frac{B-B_I}{B_I}$, in units of 10^{-4}, as function of distance from origin. B_I is field calculated for an ideal quadrupole given by $B_I(d) = \mathrm{Gradient}\times d$.

(the same as for the first horizontally focusing e-beam quadrupole); however, then the beam separation would be too small at the next magnet downstream, the current septum quadrupole. On the other hand, too large a pole radius, such as obtained with a QC (or QS) 50 mm pole radius lamination profile, yields too small a quadrupole gradient. Thus the MSQ is expected to require an entirely new profile and should be optimized according to its own requirements.

3.5 Vertically Focusing Current Septum Quadrupole

The next magnet is a current septum quadrupole (CSQ) of the PEP-II type.[1] Here a full quadrupole apeture is available to the p-beam rather than being limited to a half apeture as in the MSQ case and thus the pole radius can be kept smaller for a higher gradient. The tradeoff for this higher gradient is that the e- and p-beams must be separated more than for a MSQ in order to provide space for the full excitation current turns, typically tens of kiloamperes compared to MSQ correction coils with tens of amps. Thus a CSQ cannot be used as a one-for-one replacement for a MSQ; however, when there is sufficient beam separation to use a CSQ, it will perform better.

The CSQ has a magnetic length of 5.6 m with a gradient of 29.2 T/m. With a pole radius of 32 mm the pole field reaches 0.934 T.

The beam positions at the start of the CSQ are shown in Fig.16 along with the edge of the synchrotron radiation that just misses the MSQ septum mask. Note that an additional septum mask is required to protect the septum coil from this synchrotron radiation which is not intercepted by the MSQ septum.

The beam positions at the downstream end of the CSQ are shown in Fig.17. It is assumed that a synchrotron radiation absorber is placed in front of the CSQ so as to shadow the ring outside coils in the mid-plane. While it is conceivable to try to let much of the synchrotron radiation pass through this magnet also by adding a second septum at the ring outside position, such a configuration would cause the magnet to use an excessive amount of electrical power due to reduced conductor cross section.

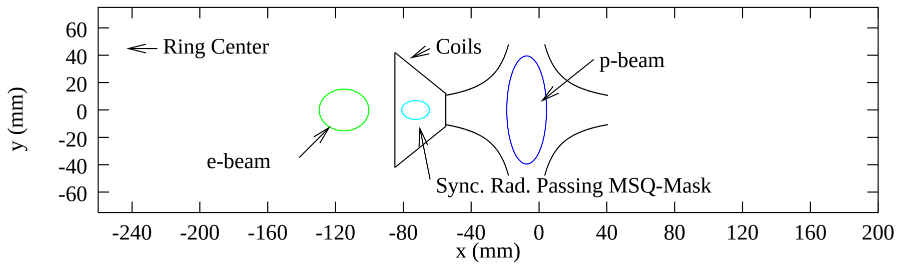

Figure 16: e- and p-beam positions at the start of the CSQ. The assumed 32 mm pole radius is indicated. The synchrotron radiation to the ring outside is assumed to be absorbed in a collimator just upstream of this quadrupole so there is no need for a spit coil in the outside mid-plane. Also indicated is the outline of the area available for the septum coil and a projection for synchrotron radiation which just passes the MSQ septum mask shown in Fig.12. Note that a second septum mask will be needed to protect some of this coil region but the requirements for this mask are not nearly as severe as for the MSQ mask.

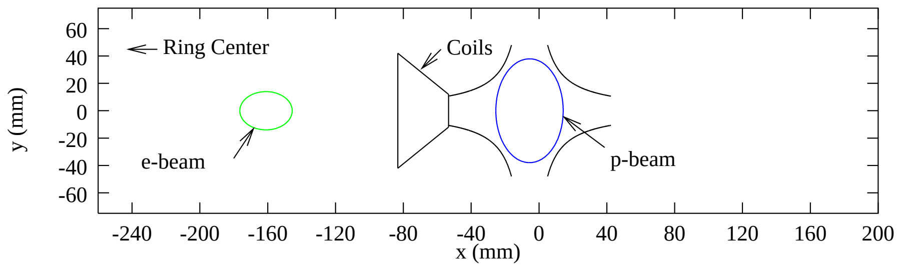

Figure 17: e- and p-beam positions at the start of the CSQ. The assumed 32 mm pole radius is indicated. Any synchrotron radiation which would hit this quadrupole is assumed to be absorbed in upstream collimators. The area available for the septum coil is indicated.

3.5.1 Horizontally Focusing p-Ring Quadrupoles

Once the e-p beam separation is sufficiently large, it is found possible to reuse some of the existing IR magnets to complete the horizontal focusing of the p-beam. Here we use three HERA QR-type magnets connected in series. The beam positions at the first QR quadrupole is shown in Fig.18. The beam separation at the front of this magnet is such that a small amount of material will have to be ground away to make room for the e-vacuum beam pipe.

The beam positions at the middle of the second QR magnet are shown in Fig.19. At this point the e-beam completely clears the outside of the QR magnet. Note also that the $\pm 5\sigma$ for the neutral vector from the IP for reference and it is well inside the region defined by the proton aperture. Thus with a sufficiently large p-ring beam pipe downstream of this magnet it should be possible to pass this cone to the present luminosity monitor location.

The magnetic length assumed for the three QR quadrupoles in series is $3{\times}3{=}9$ m at 24.3 T/m. The QR pole radius of 35 mm then implies a0.85 T pole tip field.

3.5.2 Secondary e- and p-Ring Qudrupoles and Dipoles

Additional quadrupoles, not covered in the previous sections, are desirable for the e- and p-rings

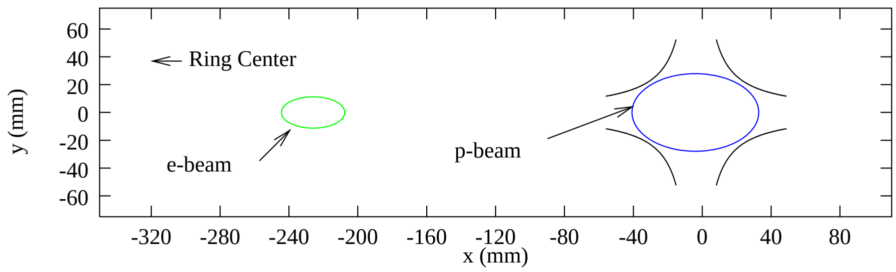

Figure 18: e- and p-beam positions at the start of the first horizontally focusing p-ring quadrupole. The assumed 35. mm pole radius for reusing a HERA QR-type quadrupole is also indicated. Note that some of the material near the e-beam, in the mid-plane of this quadrupole, will have to be cut/grinded away to make room for the e-vacuum beam pipe.

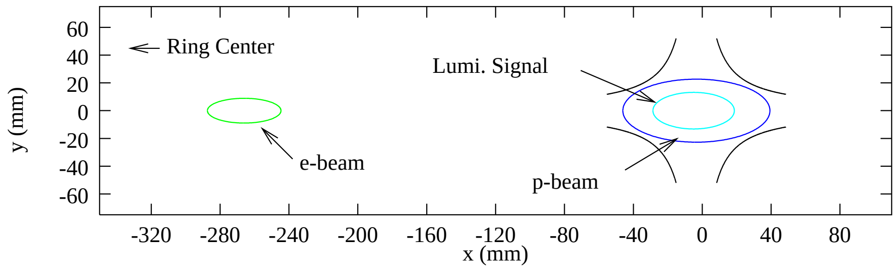

Figure 19: e- and p-beam positions at the center of the second horizontally focusing p-ring quadrupole where the horizontal-β reaches a maximum of 1900. m. The assumed 35. mm pole radius for reusing a HERA QR-type quadrupole is indicated along with the $\pm 5\sigma$ projection of the neutral vector radiation cone from the IP as shown in Fig.13. Note that to this point this cone is always within the 12.5σ of the p-beam. The assertion that the solid angle available for a luminosity monitor is solely limited by the MSQ is subject to a detailed analysis of the aperture provided between this magnet and the present monitor location beyond the vertically bending BU dipoles.

- Completing the IR focusing
- Aiding optics matching to the arc regions

For the e-ring it should be possible to place a HERA QL-type of quadrupole at 27 m which is a position just upstream of the p-ring QR quadrupoles discussed in the last section. Such a quadrupole is useful for giving some additional vertical focusing which does not have to be provided where space is precious close to the IP and facilitates optics matching at an existing QL magnet at about 41 m.

For the p-ring an additional quadrupole placed between 40 to 50 m is useful to complete the vertical focusing after the IR and to aid in optics matching to the arcs. The exact placement is not so critical and can be fixed at a later point in time. It is proposed that a pair of HERA QC-type quadrupoles may be sufficient for this purpose. An additional dipole, not covered in the previous sections is needed in the e-ring to

- Close the ring geometry at an appropriate matching point
- Avoid problems due to synchrotron radiation in the superconducting rf cavities.

The scenario proposed is to reuse one of the BH dipoles which is no longer needed near the IP and place at 62 m next to the superconducting rf region. Since the separator magnet provides 8.2 of the present 10 mr separation angle it is possible to close the ring geometry by adding 0.9 mr bend along with increasing slightly, by the remaining 0.9 mr the bend at an existing dipole in the middle of the rf section. Even it 0.9 mr is not found ideal for dispersion and spin-matching purposes, it should always be possible to find a combination of angles, yielding a net 1.8 mr of bend that closes the ring geometry in the middle of the rf section. Closing the ring at the rf section has the following advantages by:

- Splitting the difference between aperture demands due to a slightly different electron trajectory and the demands due to additional synchrotron radiation from bends close to the rf
- And thus avoids having to move the rf cavities

For the p-ring geometry it is useful to place a dipole near 27 m in the otherwise unused space between the vertically focusing and horizontally focusing p-ring quadrupoles. A BS dipole would fit here and provide 200 μr of bend to partially compensate the kick given to the beam by the MSQ.

References

[1] "PEP-II Conceptual Design Report," Chapter 5, Lawrence Berkeley Lab. PUB-5379, 1993.

[2] M. Marx, B. Parker and H. Wümpelmann, "Concept for a New Magnet Septum Quadrupole," European Particle Accelerator Conference, Barcelona, Spain, June 1996. See DESY Internal Report DESY M 96–13, July 1996 or http://mpy-www.desy.de/parker/EPAC96/mop040g.ps on World Wide Web.

3.6 Impact of the new Interaction Region on e^+/e^- Polarization

by E. Gianfelice-Wendt

The shrinking of the space available with the new IP region design involving the new separator magnets has two important consequences for polarization:

1) the experimantal solenoids will not, as at present, be compensated anymore by antisolenoids;

2) the experimental solenoids must overlap with the last machine magnets.

3.6.1 Effect of antisolenoid suppression

. A magnetic field parallel to the polarization direction $\hat{n}_0$ does not change $\hat{n}_0$. So if rotators are used to get longitudinal polarization at the IP, the solenoidal field does not affect $\hat{n}_0$ (this is not completely true, as we will explain below). There is only a relatively small increase of the betatron resonances due to the betatron motion of the particles in the uncompensated field of the solenoid. This results in a lower polarization level for the ideal machine but the loss is probably negligible wrt depolarizing effects due to the unavoidable machine imperfections.

If rotators are not operating, i.e. $\hat{n}_0$ is nominally vertical and thus perpendicular to the solenoidal field, the field produces a tilt of $\hat{n}_0$. For example the H1 solenoid (B_s=1.5 T, L = 7.333 mt) would tilt $\hat{n}_0$ around the longitudinal axis by about 110 mrad at 29 GeV.

Such a tilt, if not corrected before entering the arcs, would destroy completely the polarization build up mechanism, the Sokolov-Ternov effect.

We could perhaps overcome the tilt by using the scheme invented by K.Steffen for PETRA (1982) and actually applied at LEP. It consists of two vertical bumps, one on each side of the solenoid, involving horizontal bending magnets. For the same purpose one could also use the vertical bending magnets of the rotators. The size of such bumps depends on beam energy and on longitudinal field strength. The feasibility for HERA is still to be proved.

3.6.2 Effect of field overlap

. As mentioned above, even if rotators are operating, the fact that the solenoidal field overlaps with the magnetic field of the last machine elements has as a consequence that $\hat{n}_0$ is not already perfectly longitudinal when the particles enter the solenoidal field. In the following we will assume that the last CoSm magnets before the IP provide together the remaining 10 mrad, which, in the absence of the solenoid, closes the orbit and brings $\hat{n}_0$ in the longitudinal direction. For the ideal case of a "curved" solenoid following the orbit curvature, no orbit distortion is produced, but only a $\hat{n}_0$ distortion.

If the solenoid is straight then both orbit and $\hat{n}_0$ are affected; this is the realistic case that we will discuss here. Thus we need to examine simultanously orbit and spin motion.

On the reference orbit the solenoidal field has a longitudinal as well as a radial component B_x. As long as the solenoid is symmetric wrt the IP the integral of B_x vanishes. The kicks in the fringe field at the entrance and exit of the solenoid cancel. Then there is only a very small effect on the vertical closed orbit due to motion in the solenoid itself since the design orbit is not parallel to the magnet axis. The distortion of $\hat{n}_0$ is negligible too.

If the solenoid is not symmetric $\int ds B_x \neq 0$ and the kicks at the entrance/exit do not cancel. The effect is particularly important for the H1 solenoid, its center being shifted of 1.1 mt. In this case the particles see a vertical kick of 0.2 mrad, whereas the $\hat{n}_0$ is tilted 28 mrad around the radial direction.

This effect can probably be compensated by having different settings for the rotator on the left and right of the North IP.

It remains to be seen whether spin matching against spin diffusion in the straight sections is still possible.

3.7 Investigation of Synchrotron Radiation Background

D. Pitzl

The synchrotron radiation power emitted by the electron beam in a dipole magnet with bending radius R and length ℓ is given by

$$P = \frac{2}{3}\frac{Ie}{4\pi\epsilon_0}\frac{\ell}{R^2}(\beta\gamma)^4$$

with $\beta = v/c$ and $\gamma = E/m_e c^2$. Using $\alpha = \ell/R$, the dipole bending angle, the power may be expressed as

$$P[kW] = 14\frac{\alpha[rad]}{R[m]} I[A] E^4[GeV^4]$$

which is proportional to the inverse bending radius for a given bending angle. For $I = 58\,\mathrm{mA}$, $E = 30\,\mathrm{GeV}$, $\alpha = 8\,\mathrm{mrad}$, and $R = 400\,\mathrm{m}$ the emitted power is 13.2 kW (or $8 \cdot 10^6$ GeV/BC) on each side of the interaction region.

The synchrotron radiation spectrum is characterised by the critical energy

$$E_c = \frac{3}{2}\frac{\hbar c}{R}\gamma^3$$

or

$$E_c[keV] = 2.22\frac{E^3[GeV^3]}{R[m]}$$

which amounts to $E_c = 150\,\mathrm{keV}$ for the numbers used above. The photon spectrum is given by

$$N_\gamma(E_\gamma) = \frac{P}{E_c^2}\frac{S(\xi)}{\xi}$$

with $\xi = E_\gamma/E_c$ and the spectral function

$$S(\xi) = \frac{9\sqrt{3}}{8\pi}\xi\int_\xi^\infty K_{5/3}(x)dx$$

where $K_{5/3}$ is a modified Bessel function. At low energies the photon spectrum diverges like $\xi^{-2/3}$. In all simulations a lower cutoff at 10 keV is applied. The rate of photon emission is then $1.2 \cdot 10^{18}\,\mathrm{s}^{-1}$ in the example given above. At high energies ($\xi \gg 1$) the spectrum falls exponentially. Note that half the synchrotron radiation power is carried by photons with energies above the critical energy. In the simulation the synchrotron radiation is emitted tangentially to the path of individual electrons that are tracked through the magnets. The intrinsic angular spread of the radiation is of order $1/\gamma$ (0.017 mrad at 30 GeV), which is much smaller than the divergence of the electron beam.

The number of photons reaching the central detector components must be reduced by 10 orders of magnitude by a system of absorbers and collimators around the interaction region. The central drift chamber of H1, for example, can tolerate at most 10 synchrotron radiation hits per bunch crossing, before the hit occupancy, after integrating over 12 bunch crossings, starts to affect the pattern recognition efficiency. A similar value is obtained from ageing effects in the chamber, using a limit of 0.03 C/cm of charge accumulated on the sense wires and a

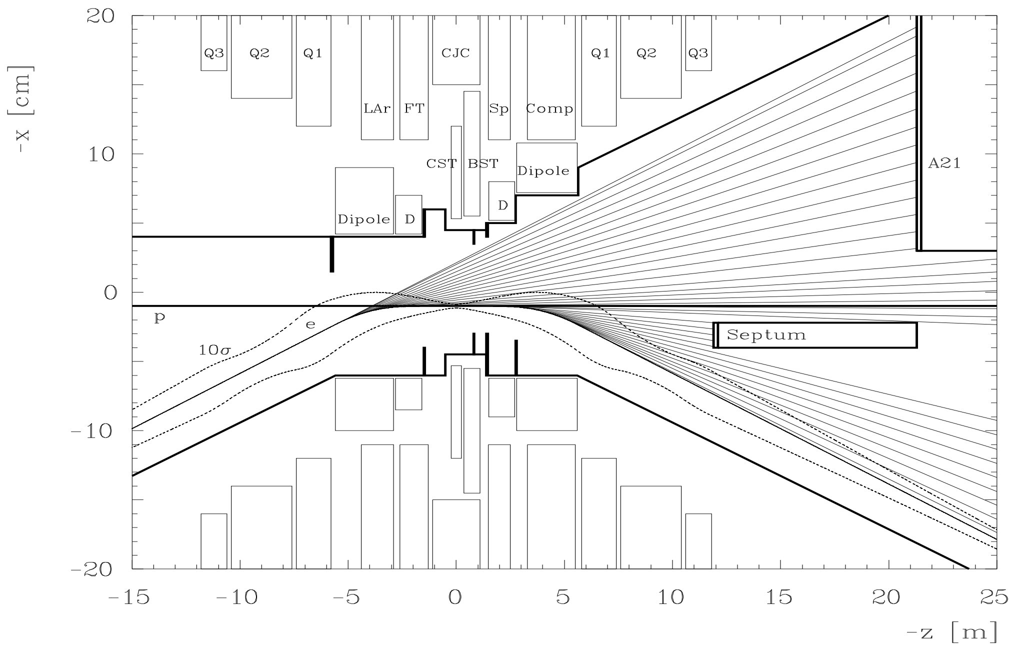

Figure 20: *Layout of a high luminosity interaction region for the H1 experiment in the horizontal plane with the synchrotron radiation fan from the dipole magnets. The beams are displaced by 1 cm horizontally relative to the detector axis. Note the different scales for the z- and x-axes.*

lifetime of 10 years at high luminosity. In the silicon detectors close to the beam pipe a hit rate of $0.01/\mathrm{cm}^2/\mathrm{BC}$ leads to an accumulated dose of 10 krad/y, which can be tolerated for a lifetime of 10 years by the CMOS front end electronics. For the H1 silicon vertex detector the corresponding hit rate is 40/BC, which can be tolerated by the pattern recognition software. In both cases one hit is assumed to deposit 30 keV, and one year of operation is 10^7 s.

3.8 Synchrotron Radiation Shielding

The design of the interaction region is guided by the principle that only doubly scattered radiation may reach the experiment. The direct radiation must not hit the beampipe anywhere inside the detector. It is absorbed by upstream collimators and downstream absorbers. These must be placed as far away as possible to reduce the solid angle for backscattered radiation to reach the central detector. Furthermore, a set of secondary collimators is needed to shield against this backscattered radiation. A possible layout for a high luminosity interaction region with dipole magnets inside the collider experiments is shown fig 20.

3.8.1 Synchrotron RadiationAbsorbers

Absorbers for direct synchrotron radiation must absorb up to 10 kW on an area of a few square centimeters and should have the lowest possible backscattering probability. A detailed simulation of photon interactions in the energy range from 10 to 1000 keV was used to find an optimal absorber. The albedo is defined as the number of backscattered photons devided by the number of incident photons. Fig. 21 shows the albedo as a function of the critical energy of the incident synchrotron spectrum for three different absorbers: pure tungsten, pure copper and a tungsten absorber coated with 0.4 mm silver and 0.2 mm copper. The coated absorber has the lowest albedo (by a factor of 3 at $E_c = 150\,\mathrm{keV}$) but it requires some development work to ensure that the thin coating is not destroyed by overheating the absorber.

It can be understood qualitatively by inspecting the energy spectra of backscattered photons from the three absorbers (see figure 22). The spectrum from a pure tungsten absorber is dominated by the K_α and K_β fluorescence lines, while the copper absorber shows a Compton continuum (the K-lines of copper are just below the 10 keV cutoff). For the coated absorber the silver layer absorbs the tungsten K-lines and the copper layer in turn absorbs the K-lines of silver (25 keV). The thickness of the layers is a compromise between absorbing the fluorescence from the deeper layer and not generating Compton backscattering of the incident radiation. It is found that the optimum coating is independent of the incident spectrum for critical energies between 30 and 200 keV.

Luminosity Monitor Shielding

3.8.2 Luminosity Monitor Shielding

The photon detector of the luminosity monitoring system is placed 100 m downstream from the interaction point. It has a diameter of about 20 cm and as is therefore exposed to the synchrotron radiation emitted in the last 1 mrad bend. The radiation power is about 2.5 kW, or $1.6 \cdot 10^6$ GeV/BC, which has to be reduced by 6 orders of magnitude in front of the calorimeter. The present photon detector of H1 has a copper-lead-water absorber with a thickness of 3 radiation lengths. This thickness should not be increased in order not to further deteriorate the energy resolution of the calorimeter.

The non-absorbed energy fraction as a function of thickness can be estimated by integrating the photon energy spectrum wheighted by the energy absorption length τ_E

$$F(t) = \frac{1}{N} \int_{E_{\gamma,\min}}^{E_{\gamma,\max}} S(E_\gamma)\; e^{-t/\tau_E(E_\gamma)} dE_\gamma$$

whre N is the integral over the incident spectrum. The integrand does not represent the true spectrum at a depth t, since the re-population of the low energy region by scattered photons and fluorescence is not taken into account in detail. However, the tabulated energy absorption lengths include the effects of secondary radiation on average and give a correct description of the overall energy flow. Note that the energy absorption length is larger than the photon mean free path length by up to a factor of 2 in lead and by up to factor of 10 in carbon. A high-Z absorber material is therefore prefered. Figure 23 shows the non-absorbed energy fraction in lead for several critical energies. A reduction of 10^6 in less than $3\,\mathrm{X}_0$ is only possible by

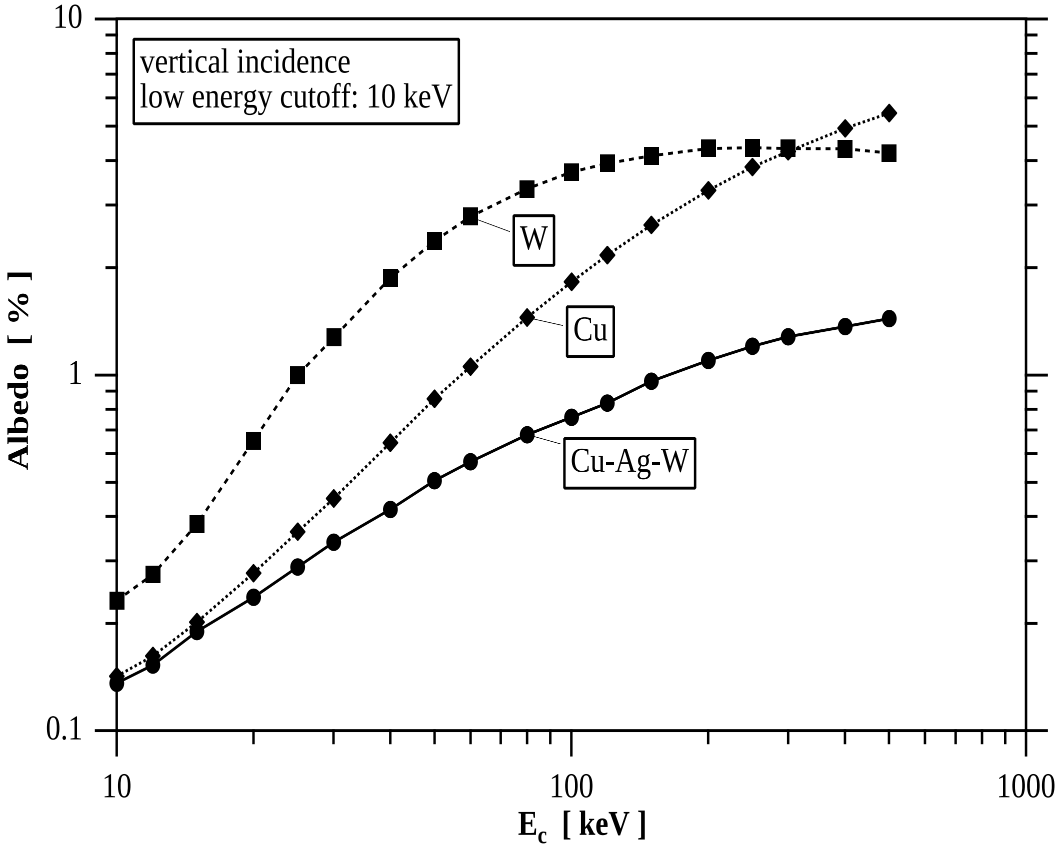

Figure 21: *Backscattered photon fraction for 3 absorbers versus the critical energy of the incident synchrotron spectrum.*

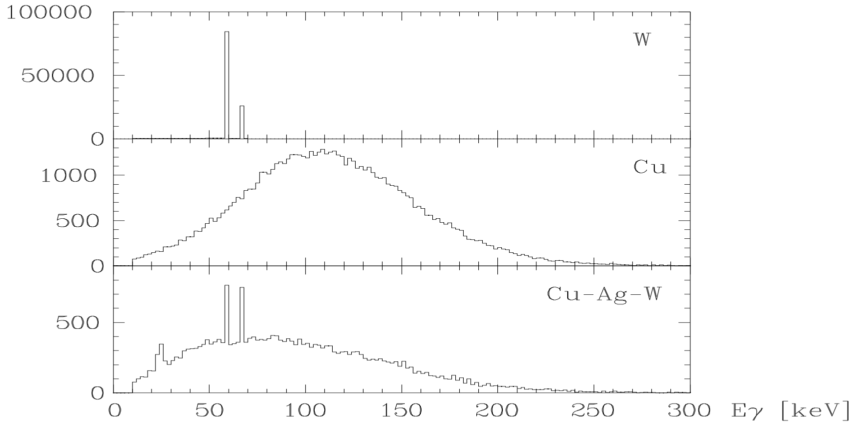

Figure 22: *Energy spectra of backscattered photons for 3 absorbers at* $E_c = 150\,keV$*. The vertical scale is in arbitrary units.*

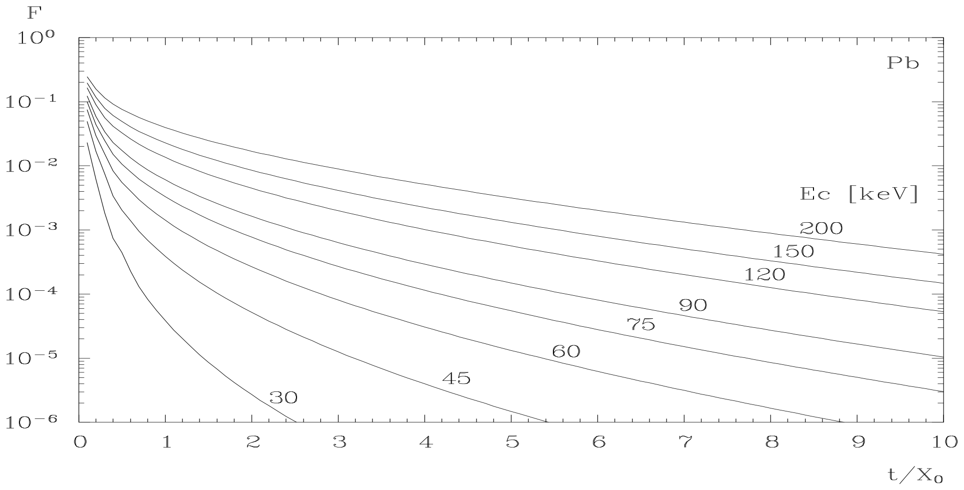

Figure 23: *Non-absorbed energy fraction versus lead thickness for several synchrotron spectra.*

introducing a 'soft bend' with a critical energy below 34 keV for the first 1 mrad. This result is due to the Compton minimum in the photon cross section. Between $E_\gamma = 200$ and 1000 keV the photon mean free path length in lead is larger than than radiation length.

3.8.3 Interaction Region Layout

A possible high luminosity interaction region layout has been developed using the following parameters and considerations:

- The bending angle of 8 mrad is provided by air core dipole magnets inside the experiment.
- The magnets start at ± 1.6 m from the interaction point and extend to ± 5.6 m. The bend over the first 1 mrad is 'soft' with a radius of 1200 m, which requires a magnet length of 1.2 m. The remaining 7 mrad bend is achieved with a radius of 400 m over a length of 2.8 m.
- The width available for the dipole magnets is limited at the outer radius to 11 cm by the H1 compensator and the liquid argon cryostat. The inner radius is determined by the aperture required for the electron beam and by the outgoing synchrotron radiation fan in the horizontal plane.
- The focussing quadrupoles for the electron beam are placed on-axis and do not contribute to the bending.
- The first focussing element for the proton beam (the septum half-quadrupole) starts at ± 12.1 m.
- All synchrotron radiation from the 8 mrad bend passes through the interaction region and is absorbed behind the septum magnet at 21.3 m. The mirror plate of the septum magnet is also exposed to direct synchrotron radiation. Both surfaces are coated for minimum albedo.
- The vacuum tube inside the septum magnet extends up to 20 cm horizontally outward from the beam axis to accomodate the synchrotron radiation fan.
- The central beam pipe section is shielded against backscattering from the absorber and the septum by secondary collimators placed at $z = -0.8$, -1.4, and -2.7 m. These collimators leave an aperture of 20 mm radius required for proton injection and need not be movable.
- The diameter of the central beam pipe is 90 mm such that the existing central and backward silicon tracking detectors of H1 can be accomodated. The critical point is the shielding of the backscattering from the septum magnet with collimators that must not be hit by direct synchrotron radiation.
- The beams are displaced by 1 cm horizontally ring-inwards relative to the axis of the experiment.

This interaction region has been implemented in a simulation program that tracks backscattered photons from the absorber at 21 m and the face of the septum magnet at 12 m. The emission angles are restricted to a solid angle fraction of $7 \cdot 10^{-5}$ of 2π towards the central detector region. Photons are tracked through any number of scatterings until they are absorbed. With more than 10^6 trajectories followed, an overall sensitivity of better than 10^{-11} is achieved.

The simulation was also performed for H1 interaction region layout of 1996 with a beam energy of 27.5 GeV and for a current of 58 mA. Here, the main absorber at -24 m is a pure copper absorber. The strongest source for scattered radiation is the inner edge of the upstream collimator C_3 at 5.6 m.

Table 3.8.3 the summarizes the beam parameters and simulation results. Two conclusions may be drawn. The absolute prediction for the number of hits in the central drift chamber and the silicon detector are well below the tolerable limits, with a comfortable safety margin. The relative increase for the high luminosity interaction region is roughly a factor of 10 for 58 mA, or a factor of 20 compared to the usual operating current in 1996. The synchrotron radiation background at present is very small and therefore hard to measure. At least, it does not severly exceed the simulation result. It is therefore expected that the present detector can be safely operated in the high luminosity environment.

	HERA 1996	HERA upgrade
E_e [GeV]	27.5	30.0
I_e [mA]	58	58
$\beta^*_{x,e}$ [m]	1.0	0.4
$\beta^*_{y,e}$ [m]	1.0	0.4
bend angle [mrad]	10	8
bend radius [m]	1260	400
E_c [keV]	36	150
P_{tot} [kW]	7	27
$N_\gamma(E_\gamma > 10\,\text{keV})$]1/s]	$1.2 \cdot 10^{18}$	$2.2 \cdot 10^{18}$
N_γ central BP [1/BC]	10	120
N_{hits} CST, BST [1/BC]	0.02	1
N_{hits} CJC [1/BC]	0.1	2

4 Upgrade of the ZEUS Interaction Region

HERA-ZEUS Upgrade Group:

D.Boscherini, N.Brook, J.Butterworth, A.Caldwell, C.Catterall, R.Cashmore, C.Foudas, J.Hartmann, U.Karshon, R.Klanner, H.Kowalski, M.Kuze, E.Lohrmann, S.Magill, T.Massam, N.McCubbin, K.Piotrzkowski, M.Riveline, R.Saunders, U.Schneekloth, W.Schott, L.Suszycki, J.Tickner, K.Tokushuku, D.C.Williams, F.Zarnecki

Editor: W.Schott

4.1 Summary

We report on the status of the new design of the ZEUS interaction region as discussed in the frame of the HERA Luminosity Upgrade Group and on a first evaluation of the impact on the ZEUS components close to the beam.

4.2 Introduction

As discussed extensively at the workshop, an increase in HERA luminosity above the design value will allow the experiments to extend substantially the current fields of research and even open up new regions of activity. However, most of the parameters that determine the luminosity of the HERA accelerator complex are at their technical limits, and to push them further would need a very major effort of the laboratory. The most promising option is a reduction of the beta functions at the interaction region. A scenario as given in Table 3 would raise the maximum luminosity by a factor of about five above the nominal value of $1.5 \times 10^{31}/\mathrm{cm}^2\mathrm{s}$.

Technically this requires a rearrangement of the HERA magnets in the experimental area. A smaller beta function at the interaction point (IP) leads to a faster growth of the beam envelopes between the IP and the first focusing magnet and the first quadrupole has to be as close as possible to the IP. Therefore the separation of the beams (e, p) with bending dipole magnets should be done as close to the IP as possible.

This means that accelerator magnets have to be installed inside the central part of the existing HERA detectors. This Working Group made a first study of the technical feasibility and the consequences of this concept. The work done by ZEUS members was based on a design study by F.Willeke, that foresees as innermost elements magnets with 8 mrad bending angle, which start at 5.6 m distance from the IP and reach as far as possible into the detector (minimum 1.2 m distance from the IP).

	Present	Proposed
β_x^p	7 m	3 m
β_y^p	0.7 m	0.15 m
β_x^e	1 m	0.4 m
β_y^e	1 m	0.4 m

Table 3: Proposed scheme of beta functions.

The present report gives a first preliminary assessment of the impact of the luminosity upgrade on the ZEUS detector. A more detailed report is to follow.

4.3 The new HERA beam line inside ZEUS

Here we discuss the magnet system for the final 8 mrad bending of the electron beam within ± 5.6 m of the IP. The concept of bringing HERA magnets inside the existing ZEUS detector is subject to several boundary conditions:

- The transverse outer dimensions of the magnets are limited by the 20 cm beam pipe hole of the ZEUS calorimeter.
- The aperture of the magnets has to be wide enough to accommodate the beams and the fan of synchrotron light from the bending of the electron beam.
- The front face of the ZEUS calorimeter should not be shadowed by the magnets, i.e. particles originating from the IP should reach the calorimeter unobstructed.

In addition to these general requirements, consideration has also to be given to aspects like construction of beam pipe, absorption of reflected synchrotron radiation, installation, support etc. Presently two options for the magnet layout are under discussion:

Option 1: An air coil dipole magnet is used on either side of the IP, however, in a somewhat asymmetrical way (see Fig. 24). The magnet on the forward side (ZEUS coordinate $z > 0$) has an outer diameter of 14 cm, an inner diameter of 8 cm, and a length of 400 cm. The magnet ends at $z = 160$ cm, just behind the line-of-sight between IP and FCAL front edge.

The magnet on the rear side (ZEUS coordinate $z < 0$) has an outer diameter of 19 cm, an inner diameter of 12 cm, and a length of 410 cm. The magnet ends at $z = -150$ cm in line with the RCAL front face. It has a wider aperture and is displaced in the horizontal plane by 15 mm to accommodate the fan of direct synchrotron radiation.

Option 2: Here the magnet layout (see Fig. 25) as compared to option 1 is different on the forward side. The air coil dipole magnet has now the same inside and outside diameter as the rear one. However, the length is only 340 cm, ending at $z = 220$ cm.

A permanent SmCo magnet provides a dipole field between $z = 220\,\mathrm{cm}$ and $z = 150\,\mathrm{cm}$. The permanent magnet can be closer to the IP without shadowing the forward calorimeter because the diameter gets smaller towards the IP.

The field of the SmCo is relatively low (approx. 0.1 Tesla) such that it contributes only a 0.5 mrad bend. This has the advantage of reducing the intensity of synchrotron radiation that hits the ZEUS luminosity detector.

4.3.1 Magnet design

Long dipole magnet. Both design options use long dipole magnets (with somewhat varying dimensions). The homogeneous magnetic field is provided by a coil which has a current distribution that is proportional to the cosine of the azimuthal angle. The conductors of the coil are arranged in 3 layers such that they approximate this current distribution along the magnet circumference (see Figs. 26, 27). The coil does not have an iron yoke since it will be inside the ZEUS compensator magnet.

Normal conduction technology is preferred because of space restrictions and in order to keep the infrastructure requirements simple. At a nominal field of approximately 0.2 Tesla the normal conducting coil will use on the order of 100 kW of power. Cooling water is circulated inside the hollow conductor. Several parallel cooling channels are needed to keep the temperature of the magnet below a value that is acceptable for the ZEUS detector. The connections to the coil will be made at the magnet head at $z = \pm 5.6\,\mathrm{m}$. Care must be taken to prevent heating of detector components situated close to the magnet. Safety of this magnet also requires special considerations.

Permanent magnet. The particular feature of option 2 is a permanent magnet on the forward side of the detector. Permanent magnets built from rare-earth-cobalt alloys like SmCo can provide high magnetic field strength at a very compact design. Fig. 25 schematically shows the tapered permanent magnet. It would actually be segmented in the longitudinal direction into several rings. Each ring is made up from blocks of SmCo material (see Fig. 28). The arrangement of the magnetised SmCo blocks in a ring produces a homogeneous dipole field inside with almost no fringe fields outside. One of the difficulties with this design is the need to provide a temperature stabilisation.

4.3.2 Beam pipe

The beam pipe in the experimental area (see Figs. 24, 25) is divided by flanges into three sections. The construction of the front flange is particularly delicate, because the requirement not to put too much inactive material in front of the sensitive ZEUS detector components leaves little space. At least one bellow is needed to give some freedom for relative motion of the beam pipe sections.

The size of the central beam pipe (outer diameter 100 mm) is mainly determined by the synchrotron radiation, i.e. by the direct radiation and the radiation reflected back from downstream absorbers. The synchrotron radiation reflected back into the central ZEUS region has to be taken care of by dedicated absorbers at $z = -140\,\mathrm{cm}$ (rear flange), $z = -80\,\mathrm{cm}$ and at $z = 150\,\mathrm{cm}$ (front flange).

For a good vacuum pumps are needed inside the beam pipe (see Fig. 26). The magnetic field and the space available inside the large air coil magnet is the same as in the HERA electron dipole magnets. Therefore standard HERA integrated ion getter pumps can be used. Possible negative effects on the electron beam life time, as observed in the HERA electron ring, are not expected, because there is no direct line-of-sight between the anodes of the integrated pump and the beam. The integrated pumps will be in operation only when the air coil magnets are on; additional holding pumps are therefore required between the air coil magnets and the following quadrupole magnets.

The pumping speed can be increased by equipping one of the pumping channels with NEG pumps. The same design can be used as for the HERA dipole pumps, which are in preparation. The advantage is a high pumping speed for active gases independent of the magnetic field.

4.3.3 Support structure

The long dipole magnets which go into the ZEUS interaction region have a mass of about 600 kg each. The forces from the existing ZEUS magnets on the coils are comparatively small (below 100 N).

There are only limited possibilities to support the new magnets, since the experiment has a number of mechanical constraints. As indicated in Figs. 29, 30 the magnets have to be supported mainly from their outside ends, i.e. with relatively long lever arms. The situation is more favourable on the rear side due to the cryo tower structure. On the front side some weight may be supported inside the ZEUS detector by string connections to the spokesplate.

4.3.4 Installation

The magnets, their corresponding beam pipe elements, and related ZEUS detector components will be installed as pre-assembled units. They are installed from the forward side (see Fig. 31). First the rear magnet with the rear beam pipe part is lowered with the hall crane between the opened ZEUS forward calorimeter halves. This unit is then pushed through the central detector to the rear side. Next the central part of the beam pipe is inserted from the forward side. A planned new silicon microvertex detector should have been assembled around the central part of the beam pipe and will then be installed together with it. After installation it will be dismounted from the beam pipe and attached to the CTD inner vessel. Finally the forward magnet with the part of the beam pipe inserted and the FDET assembled around it will be put in place. Removal of the magnets, beam pipe parts, FDET, and microvertex detector will have to be done in the same way as the installation but in reverse order.

4.4 Background conditions

4.4.1 Background from the proton beam

The background from the proton beam will be higher than at present (1996), because a proton current close to the design value of 160 mA is finally expected, to be compared with the

1995 value of 40 mA. However, this increase will come with the general HERA improvement independent of the low beta scheme.

The low beta scheme should not make a big difference, because all apertures near the interaction point are the same as at present, except possibly a synchrotron radiation absorber at $z = -80$ cm and at a horizontal distance of 20 mm from the beam.

The beam gas background will depend on the possibility to install vacuum pumps inside the separator magnets.

4.4.2 Background from the electron beam

Since the collimators C1, C2, C3 and C4 will no longer be there, they cannot be used to limit background from stray electrons. The effect of stray electron on the ZEUS detector is however small, except for the present Beam Pipe Calorimeter (BPC), which will no longer be there.

Again, independent of the low beta scheme, the general increase of the electron current from 30 mA in 1995 to the design value of 58 mA will have to be accommodated.

4.4.3 Synchrotron radiation

Synchrotron radiation is the most critical source of background. There are three potential sources:

i) Backscattered radiation from the main synchrotron radiation absorbers, which are at distances of $12 \cdots 20$ m from the interaction point.

ii) Edge scattering from absorbers near the interaction point which are installed to protect the experiment from source i).

iii) Synchrotron radiation from the quadrupoles, which start about 5.8 m from the interaction point. Under normal circumstances this is a negligible source. However, if the beam is misadjusted, it can make a large contribution.

In the following, we shall only consider source i), the backscattered radiation.

Fig. 24 shows the interaction region with the line marking the boundary of the direct synchrotron radiation. It is not touched by any absorbers, until it hits the main absorbers, which are situated at distances of $12 \cdots 20$ m from the interaction point. In order to minimize reflection from these main absorbers, they have to be covered by an anti-reflecting coating, e.g. 3 mm W, 0.5 mm Ag, and 0.13 mm Cu. The back reflected radiation constitutes the main background for the detector. It delivers a dose rate of about 0.01 Gray/s, and therefore all sensitive parts of the detector including the beam pipe have to be protected from it. This is done by absorbers placed at -0.8 m and -1.4 m (see Fig. 24). All surfaces hit by the reflected radiation need an anti-reflection coating.

In order to assess the radiation load on the CTD, a comparison with the present situation is made. In Table 4 the present situation is compared with the low beta option. For this comparison an electron energy of 30 GeV, an electron current of 58 mA and a field in the last deflection magnet of 0.22 T have been assumed.

The table shows that the background in the CTD will increase about 15-fold. Compared with the situation in 1995, where currents were about 30 mA, one has to expect a 30-fold increase.

In a run with random triggers, less than 1 hit was observed on average in the CTD in 1995 at 30 mA. The hits were distributed uniformly throughout the chamber. This would translate into less than 30 hits on average for the low beta scheme.

In a similar way the number of hits in a Si detector at a radius of 5 cm and of 0.4 mm thickness can be estimated. One gets $10^{-4} \cdots 10^{-3}$ hits/cm^2/bunch-crossing. This corresponds to a dose rate of $10^{-6} \cdots 10^{-5}$ Gray/s.

	present	low beta
Total power (both sides)	9.7 kW	22 kW
Critical energy	44 keV	126 keV
Dist. of main absorber (weighted)	23.5 m	16.3 m eff.
Reflected into experiment (arb. units):		
Total power	1.0	2.3
(distance of main abs.)$^{-2}$	1.0	2.1
Reflection coefficient	1.0	1.6
Missing action of abs. C1 $\cdots$ 3	1.0	2.0
overall factor	1.0	15

Table 4: Comparison of synchrotron radiation background (present values scaled to nominal electron beam parameters, i.e. 30 GeV and 58 mA)

4.5 Luminosity measurement and photon tagging

The consequences of the HERA interaction region upgrade for the present ZEUS LUMI system and for photoproduction tagging are discussed in this section. Also the concept of a future Beam Monitoring Station is proposed.

4.5.1 Present LUMI system

Synchrotron radiation and filter thickness. At an assumed bending radius of 475 m the thickness of the carbon filter in front of the photon calorimeter of the luminosity monitor would have to be increased from $2 \cdots 3$ radiation lengths (r.l.) to 4 r.l. This would deteriorate the resolution from presently $23\,\%/\sqrt{E}$ (for 2 r.l.) to $>35\,\%/\sqrt{E}$ and increase the minimum energy that can be measured well from 1 GeV to about 3 GeV. The expected uncertainty of the luminosity measurement due to these effects is about 2 % and is not compatible with $\leq 1\,\%$ precision. If, however, a new detector were installed with a preshower detector and better energy resolution, then possibly a 1 % precision could be achieved. Another step to be considered is the use of polyethylene instead of carbon as an absorber.

Event rate. The strongly increased event rate will constitute a problem.

- At a luminosity of $10^{32}/\mathrm{cm}^2\mathrm{s}$ the rate of bremsstrahlung with energy above 1 GeV is 17 MHz. This results in a very high occupancy: on average 2 photons per bunch crossing and only 13 % of bunch crossings without hard bremsstrahlung). Effects of such event pileup, however, can be well simulated, measured and controlled by usage of different energy cuts. Possibly also pileup insensitive measurements (energy flow measurement) can be adopted.
- The present luminosity detector uses PMTs for readout. If one scales the present anode current (already at very low HV) to a luminosity of $10^{32}/\mathrm{cm}^2\mathrm{s}$ one expects 60 μA! Either low gain PMTs (6/8 dynodes) or hybrid PMTs would have to be used.
- Radiation dosage at the worst point is expected to be up to 10 kGray/year and may seriously affect the energy measurement.

Photon acceptance. For the recent Willeke optics the bremsstrahlung cone has a horizontal angular divergence of 0.35 mrad which reduces the photon acceptance from 98 % to 80 %. In such a case systematic effects are much less controlled and may result in an increased error from this source from 0.5 % now to 2 % at the full luminosity. To keep the precision, one can try to either increase the angular acceptance or decrease the electron beam emittance and angular divergence at the IP.

To summarize: A luminosity measurement similar to the one presently used in the ZEUS experiment has an estimated accuracy of 3 %. The accuracy can be possibly improved by ensuring a high photon acceptance and better linearity of the energy measurement. To achieve approximately 1 % precision — desirable for some physics questions — alternative solutions should be considered.

4.5.2 Photoproduction tagging

The present tagging devices are incompatible with the HERA upgrade. There are three possible new locations:

i) About 10 m from the IP, just after the first two quadrupoles; since any extra space (longitudinally) would reduce the luminosity, the detector should be integrated to some extend with the quadrupole/beam pipe — it could be a tungsten spaghetti calorimeter — and use only the typical space available ($20 \cdots 30$ cm) between beam line elements. Such a detector would tag photoproduction at high/medium W, at about $180 \cdots 250$ GeV (corresponding to $35 \cdots 120$ mm distance of the scattered electrons from the beam axis).

ii) At a distance >20 m from the IP a low W (about 80 GeV) tagger could be installed using the technique of the present 44 m tagger.

iii) If high W ($\geq$280 GeV) tagging would be required, then a small detector just after the dipole at -5.6 m could be installed using the technique of the present 8 m tagger.

The main difficulty in running the tagging devices at very high luminosity is a large event rate due to e p bremsstrahlung which results in a significant detector occupancy. Therefore, very good vacuum (to avoid a large e-gas contribution) and a high bremsstrahlung photon acceptance (to allow for efficient vetoing) are essential.

4.5.3 Beam monitoring station

Running experience has shown that scintillation counters close to the beam pipe in the outgoing electron beam direction (C5 counters, Beam Pipe Calorimeter) are essential for a quick monitoring of the background conditions at the ZEUS experiment and the precise determination of the mean z position of the e p interaction region and the monitoring of satellite bunches. The present position around $z = -300\,\text{cm}$ will not be free due to the presence of the new dipole magnet. A new extended Beam Monitoring Station (BMS) is proposed at a position around $z = -560\,\text{cm}$, downstream of the new dipole magnet.

The tasks of the BMS are:

1. Separate measurement of the radiation background from the proton and the electron beam.
2. Measurement of the mean z position (longitudinal) of the e p interaction point from the difference of the arrival times of background particles from the electron and from the proton bunches.
3. Monitoring of the satellite bunches accompanying the main bunches.
4. Measurement of the transverse position of the e p interaction point.
5. Measurement of the luminosity, independent of the present ZEUS luminosity monitor.

A conceptual side view of the BMS is shown in Fig. 32. The main elements are a thin exit window of the vacuum-pipe (i.e. transition from the circular cross section to an elliptical shape), two silicon trackers above and below the beam pipe, each consisting of two microstrip detectors ($60\,\text{mm} \times 60\,\text{mm}$) with horizontal strips and two microstrip detectors with vertical strips, and two small compact electromagnetic calorimeters (e.g. $PbWO_4$ crystals). The minimum length required along the beam is 50 cm.

The timing information from the electromagnetic calorimeters is used to obtain the information for topics 1, 2, and 3. The measurement of small angle inelastic e p scattering (angular acceptance $7 \cdots 12\,\text{mrad}$) and QED Compton scattering ($ep \rightarrow e\gamma p$) will provide events to reconstruct the transverse e p interaction point (using the z position obtained from the timing information in topic 2) and to obtain a measurement of the luminosity.

4.5.4 Beam position monitor

A beam position pick-up monitor positioned around $z = \pm 300\,\text{cm}$ (inside of the new dipole) appears highly desirable. No design work has yet been done.

4.6 Impact on other ZEUS components

The impact of the upgrade of the interaction region for components close to the beam is discussed. There are at present only qualitative results.

4.6.1 CAL

There is some fringe field from the new magnets; Table 5 provides a map of the field values from the air coil magnet. The calorimeter PMTs close to the dipole magnet may require improved shielding — this is under study. Possible effects due to the additional material from the new magnet on the calorimeter performance are presently being studied with Monte-Carlo calculations.

$z = 120\,\mathrm{cm}$ (magnet head)

	$x = 0$			$x = 10$			$x = 20$			$x = 30$		
$y = 0$	0	−1015	0	0	424	0	0	133	0	0	58	0
$y = 10$	0	−408	526	−270	−25	216	−86	62	50	−32	42	17
$y = 20$	0	−124	131	−80	−64	96	−65	−1	48	−37	15	23
$y = 30$	0	−57	58	−30	−42	50	−37	−16	34	−29	0	21

$z = 220\,\mathrm{cm}$

	$x = 0$			$x = 10$			$x = 20$			$x = 30$		
$y = 0$	0	−2032	0	0	846	0	0	264	0	0	115	0
$y = 10$	0	−819	0	−539	−52	0	−172	122	0	−64	81	0
$y = 20$	0	−251	1	−160	−130	1	−130	−5	1	−74	28	1
$y = 30$	0	−116	1	−61	−85	1	−73	−34	1	−58	−3	1

Table 5: Air coil dipole magnet field map at $z = 120\,\mathrm{cm}$ (magnet head) and $z = 220\,\mathrm{cm}$. The ZEUS coordinates x and y are given in cm, the magnetic field B_x, B_y, B_z in Gauß.

4.6.2 Tracking detector

The additional magnetic field does not pose a problem for the performance of the tracking detector and the track reconstruction. For synchrotron radiation effects see Section 4.4.

4.6.3 Silicon vertex detector

Installation of a vertex detector based on Si detector technology appears compatible with the low beta installation. An inside diameter of 10 cm can be accommodated; the radiation background has been discussed in Section 4.4 and appears to be at a tolerable level. More accurate statements can be made once the design for such a device is available.

4.6.4 FMUON

No impact on the performance of the forward muon system is expected.

4.6.5 PRT

Scintillation counters close to the beam pipe are presently located at $z = 5.4$ m and $z = 25$ m to separate diffractive from non-diffractive events. The place of the counters at 5.4 m will be taken by the new dipole magnet. It presently appears difficult to install new counters at this position unless approximately 20 cm of space is freed along the beam direction. This z position is symmetric to the position in the electron direction of the proposed BMS. The counters at 25 m should not strongly be affected by the modification of the interaction region.

4.6.6 LPS

The main impact of the luminosity upgrade on the performance of the ZEUS Leading Proton Spectrometer (LPS) is due to the increased transverse momentum spread of the proton beam, which, compared to the present situation, increases from 25 MeV to 35 MeV in x and 75 MeV to 160 MeV in y. As the detectors have to be at least $10\,\sigma$ away from the beam this results, for protons with $x_L = 1$, in an increase of the lower transverse momentum cutoff from 250 MeV to 350 MeV. No significant change of the longitudinal momentum resolution is expected. The transverse momentum spread however will result in a significant degradation of the resolution of the measurement of the momentum transfer to the proton.

The installation of the LPS does not present a problem in principle. However, it will represent a major operation both in terms of manpower and money. At present it appears that most detectors have to be rebuilt and that the first three stations S1, S2 and S3 will have to be moved. It should however be possible to leave the beam profile at the later stations S4, S5 and S6 unchanged. Every effort should be made so that this option is viable. This will require a close collaboration between HERA and ZEUS.

The main effects on physics are due to the reduced acceptance and the poorer momentum transfer resolution.

For details we refer to the report "The ZEUS Straight Section Upgrade" (ZEUS-Note 96-087 by T. Massam, August 26, 1996).

4.6.7 FNC

As in the case of the LPS, the main impact on the performance of the ZEUS Forward Neutron Calorimeter (FNC) is due to the increased transverse momentum spread of the proton beam. The angular acceptance of the FNC is determined by the apertures of the HERA beam elements, and no major change is expected if proper care is taken with the new beam design. The measurement of the transverse momentum transfer from the beam proton to the scattered neutron will be much less accurate than at present. Again the optimum design will require a close collaboration between HERA and ZEUS.

Overall no major impact on the physics performance of the FNC is expected in an optimized design.

For details we refer to the report "The ZEUS Straight Section Upgrade" (ZEUS-Note 96-087 by T. Massam, August 26, 1996).

4.7 Impact on physics and conclusions

As can be seen from the physics working group reports included in these proceedings, the upgrade of the HERA accelerator to reach luminosities of $1\,\mathrm{fb}^{-1}$ is necessary to exploit the physics capabilities inherent in HERA. High Q^2 and high P_T physics, as well as the search for rare processes, will greatly benefit from the increase in luminosity.

On the other hand, the luminosity upgrade will impair the capability of the ZEUS experiment to pursue physics processes connected to detecting particles at small forward and backward angles. Components such as the beam pipe calorimeter, electron taggers, the proton remnant tagger, the leading proton spectrometer and the forward neutron calorimeter will be seriously affected, and in some cases will have to be removed completely (e.g., the beam pipe calorimeter). This will mean a reduction in the capability of the ZEUS detector for low Q^2 physics. Studies of diffractive physics, forward jets and energy flows will also be affected (see Sections 4.6.6 and 4.6.7). We will obtain as detailed physics results on these topics as is possible before the implementation of the detector modifications, and efforts will be made to preserve as much capability as possible in the new configuration.

Other implications of the proposed options for the magnet layout within ZEUS are currently under study. The options discussed in Section 4.3.1 have been implemented in the full ZEUS Monte Carlo.

- The effect of the upgrade on the measurement of jets has been studied in both resolved photoproduction and DIS. In both cases $15\cdots30\,\%$ more jets are observed in the new configurations in the region $2 < \eta < 3$ for jets with E_T around $6\,\mathrm{GeV}$. Comparison of jets observed in the calorimeter to "true" jets of final state particles indicates that the extra jets in the calorimeter are not associated with true jets and thus the purity of the sample in the forward region is degraded. However, for jets which are matched to true jets the energy resolution is not significantly degraded. The effects of the two configurations are not significantly different.

- The proton dissociative process $ep \to eX_N\psi$, where X_N is a system of mass M_N, has also been investigated. The forward calorimeter energy distributions and the tagging acceptance versus M_N^2 show only small differences with respect to the current configuration. The tagging efficiency slightly increases for small values of M_N^2, presumably because of showering in the magnet.

In summary, these preliminary studies indicate some effects in the forward region, which we anticipate can be handled with careful simulation. Detailed studies are currently under way for a wide range of physics processes, and results will be available in a written report. To date, no major impact has been found due to the presence of the dipole magnets in the ZEUS interaction region on the measurements solely performed with the central detector.

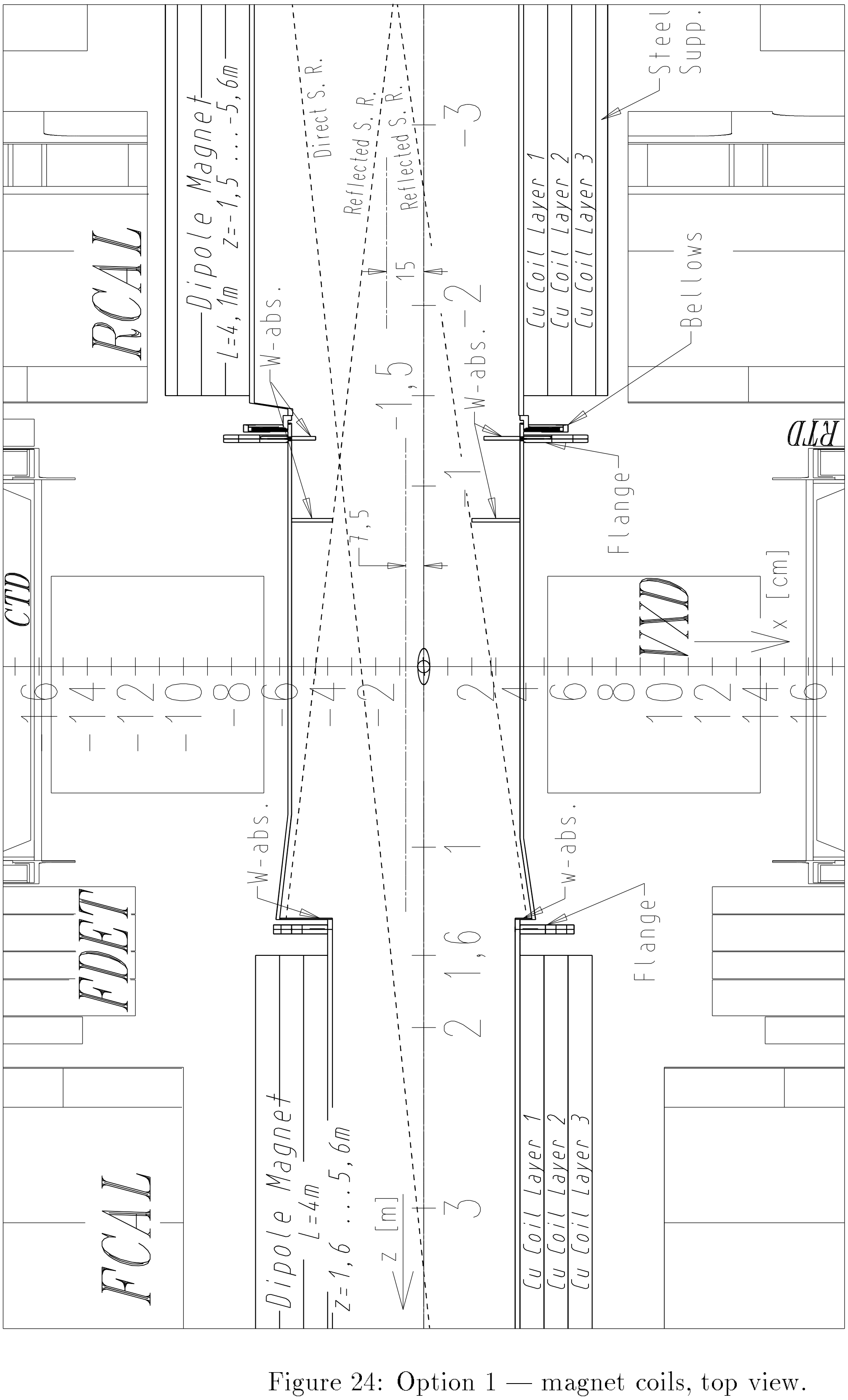

Figure 24: Option 1 — magnet coils, top view.

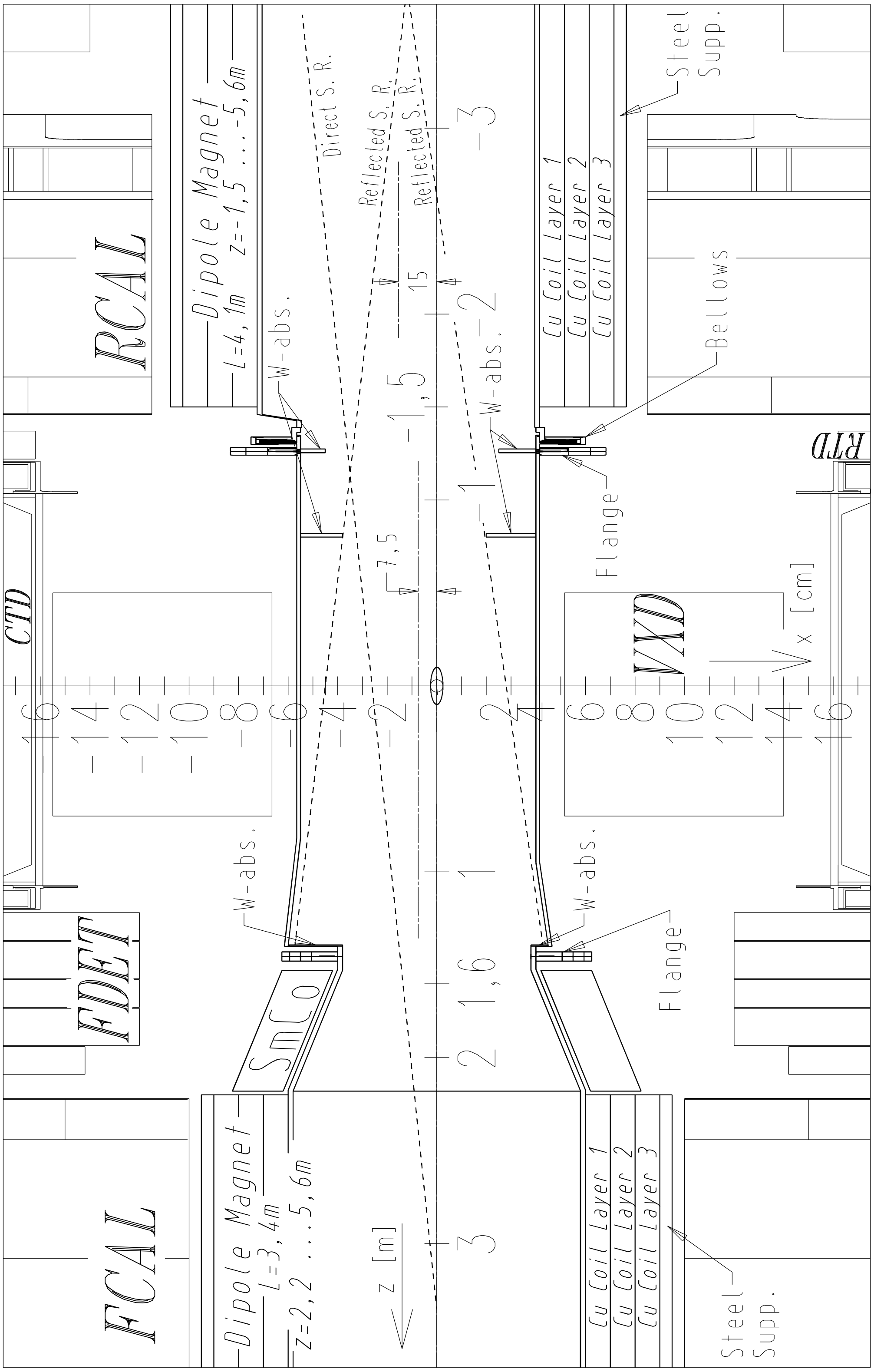

Figure 25: Option 2 — permanent magnet, top view.

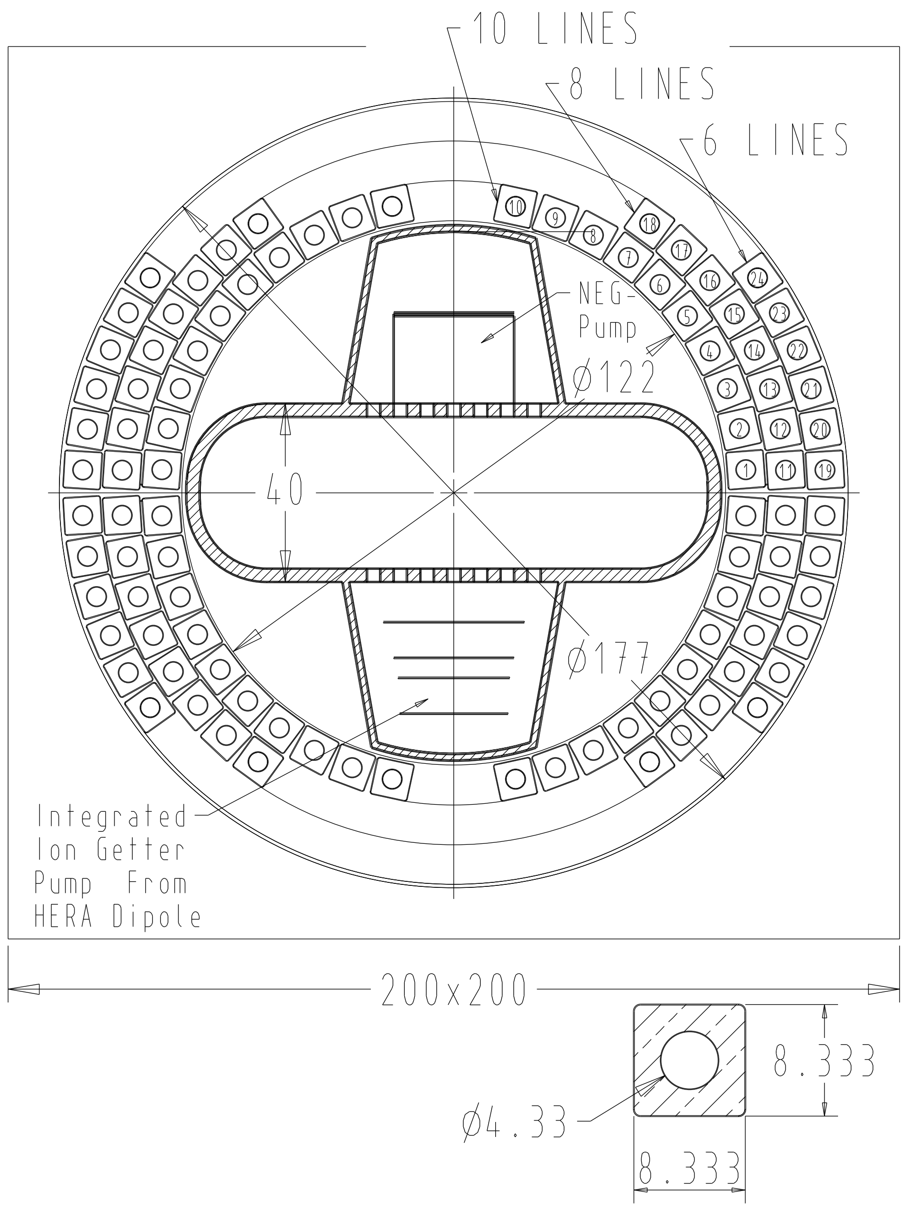

Figure 26: Cross section of magnet coil.

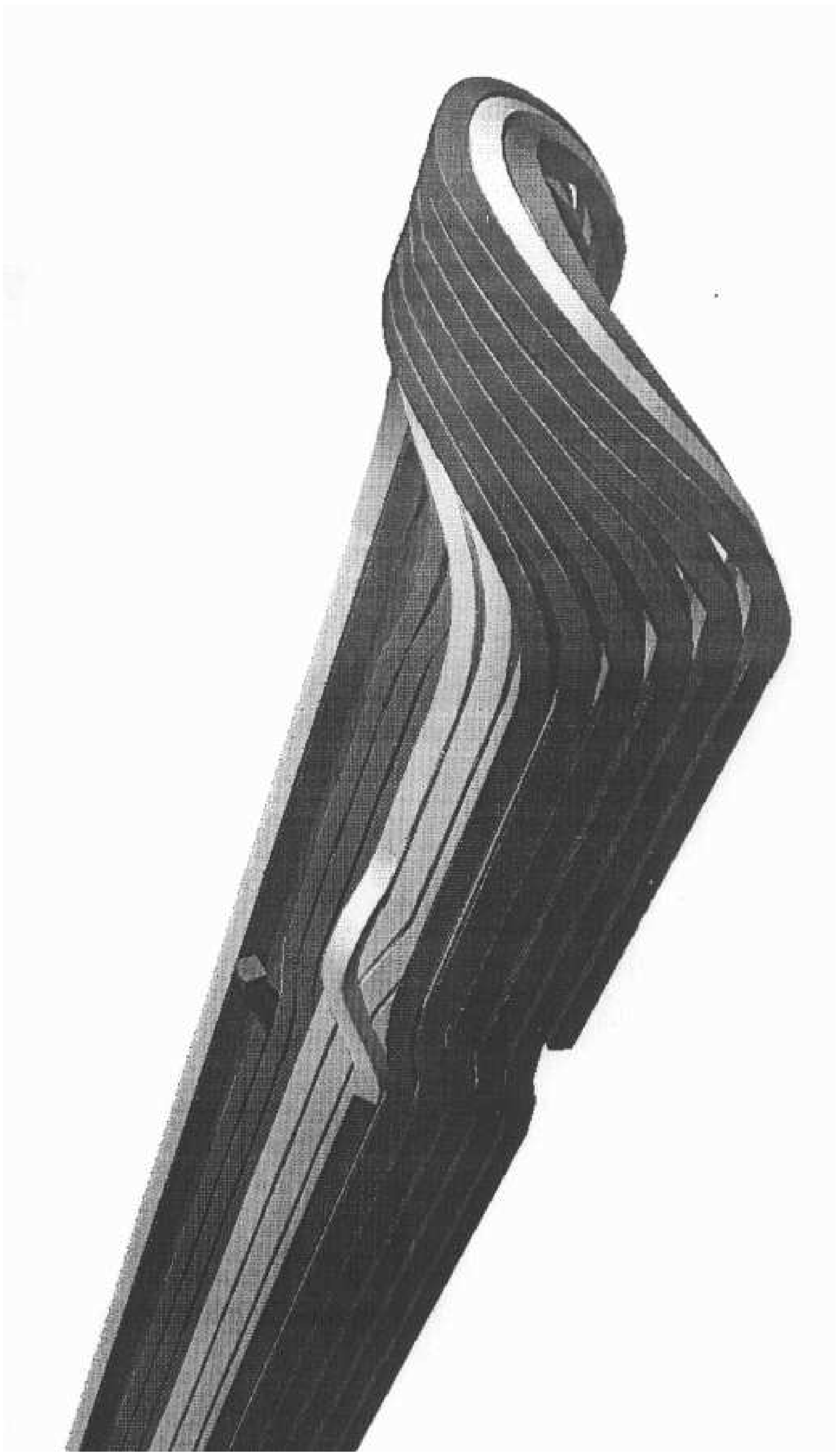

Figure 27: Artist view of magnet coil (upper half).

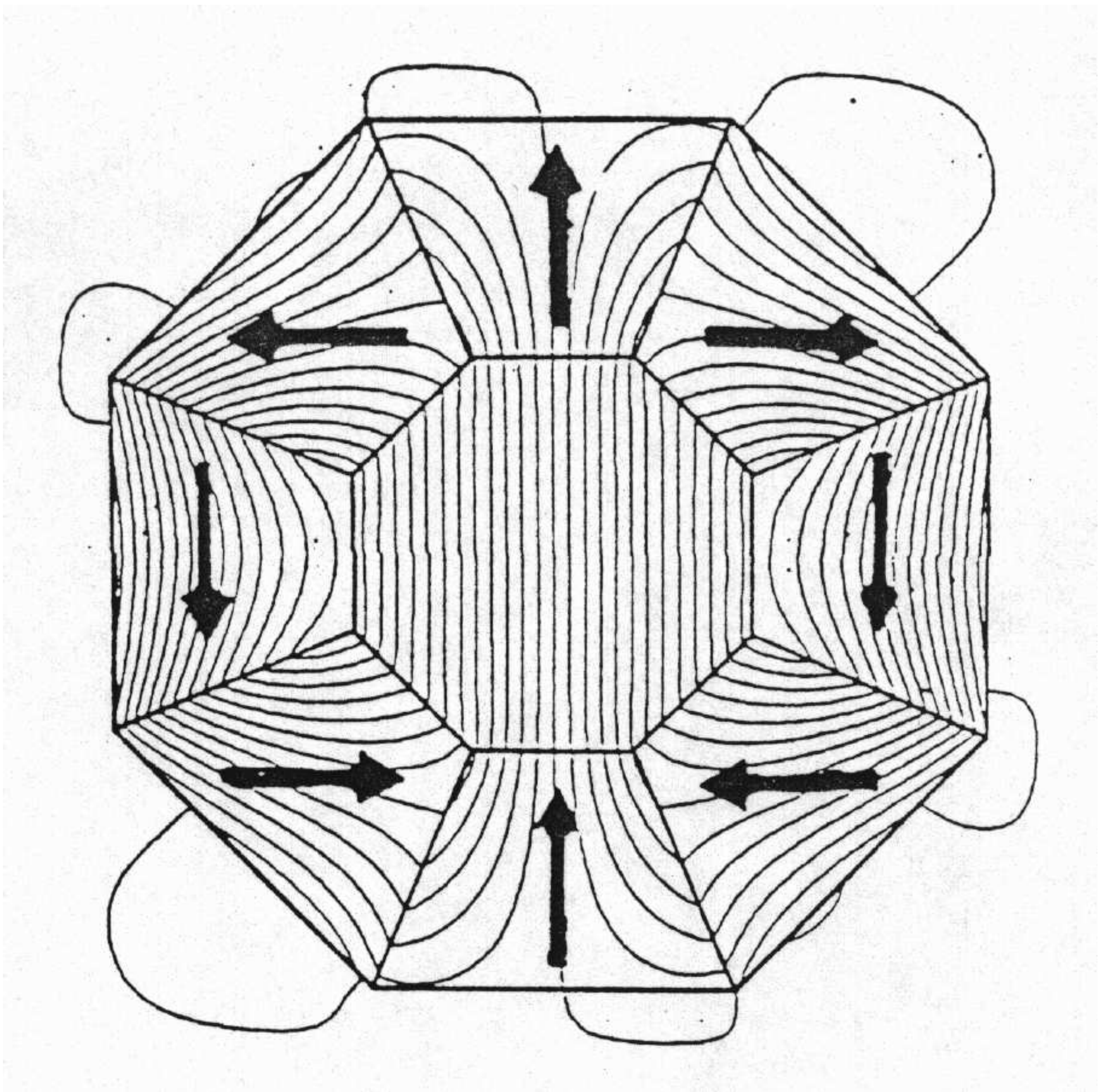

Figure 28: Cross section of permanent SmCo dipole magnet.
A ring-like structure is built from trapezoidal blocks of Sm_2Co_{17}. The block magnetisation and the flux pattern is indicated.

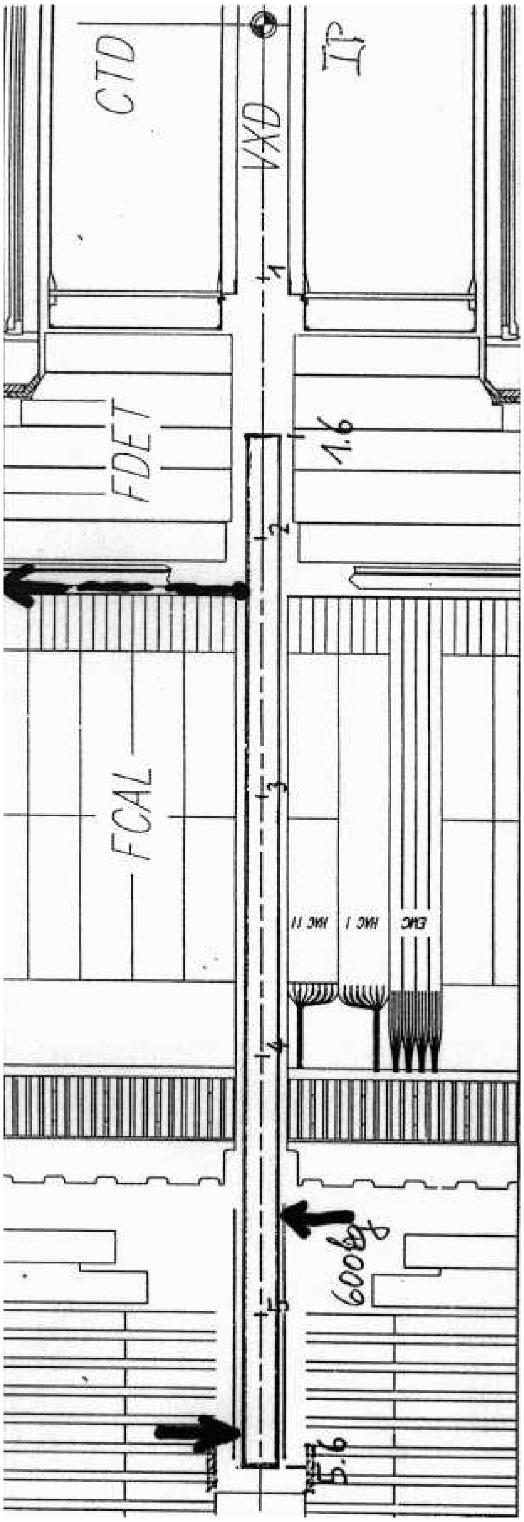

Figure 29: Magnet support on forward side, side view.

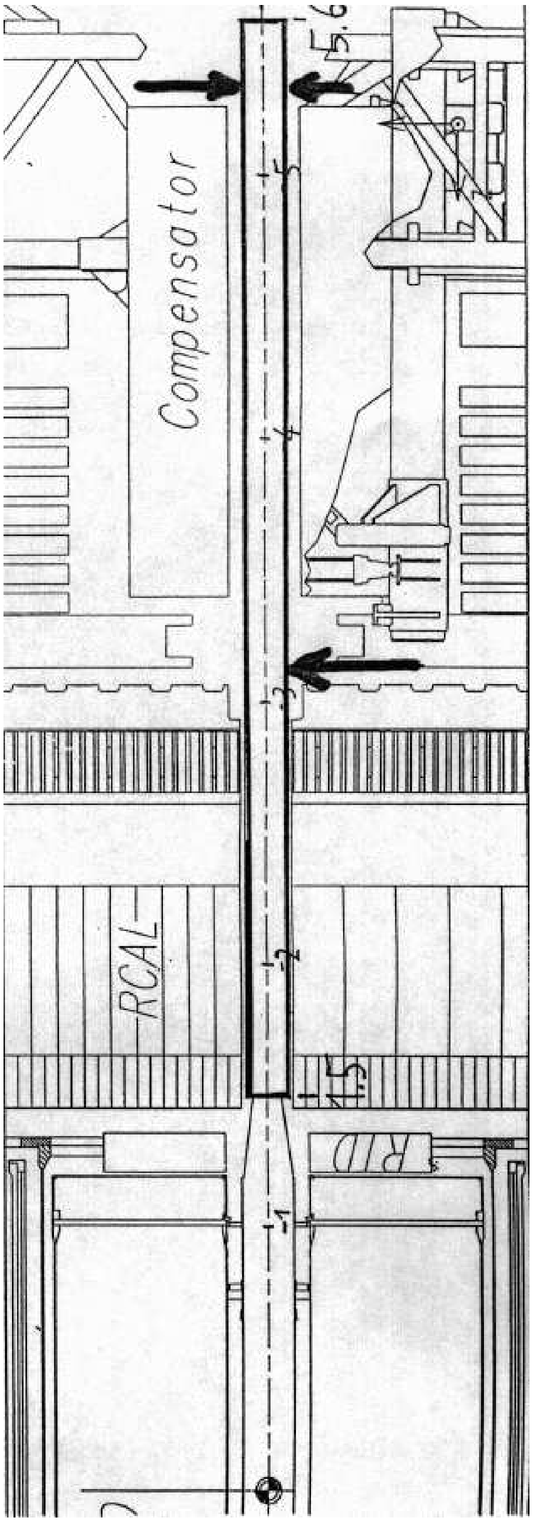

Figure 30: Magnet support on rear side, side view.

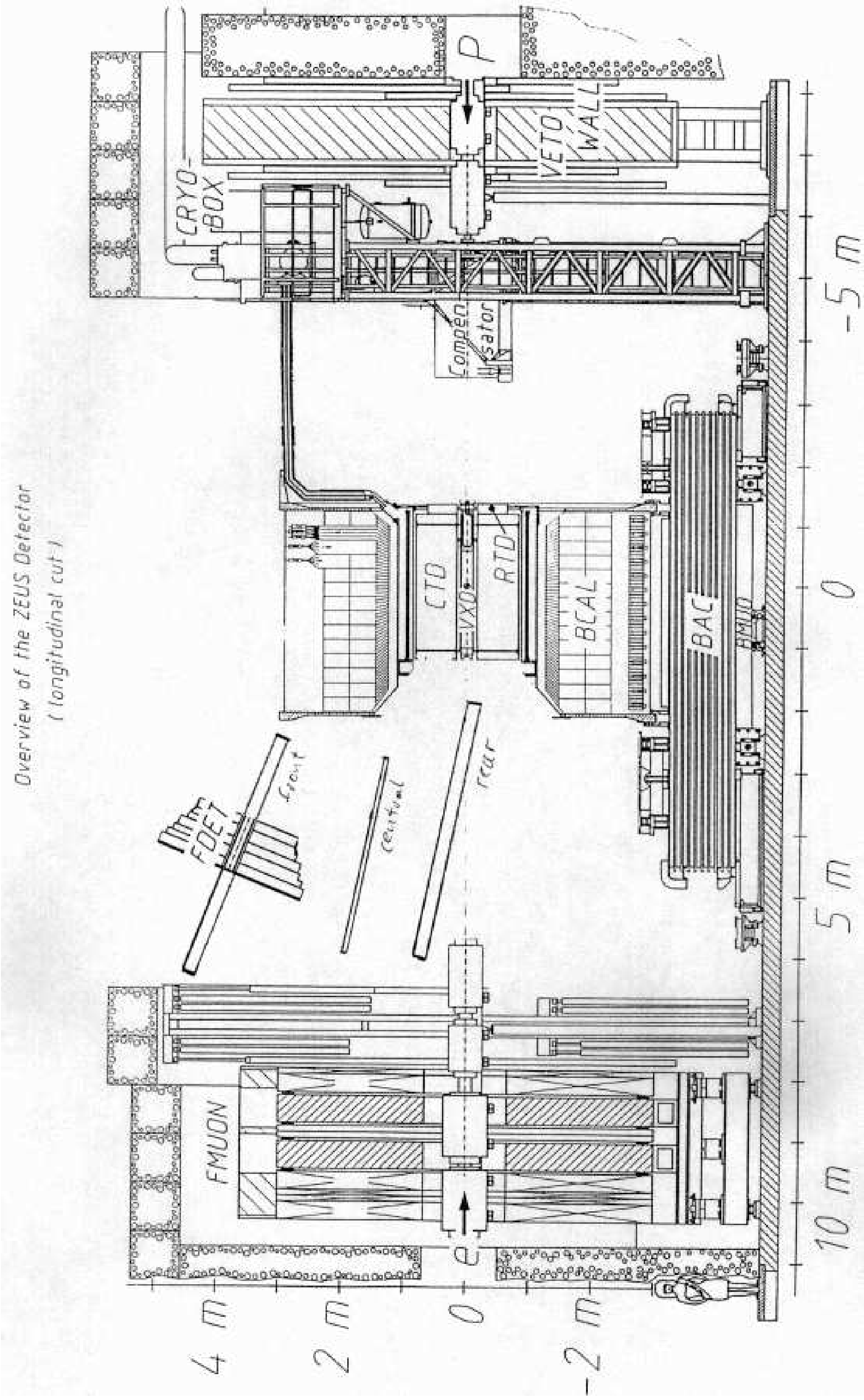

Figure 31: Installation.

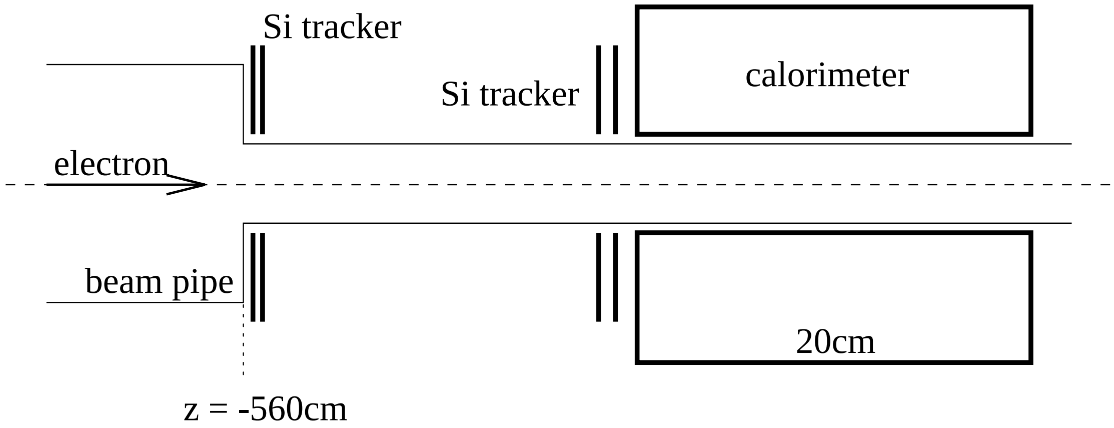

Figure 32: Beam monitoring station, side view.
Conceptual design of a beam monitoring station beyond the separator magnet (side view).

5 Impact of a Luminosity Upgrade on H1

by W. Bartel, H1

Abstract: An attempt has been made to assess the impact of a luminosity upgrade on H1 assuming two warm dipole magnets inserted inside H1. In order to accommodate dipole coils, several ccomponents of the central H1 detector will have to be modified like Silicon trackers, forward and backward tracking chambers, backward Spacal calorimeter, plug calorimeter as well as the support structure for the beam pipe.

5.1 Introduction

High luminosity is the basis for future physics studies with the H1 detector. According to an assessment of the luminosity working group within this workshop, a substantial gain can only be expected by separating the two beams as close to the interaction point as possible by introducing dipole magnets inside the experiments. Such a modification will unavoidably affect the performance of H1. In order to keep the impact on the physics performance as small as possible a scheme was followed which introduces warm dipole magnets with an outer diameter of at most 180 mm.

- The dipole coils with an anticipated outer diameter of 180 mm do not fit into the presently available apertures. Thus H1 has to be reshaped in various places to accommodate the magnets and the beam pipe.
- The deflection of the electrons will create synchrotron radiation, which has to be masked. As a consequence, a new beam pipe has to be designed.
- The luminosity measurement will be affected by the higher level of synchrotron radiation and the modified optics in the interaction point. A new photon calorimeter has to be built.
- The electron tagger needs a new design.
- The space presently taken by the plug calorimeter will be very much reduced and a different instrumentation has to be implemented.
- The detector stations of the FPS have to be moved to different positions.
- The physics performance will change due to the removal of detector elements at small radii, the additional material introduced by the coils and synchrotron radiation absorbers and the change in beam optics.

The detailed studies, which are necessary to investigate the impact of a high luminosity upgrade of H1 were not yet completed by the time of this report so that only a preliminary conclusions can be presented.

5.2 Mechanical installation

A three dimensional view of the H1 detector is displaed in Fig. 33. For a high luminosity interaction region the central beam pipe has to be replaced by a beam pipe surrounded by dipole coils. This device has to fit through the forward aperture of the tank housing the liquid Argon calorimeter, because rebuilding the tank is equivalent to rebuilding H1. This constraint limits the outer diameter to 180 mm.

The Silicon trackers around the beam pipe (CST and BST) are detector elements, which should be kept also for high luminosity operation. Therefore the dipole coil cannot start earlier than $\pm$ 1380 mm from the interaction point, if a symmetric installation of the dipole is maintained as preferred for beam optics considerations.

Having fixed the outer dimensions of the high luminosity dipole magnet a central hole has to be provided, which is wide enough to accommodate it. Thus the central modules of the backward calorimeter (SPACAL) have to be removed, which can be done by reassembling the calorimeter. Furthermore the backward drift chamber has to be rebuilt with a larger central bore hole. In order to support the beam pipe together with the dipole magnet space has to be gained at the position of the first module of the forward tracking module and at the position of the backward drift chamber. Various options are under discussion including one, where a rigid support structure is integrated into the new backward drift chamber and also the first forward tracking module is modified to support the weight of the magnet.

The H1 beam pipe is now pumped by integrated getter pumps of the order of two meters away from the interaction point. For the new beam pipe with collimators and absorbers it will presumably technically more difficult to provide the necessary pumping power close to the interaction point.

The present version of the high luminosity insert assumes that the compensating solenoid is kept, in order to maintain electron and positron polarisation. The compensating solenoid does not move together with the main H1 detector. Therefore the beam pipe with the dipole has to be installed when the experiment sits in the interaction region. The necessary space for inserting can be gained by temporarily removing the HERA quadrupoles next to the interaction point.

5.3 Synchrotron Radiation

All details on the synchrotron radiation generated in the bends next to the interaction point and the way they could be shielded is outlined in D. Pitzls contribution to this workshop [1].

The strategy to protect the experiment against synchrotron radiation is based on a central beam pipe, which is wide enough to pass the synchrotron radiation fan through the experiment and place the principal absorbers as far downstream as possible. Masks close to the interaction point prohibit then scattered photons from reaching the tracking chambers. First background estimates show that an increase by a factor of about ten in the numbers of photons reaching the central drift chamber is expected compared with the present set up, which leads to still tolerable rates.

According to a preliminary study of a beam pipe design, the central Silicon tracker could be kept as it is with the beam passing off center. The backward tracker has in its present version too small an aperture for the beam pipe. It has to be rebuilt.

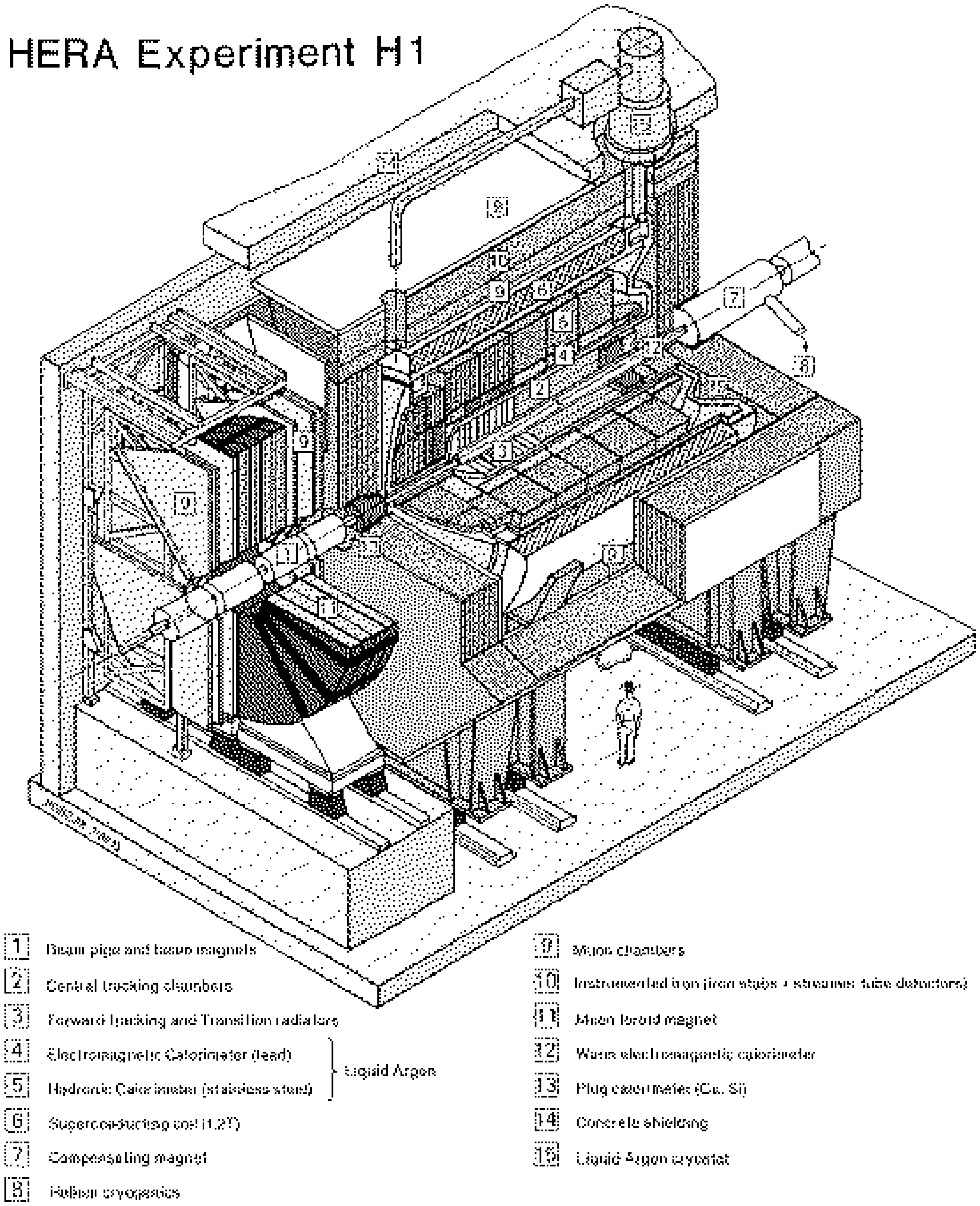

Figure 33: Perspective view of the H1 detecctor.

5.4 Luminosity Measurement

The accuracy of a luminosity measurement by observing ep bremsstrahlung will be degraded in the proposed high luminosity scheme. Two items contribute. First the photon counter due to the larger beam divergence at the interaction point will accept only between 60 and 70% of all bremsstrahlung photons compared with 95% in the prestent set up and second due to the high level of synchrotron radiation the absorber thickness in front of the photon detector has to be increased thus leading to a bad energy resolution. Preliminary studies indicate that the luminosity measurement may not be better than 5%.

At high luminosity, however, other reactions with well known cross sections may be used for normalisation like QED Compton scattering.

In measuring luminosity and for tagging photoproduction events electron taggers are employed. With the new design of the interaction region appropriate new positions for these devices have to be found.

5.5 Plug Calorimeter

The space presently occupied by the plug calorimeter will widely be taken by the forward dipole coil. In addition the material in front of the calorimeter represented by the coil will be too big for a useful energy measurement. Thus a new design for the forward instrumentation has to be made.

Although the calorimetry in this area will be poor it cannot be dropped completely, because another important feature of the plug calorimeter has to be maintained. It provides a timing signal, which is used to suppress background events from beam gas and beam wall scattering.

5.6 Forward Proton Spectrometer

The forward proton spectrometer (FPS) employs the HERA machine magnets downstream of the interaction point for a momentum measurement of small angle protons. Changing the focusing properties of the beamline requires new positions for the detector stations. As an example, 820 GeV protons are most favourably observed at a position, where the phase advance with respect to the interaction point is close to $\pi/2$. The new positions can only be determined after having defined a realistic beam optics scheme. Furthermore it has to be observed that apertures are large enough not to cut into the acceptance of the spectrometer.

Besides these pure geometrical considerations, which have to be observed, the physics performance of the FPS will be affected by the strong focusing and consequently large beam divergence at the interaction point. The transverse momentum thus introduced into the interaction will go up from presently 70 MeV to 160 MeV, which is already close to the natural transverse momentum in diffractive processes of about 350 MeV.

5.7 Physics Performance of H1

The main impact of a high luminosity intersect on the physics capability of H1 is due to the insertion of a massive coil close to the interaction point, which will obscure the region of small angnes (smaller than 100 mrad) in the forward and backward regions. In particular the physics at very low Q^2 ($Q^2 \leq 2\ GeV^2$) and diffractive physics with rapidity gaps above $\eta \geq 3$ will affected. We may, however, assume that by the time the HERA luminosity will be upgraded some 100 pb^{-1} will have been accumulated with the present configuration so that most of these investigations have come to an end. Detailed Mt Carlo studies on the performance of H1 in a high luminosity environment are under way. It is, however, unlikely the main conclusions will change.

By the time H1 and HERA could be upgraded most of the physics processes with large cross sections will have been studied and higher luminosity will be vital for H1 to surwive. Physics topics, which will come into focus are DIS at high Q^2, electro weak interactions, search for new phenomena and diffractive events with forward going protons at high invariant mass final states.

5.8 Conclusion

Preliminary investigations into an upgrade of the HERA luminosity by introducing a dipole field close to the interaction point inside the H1 detector show that the necessary modifications seem technically feaseble within a reasonable effort. The physics capability of H1 to study ep reactions with the high luminosity machine will not be affected if we assume that the program of large cross section physics is completed by the time of the upgrade. A special effort has to be made to develop a scheme for an accurate luminosity measurement.

An upgrade of H1 and HERA is vital to a physics program beyond the year 2000.

References

[1] D. Pitzl This proceedings

6 Conservative upgrade of the HERA interaction regions

by R. Brinkmann

6.1 Introduction

In this section we discuss the potential for a luminosity upgrade in HERA by modifying the beam optics in the North and South IR's under the boundary condition that the free space for the experiments is left unchanged at $\pm 5.8m$, i.e. without any magnets inside the detector. Such a conservative approach can clearly not provide as much luminosity gain as a more radical lattice modification with separator magnets integrated in the detector, as described in section(...), but the detailed investigation shows that about a factor of two increase in specific luminosity compared to the present optics can be achieved. In this approach, moving the p-beam low-beta quadrupoles closer to the IP is accomplished by the following modifications:

- Reduction of the e-beam bending radius from 1300m (present lattice) to 820m. The critical energy of synchrotron radiation remains unchanged if we limit the e-beam energy to 30 GeV instead of 35 GeV for the original layout.
- Simplification of the e-beam optics by replacing the triplet focussing by a doublet.
- Moving the "BS-type" magnet (used for correcting the influence of the e-magnets on the p-orbit) after the first p-beam focussing element.
- Using a half-quad with "thin" septum plate, as suggested by B. Parker, for the first p-beam focussing element in order to cope with a small beam separation at this position.

The minimum distance of the first p-beam half-quad from the IP is 16.5m with these modifications, down from 27.6m in the present lattice. This allows to reduce the p-beam beta-function at the IP by more than a factor of three. An overview of all relevant parameters is given in table 6. In the following, the beam optics modifications for the electron and proton rings are described in more detail.

6.2 Electron beam optics

The reconfiguration of the e-beam lattice is done by using only existing magnets. The low-beta doublet consists of a pair of QL-quads followed by two QC-quads. As in the present optics, they are positioned off-axis w.r.t. the orbit and act as combined function magnets. The required strengths do not present any problem and the available aperture is safely sufficient for the beams and for the synchrotron light (see fig. 34). After the doublet, a BH-dipole is installed which completes the separation angle to 9 mrad at a bending radius of 820m. An important part of this design is the reduction of the horizontal beam emittance by stronger focussing in the arcs (78 deg. per FODO cell instead of 60 deg.). This reduces the aperture requirement for the e-beam and the chromaticity of the low-beta insertion (same beam size at the IP achieved with

	e-beam	p-beam
energy / GeV	27.5	820
number of colliding bunches	176	176
bunch charge N / 10^{10}	4.18	10
emittances $\epsilon_{x,y}/m$	1.8×10^{-8}	
norm. (2σ) emittance $\gamma\epsilon_{x,y}/m$		20×10^{-6}
Beta at IP $\beta^*_{x,y}/m$	5.5, 0.22	1.8, 0.35
beam size $\sigma^*_{x,y}/mm$	.180, .0324	.178, .0355
tune shift $\Delta Q_{x,y}$	.040, .039	.0017, .0004
specific lumi $/10^{29} cm^{-2}s^{-1}mA^{-2}$	10.7	10.7
gain factor	2.14	2.14
luminosity $/10^{31} cm^{-2}s^{-1}$	4.6	4.6

Table 6: Parameters for the conservative IR upgrade

a larger β^*_x). It will also be beneficial for synchrotron light collimation, since the collimators can be moved closer to the beam axis. Matching of the low-beta insertion to the remaining straight section is in principle no problem, but so far no attempt has been made to include the boundary conditions of spin matching. The optics in the vicinity of the IR is shown in fig.35. The available aperture at the position of the first p-beam half-quad is rather small in the horizontal plane (although sufficient for luminosity operation) and an injection optics with relaxed beta-functions will be required to provide enough acceptance for off-axis accumulation.

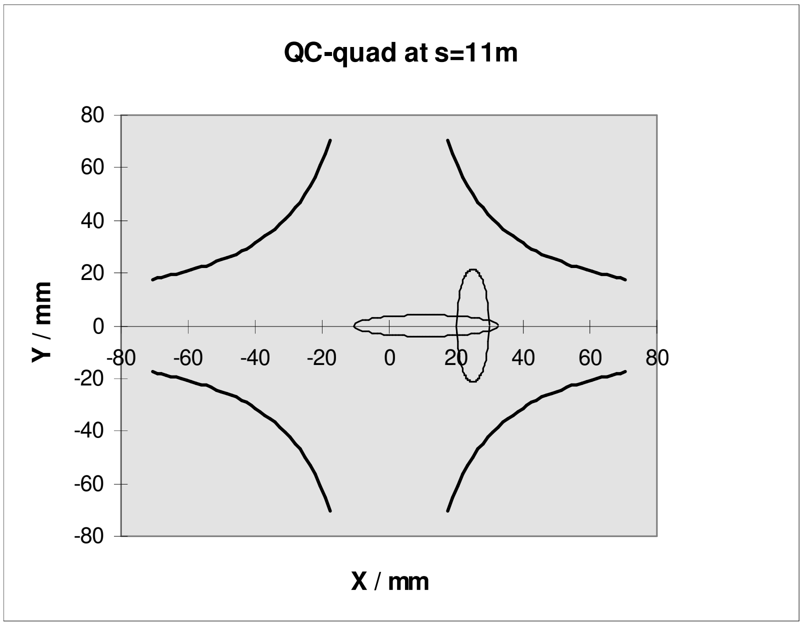

Figure 34: Beamsizes (12-sigma) at the end of the e-beam doublet.

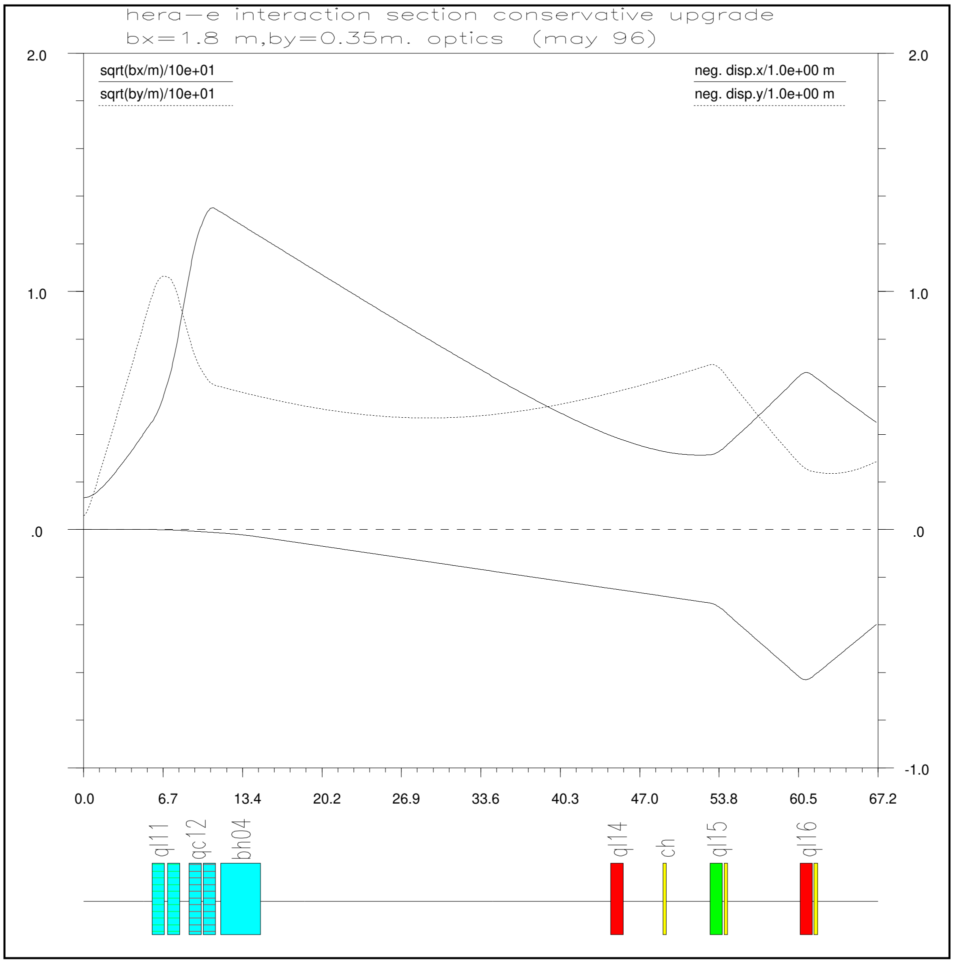

Figure 35: Electron beam optics in the upgraded IR.

6.3 Proton beam optics

The first element of the p-beamline is a "Parker septum half-quad" with an aperture radius of 40 mm. The beam separation is sufficiently large to provide a 12-sigma aperture for both beams (see fig. 36).

The strength of this half-quad corresponds to a pole-tip field of 8 kGauss, which seems conservative. The other p-beam focussing elements are recycled magnets from the present lattice (QS- and QR-magnets) and provide more than the required 12-sigma aperture. A BS-type dipole magnet, with reduced length, is installed between the "Parker-quad" and the first QS-magnet. This correction magnet is foreseen to compensate the variation of the influence of the e-magnets on the p-orbit during the e-ring energy ramp. It is assumed that the p-magnets have to be slightly re-adjusted if the machine is switched from electron to positron operation

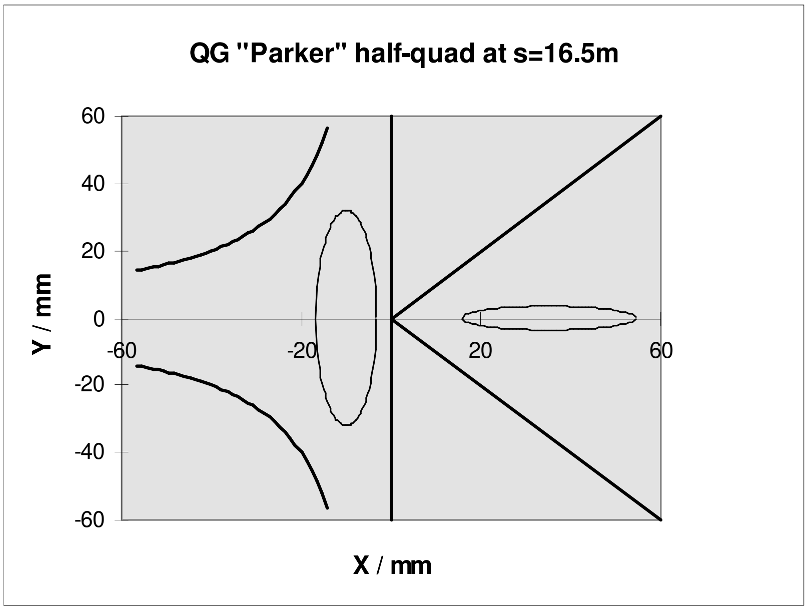

Figure 36: Beamsizes (12-sigma) at the beginning of the Parker half-quad

(or vice versa). The peak beta-functions in the proton optics are even slightly lower than in the present optics and the chromaticity compensation is not a problem. The modified proton optics has been matched to the periodic arcs, which is possible with the available correction quadrupole strengths.

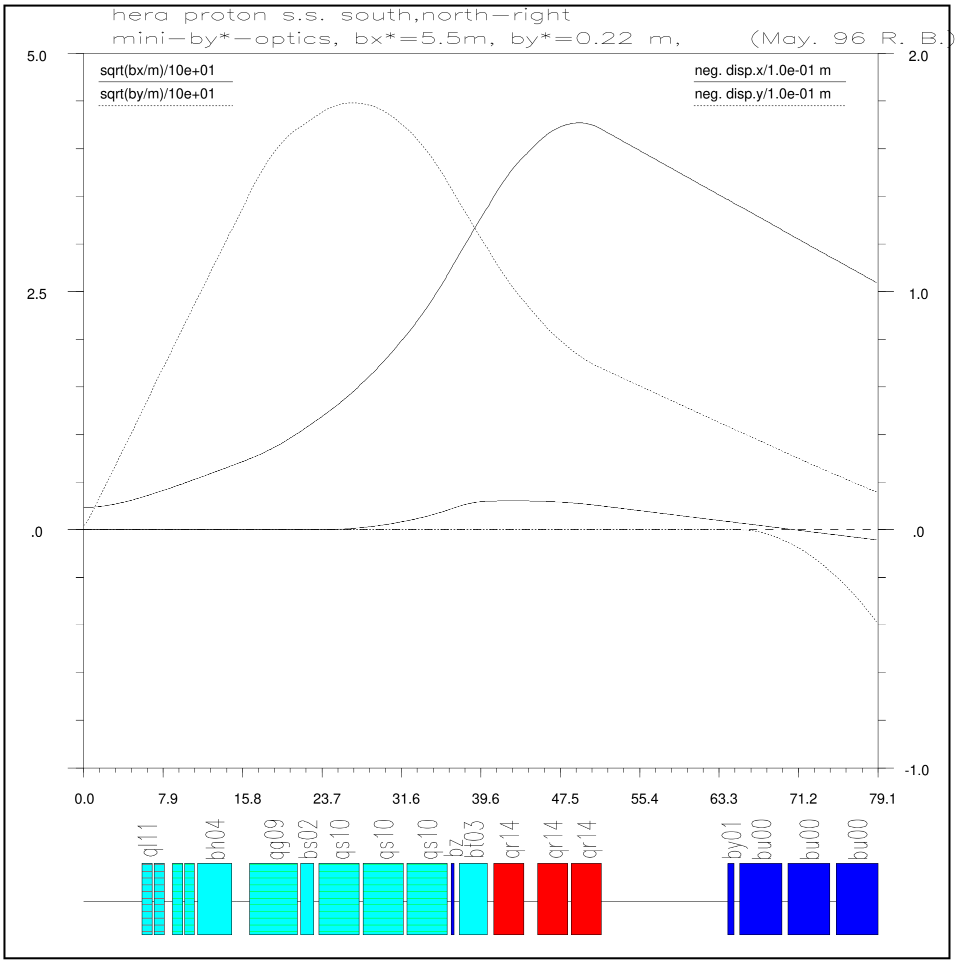

Figure 37: Proton beam optics in the upgraded IR.

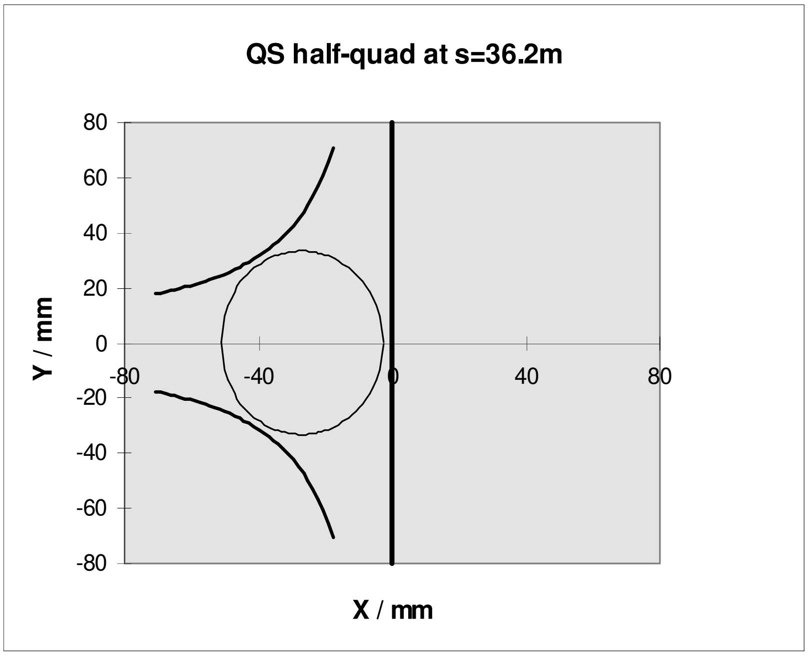

Figure 38: Proton Beamsize (12-sigma) at the end of the 3rd QS half-quad.

6.4 Conclusion

The potential for an IR upgrade in HERA based on an essentially unchanged concept for the beam separation and using many of the presently installed components has been investigated. The proposed beam optics leaves a free aperture of 12 sigma for the p-beam. Tightening the aperture somewhat (say, to 10 sigma) seems conceivable and would allow to bring the vertical beta-function at the IP down to the bunchlength (15 cm) limit, with another 20% gain in luminosity. We therefore conclude that an improved lattice which maintains a free space for the experiments of $\pm$ 5.8 m has a luminosity gain potential of up to a factor of 2.5. Taking into account that such a modification requires a relatively small amount of new components, it seems conceivable that it could be done as the first step of an IR-upgrade on a rather short time scale, and that the full upgrade (as desribed in section (...)) with another gain of about 60 % in luminosity could be viewed as the 2nd step.

7 DESYIII Beam Brightness Limitations

by W. Ebeling and J. Maidment

7.1 Introduction

Desy 3 is the first circular machine in the HERA-p injector chain. It accelerates protons from 50 MeV (kinetic energy) to a momentum of 7.5 GeV/c. Injection into this machine is from a linear accelerator which provides H^- ions. These are stripped using a thin foil which in principle allows accumulation of protons with negligible increase in transverse emittance. Typically the linac pulse current and duration are 10ma and 35μs respectively thus allowing ten turns to be injected. The resultant coasting beam is quasi-adiabatically captured in 11 bunches establishing the longitudinal separation subsequently required in HERA. Acceleration takes approximately 2 seconds. Ten of the 11 bunches are transferred to Petra. The maximum current achieved to date is roughly 200 ma, corresponding to 20% above the HERA single bunch design intensity. In routine operation about $1.1{\cdot}10^{11}$ protons per bunch are accelerated.

7.2 Transverse Space Charge Effects

Space charge is considered to be the most significant effect limiting the beam brightness. It is convenient to use the expression for space charge detuning namely:

$$\Delta Q_v = \frac{N r_p F}{\pi \varepsilon_v \left(1 + \sqrt{\frac{\varepsilon_h}{\varepsilon_v}}\right) B_f \beta \gamma^2}$$

Where N is the total number of circulating protons, F (~ 1) takes account of the image forces, B_f is the bunching factor (average/peak current) and ε is the transverse normalised emittance (2σ). The expression shows that the tune shift (which in reality characterises a spread) is greatest at low energy and increases linearly with brightness.

Measurements of the beam emittances as a function of accelerated current both at peak energy ("flat top") and shortly after injection ("flat bottom"). Figure 39 shows the results for the vertical emittance and Figure 40 those for the horizontal emittance. The solid lines correspond to flat top and the dotted lines to flat bottom. The increase of emittance with increasing beam current is clearly apparent as is also the increasing blow-up from injection to peak energy. More detailed measurements of the variation with time during the cycle together with the corresponding bunch length allow the implied tune shift to be calculated. The (vertical) tune shift so derived is shown in Figure 41.

The variation of tune shift is due not only to the increase in energy but also due to emittance blow-up and particle loss. These latter effects cease at around 0.25s at which time the beam momentum is approximately 1 GeV/c.

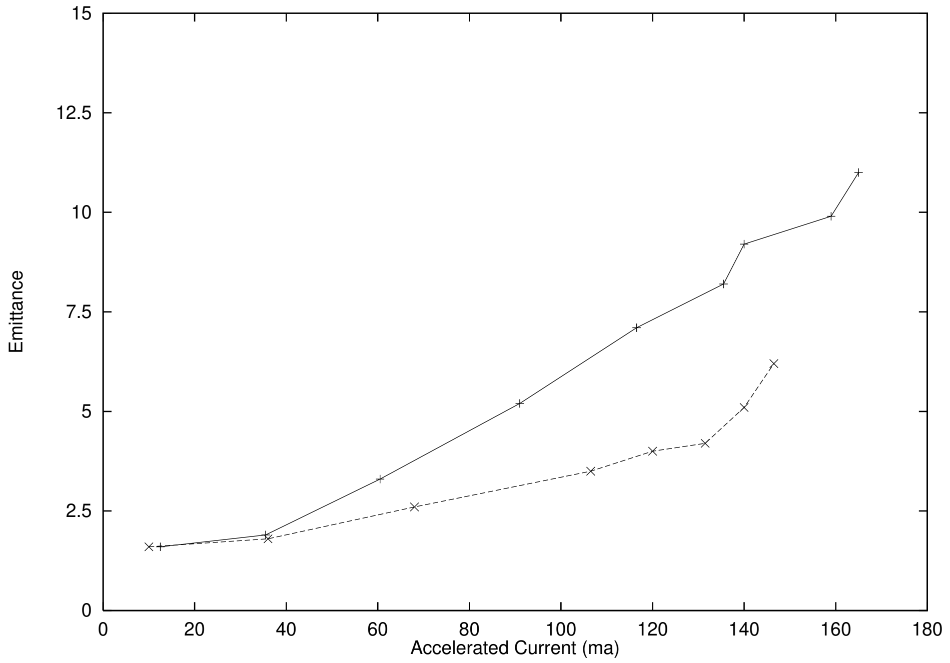

Figure 39: Vertical Emittance vs Accelerated Current

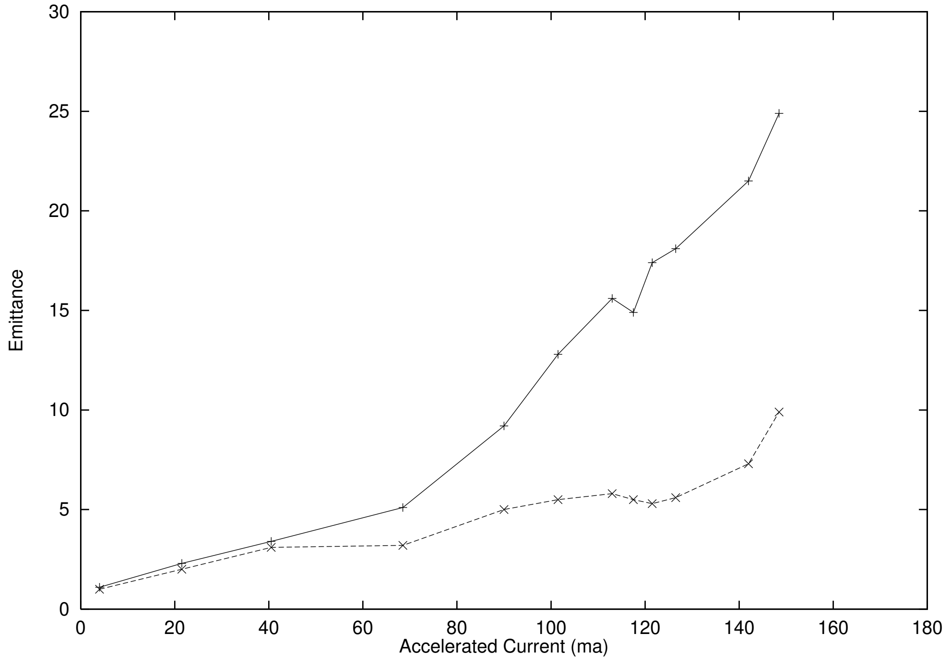

Figure 40: Horizontal Emittance vs Accelerated Current

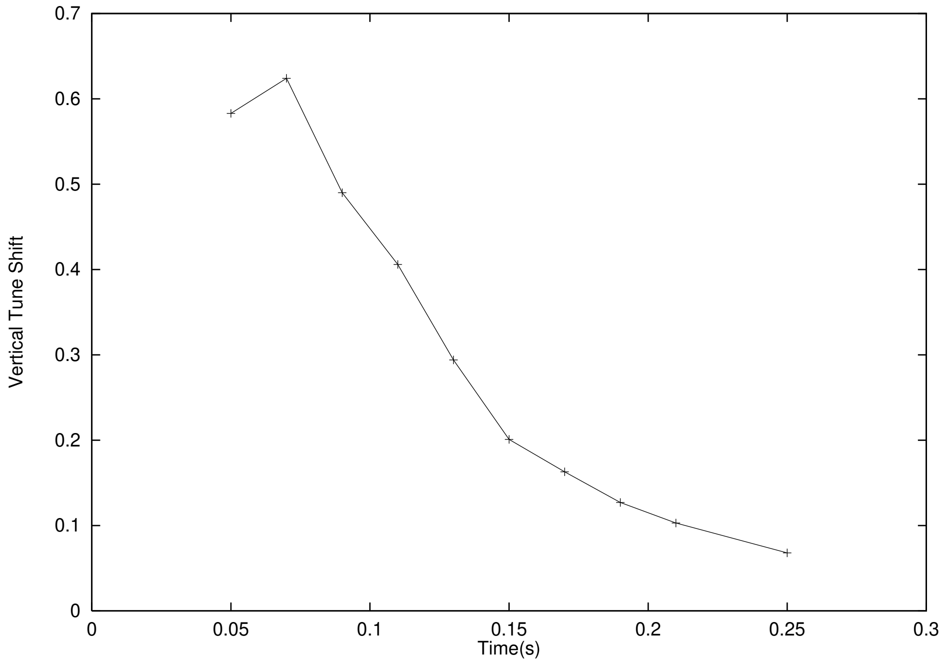

Figure 41: Vertical Tune Shift vs Time

7.3 Future Options

Although there is an ongoing program of machine studies to identify and understand all the contributions to emittance dilution it is clear that space charge is the dominant effect. In this situation an increase in the injection energy would allow potentially brighter beams. Two alternative possibilities have been or are under consideration. One study, in collaboration with INR (Moscow) has proposed an upgrade of the linear accelerator output energy to some 170 MeV. More details of this work may be found elsewhere in this document. In summary this option would require modest modifications to the existing Desy3 systems and yield at most a factor of 2 potential brightness increase.

A further option, namely the use of an intermediate booster, is being investigated in collaboration with IHEP (Protvino). The outline specification is for a 1 Hz repetition rate synchrotron accelerating 2 bunches per cycle to 800 MeV (momentum = 1.46 GeV/c). Five cycles would be used to fill the required 10 bunches in Desy3. Installation of a fast injection kicker system in Desy3 would be required. Use of such a booster may increase the space charge limit in Desy3 by at least a factor of 5.

It is intended that the booster study shall be completed in 6 months. Included will be not only design concepts but also cost estimates. This then allows a decision between the alternative options to be made in mid 1997.

8 LINAC III Upgrade Using a High Gradient Linac

LINACIII Upgrade group; compiled by N. Holtkamp

The conceptual design study which will be presented throughout the next pages is based on a more detailed report which has been worked out in collaboration with the Institute of Nuclear Research in Moscow (Troitsk), the INR. At INR a 600 MeV high duty cycle proton linac is under construction and a proton beam has already been accelerated up to 200 MeV/c [1]. With this expertise in house, the goal of this study was, to investigate the feasibility of an energy upgrade using a higher harmonic accelerating structure which has to be installed in the beam line of the existing LINAC III to the DESY III synchrotron. Given the limited space (length) the maximum energy should be achieved at reasonable investment and operation cost.

8.1 Introduction

Presently the proton linac, which is a 50 MeV Alvarez structure, injects H^- particles into the DESY III proton synchrotron, where multi-turn injection through a stripping foil is used to accumulate sufficient intensity for HERA. This linac is separated into three tanks and powered by a radio-frequency system operating at 202 MHz. The area occupied by the linac and part of the injection beam line which would have to be replaced with new accelerating structures can be seen in 42

The total space available for the installation of the new linac from the end of tank 3 to the injection into the booster synchrotron is roughly 35 m. A scenario which would replace tank 3 in addition and start with a 30 MeV beam to gain somewhat more space for the high gradient structure has been discussed, but will not be presented here. According to the feasibility study a higher harmonic frequency of 810.24 MHz can be used for the upgraded part of the linac. Such a high frequency allows to obtain a large accelerating gradient which will accelerate the H^- beam up to 160 MeV over a distance of $\approx$33 m. This part describes all subsystems of the accelerator leading to a cost estimate for the whole linac.

8.2 Linac III Beam Parameters

The knowledge of the present beam parameters of the Linac III is very important for a suitable design of the upgraded part of the linac. Typically for a low intensity injector into a synchrotron beam profiles and emittances containing 90 % of particles are used. In our case beam emittances containing almost 100 % of particles are used in the design because of the relatively low value of the transverse and the longitudinal acceptance, which is well known for coupled cavity linacs (CCL). Therefore the accelerating and focusing structure of the CCL is designed in order to avoid coupling of the transverse and longitudinal motion as well as non-linear motion. The choice of the harmonic number of the rf system ($\times 4$) of the CCL depends mainly on the longitudinal emittance that can be achieved at the output of the Linac III. The availability of the rf-components of course is a second issue.

In order to determine the emittance from the proton linac precisely, the existing diagnostics equipment in the beam transport line has been used to measure the momentum spread. The harp monitors only provide an rms values which is calculated by fitting a Gaussian curve to the

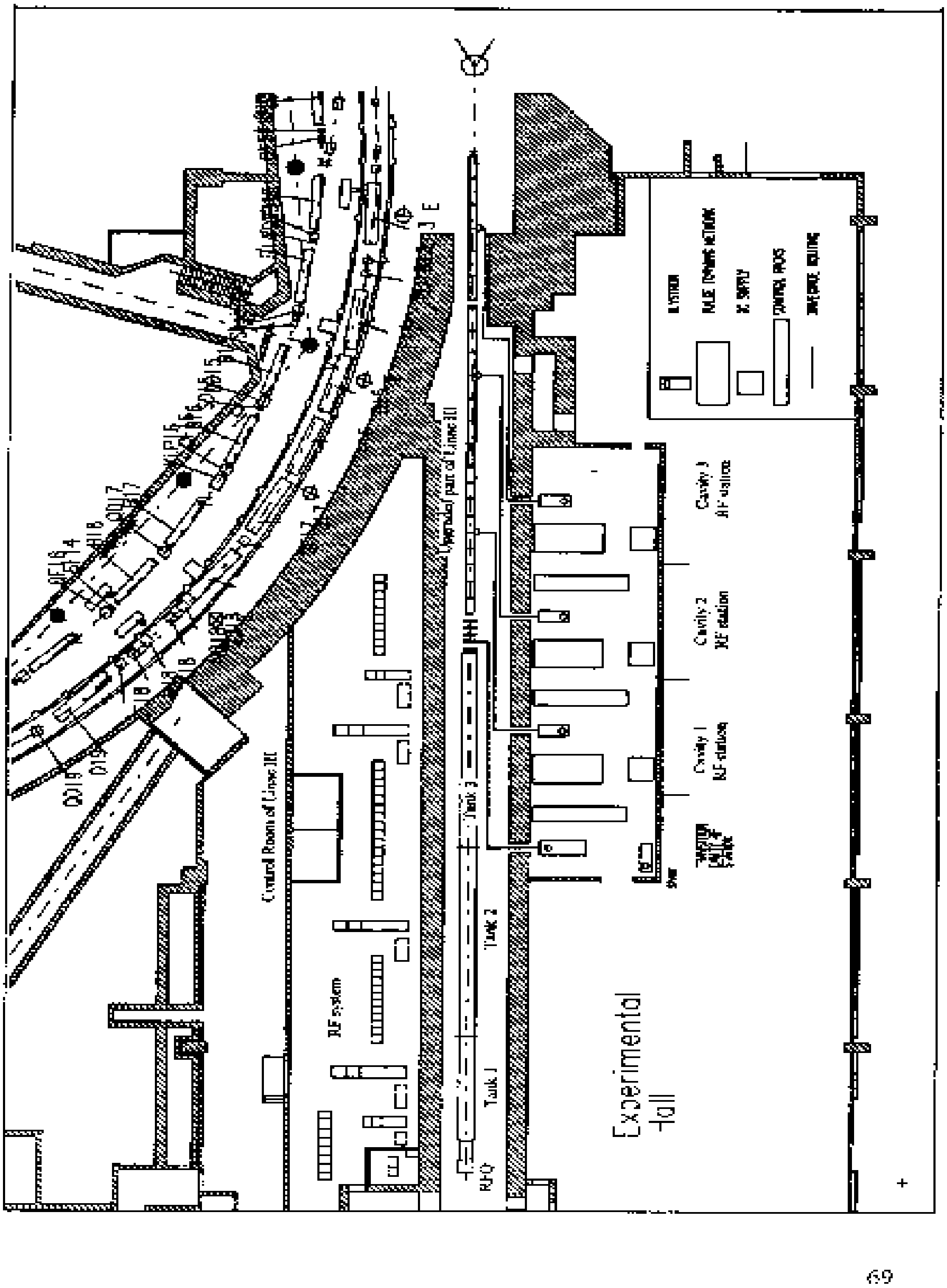

Figure 42: Sketch of the present set-up of the H^- linac and the beam transport line into the DESY III synchrotron.

measured data. A more precise measurement will be possible as soon as the new bunch shape and bunch length and velocity monitors are installed in the linac. From the data available and the tests done with off energy beams be dephasing the debuncher cavity at the end of the linac, it can be concluded that $2.5\times\sigma_{\rm p}$ contains more than 99 % percent of the transmitted particles.

longitudinal emittance data		
long. emittance		ϵ_{eff} / deg×%
rms		1.55
90 %		4.48
Full		9.68
transverse emittance data		
trans. emittance	$\epsilon_x/\pi \cdot mm \cdot mrad$	$\epsilon_y/\pi \cdot mm \cdot mrad$
	2.06	1.81
halo studies $\epsilon_{\mathrm{x,y}}$		
rms	2.1	1.8
90 %	9.6	4.1
≈ 100 %	33	29

Table 7: Longitudinal, vertical and horizontal emittance of the 50 MeV beam from the present LINAC III. These values are used for further studies of the upgraded part of the linac.

The fully reconstructed values which are the bases for further beam dynamics simulations are presented in table 7. Similar measurements have been performed for the transverse phase space. Again, in order to increase the spatial resolution on the harp monitors, the beam position has been swept over the wires of the harps. In addition, to measure the beam halo with better resolution, the beam has been focused at the position of the harp. For the transverse phase space, $4\times\sigma$ can be accepted as a maximum beam size which contains more than 99 % of the particles.

8.3 General Criteria for the Beam Dynamics

The beam dynamics in the linac is strongly related to the choice of the accelerating structure. Generally the energy range between 50 MeV to 100 MeV has been covered by Drift Tube Linacs (DTL). Recent studies in Los Alamos as well as in MRTI (Moscow) lead to the development of more efficient rf-structures to be used for acceleration above 100 MeV/c. This type of structure is based on the Coupled Cavity Structures (CCS). In contrast to drift tube linacs, where focusing can only be achieved by using FODO cells with the focusing lenses inside the large diameter drift tubes, the CCS allows to install the magnets outside of the rf cavities. Especially at a multiple of the present LINAC III frequency fabrication becomes easier, the shunt impedance can be significantly increased and strong focusing can be applied between the cavities. A restriction is given by the ratio of the aperture to cavity diameter and the longitudinal emittance which can be achieved at the end of LINAC III in order to match the beam into the smaller phase acceptance of the CCL bucket. In the energy range to be considered in our case (above 50 MeV) there are no efficient operating accelerating structures other than DTL. However, recent studies carried out mainly at Los Alamos resulted in the development of accelerating structures for intermediate energies for light ions in the range of 20-100 MeV[2]. The structure is a combination of the CCS and the DTL - CCDTL (coupled cavity drift tube linac). The data measured so far with the 50 MeV beam and preliminary studies of the beam dynamics show that even for a 50 MeV beam the operating frequency of the CCDTL can be as high as four times the multiple of the DTL frequency. The use of 810 MHz structures is in favor of high accelerating gradients, first of all, due to the well known Kilpatrick law. The choice of the frequency for the upgraded part of the linac has been done also taking into account the availability of 810 MHz klystrons. These klystrons are available, for example, from Litton with minor modifications from the 805 MHz klystrons which have been developed for the Fermi lab linac upgrade [3]. Concerning the beam dynamics, the bucket area reduction is significant for the transition energy of 50 MeV and the problem of proper matching with the acceptance of the upgraded part must be investigated carefully. In contrast to high intensity, high duty cycle linacs, as for example the Moscow Meson Factory, a number of arguments are in favor of the highest possible frequency:

- high accelerating gradients leading to a large vertical size of the separatrix and larger acceptance.
- almost no restrictions for maximum beam loss which can occur due to the reduction of the bucket phase width, other than the intensity required at DESY III.

Providing these high accelerating gradients by using the fourth harmonics on the other hand results in some disadvantages:

- Smaller longitudinal acceptance with respect to the DTL one.
- High accelerating gradients cause coupling of longitudinal and transverse motion in combination with transverse emittance growth.

These effects are more suppressed if the transition energy between the DTL and CCL is low. For all operating two-frequency accelerators (LAMPF, Fermilab, INR (Moscow)) the transition energy is close to 100 MeV which is essentially higher than in case of the proposed

LINAC III upgrade. Therefore the design of the CCL is strongly dependent on the available beam parameters.

Both transverse and longitudinal motion of the particles require a transition region (TR) at the output of the present DTL. Here, the longitudinal emittance has to be matched in order to decrease beam phase spread. In addition beam matching in the transverse phase planes has to be provided, because the periodic length of the focusing structure from $2\times\beta\lambda_0$ to $4\times\beta\lambda_0$ has to be changed, with λ_0 being the wavelength of the DTL operating frequency.Beam diagnostics and steering will be provided at the TR as well.

A number of aspects are carefully investigated for the choice of the accelerating and focusing structure. Following the development of the CCDTL structure, the decision was made to base the upgraded part of the linac on a combination of the CCDTL structure and the more conventional CCL structure. The accelerating cavity consists of $\approx$100 accelerating gaps both for the CCDTL and CCL. To provide proper beam focusing the number of the accelerating gaps per focusing period has to be chosen carefully. Special attention has been given to the choice of inter-section lengths. [1] It is obvious that this length must be as small as possible from the point of view of longitudinal beam motion. In practice nevertheless the length is mainly determined by the installation of focusing lenses, steering magnets as well as beam instrumentation. For operating linacs based on the CCS this space is an odd multiple of $\beta\lambda_0/2$ and a minimum length of $\beta\lambda_0/2$ has been realized for example in the Fermilab linac upgrade. In the energy range of 50-100 MeV this length is not sufficient in order to fit the equipment mentioned before and therefore we decided to choose an inter-section length for the CCDTL cavities equal to $2\beta\lambda_0$. For the CCL this distance is $3\beta\lambda_0/2$.

The considerations presented here resulted in a linac design with 10 accelerating sections and 9 coupling bridges in the CCDTL and 6 accelerating sections and 5 bridges in the CCL. Using the available length of 33 m three accelerating cavities (tanks) can be installed in the beam line. Each cavity is powered by a separate klystron. One CCDTL cavity allows to achieve an energy of 90 MeV and the other two cavities, which are based on the CCS, accelerate the beam up to 160 MeV. The design of the CCS has been made assuming that each accelerating section consists of 16 cells.

For the focusing structure a FODO lattice has been designed. Although it is well known that the FDO structure in the high energy part of the linacs has some advantage from the point of view of transverse beam dynamics, we reject this version. Using the doublet requires longer drift space between the sections which results in a reduction of the longitudinal acceptance. In addition the FDO structure requires a two times higher magnetic field. For our application the FODO structure seems the only solution due to transition from 202.5 to 810 MHz at a comparatively low beam energy.

[1] For the study we assume as well that a cavity consists of accelerating sections coupled by rf bridges, which has some impact on the geometry.

8.4 Accelerating structure

8.4.1 Possibilities for the Accelerating Structure

The choice of the accelerating structure strongly depends on particular requirements of the linac. We are interested in maximum energy gain with the limited space available. The maximum gradient depends on tolerable maximum electric field at the structure surface which is determined by the sparking rate and the reliability of linac operation, assuming that a given fraction of beam pulse will fail due to breakdown. Based on research work [3], performed in FNAL, and strongly referring to the successful experience [4], we have limited the following considerations to a maximum value of the electric field on the surface $\mathrm{E_s max} = 1.35\,\mathrm{E_k}$, where $\mathrm{E_k}$ / [MV/m] is the empirical Kilpatrick sparking limit:

$$\mathrm{f} = 1.643 \cdot \mathrm{E_k^2} \cdot exp(-8.5/\mathrm{E}) \tag{8}$$

where f is the operating frequency in MHz. For a frequency of 810.24 MHz the Kilpatrick limit $\mathrm{E_k}$ is 26.1 MV/m. With such a high frequency, focusing lenses can not be mounted into the accelerating structure and multi-section design of an accelerating system with focusing elements placed between sections must be considered. Here two main options - a Drift Tube Linac (DTL) structure and a Coupled Cell Structure (CCS) has been considered. The DTL structure was considered in a Bridge Coupled DTL (BCDTL) version [5] with the accelerating cavity consisting of several short sections and each section has 6 accelerating gaps. A general review of CCS has been done, for example, in the [6]. All Coupled Cavity Structures (compare figure 43), - the Side Coupled Structure (SCS), the Disk And Washer (DAW) structure, the Annular-ring Coupled Structure (ACS) and the On-axis Coupled Structure (OCS), have practically the same values for the effective shunt impedance $\mathrm{ZT^2}$. Also for the range of particle velocities between $0.3 \leq \beta \leq 0.55$, similar properties with respect to the maximum electric field at the surface $\mathrm{E_{max}}$ can be expected and all of them operate with standing wave field in so-called $\pi/2$ mode. These structures mainly differ in the value of the coupling constant and geometric design. It is well known, that for protons the energy range of 50 to 200 MeV is the called intermediate region for accelerating structures. The rf efficiency of the DTL structure decreases dramatically beyond the energy of 100 MeV. All the details of the DTL study can be found in ref. [7]. For several reasons, the option of using a DTL for particle velocities of $\beta \leq 0.43$ was rejected. On the other hand, the rf efficiency and using a high gradient in a CCS are favorable for energies larger than 100 MeV but they are quite inefficient at low energies. An interesting proposal has been made recently at Los Alamos [2]. To improve the parameters of a CCS in the low energy region, additional drift tubes have been introduced into the accelerating cells. With this geometry a combination of the high efficiency like in a DTL structure at low β (compare fig. 44) with the mode stability properties of the CCSs is possible.

The CCS option has been considered in more details for three type of CCSs, taking into account that for the low energy range of 50 - 90 MeV an intermediate drift tube will be introduced in the cells. Practically there is no difference in the rf parameters between the SCS and the ACS, but the SCS is more developed and investigated. This type of structure is used in LAMPF, at FNAL for the linac upgrade, in the SSCL linac and in many linacs aiming for industrial and medical applications. The outstanding feature of the DAW structure on the other hand are the large coupling constant and high vacuum conductivity [8]. This structure is used at the INR meson facility linac, in linear accelerating systems for TRISTAN, KEK [9] and in a linac for the SIBERIA synchrotron light source [10]. The most important features of CCSs

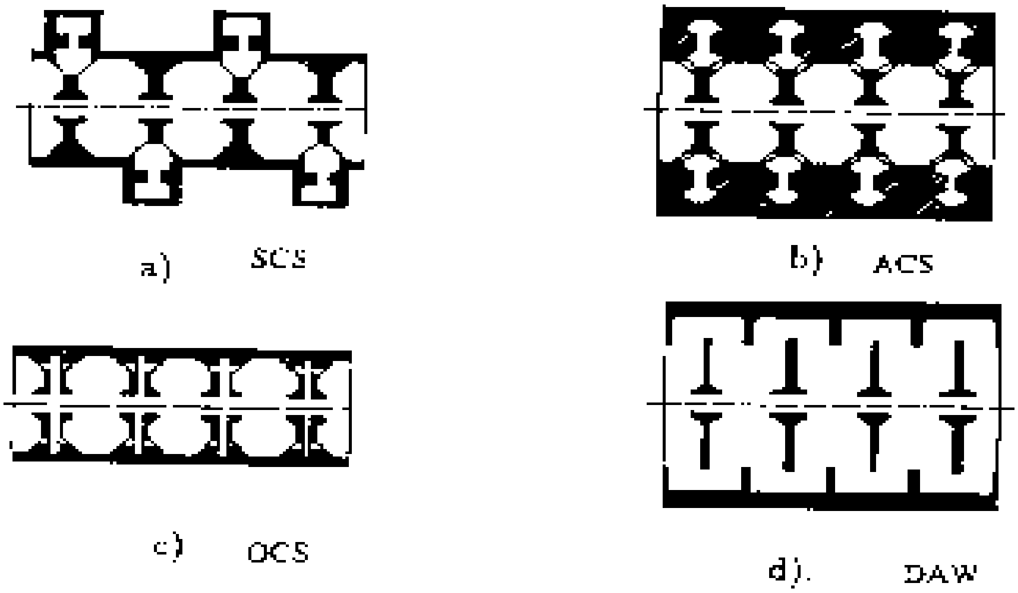

Figure 43: $\pi/2$-mode standing wave Coupled Cavity Cell Structures (CCS). a) - Side-Coupled Structure (SCS), b) - Annular Coupled Structure (ACS), c) - On-axis Coupled Structure (OCS), d) - Disk And Washer structure (DAW).

Structure	Coupling constant	Diameter of the structure (total, with coupling cells)	Remarks	Shunt impedance in the range 50-90 MeV
SCS	(5-7)%	550 mm	Tolerable vacuum conductivity	low
SCSDTL	(1.3- 1.7)%	550 mm	Low coupling constant	satisfactory
DAW	40%	550 mm	High vacuum conductivity	low
DAWDTL	20%	550 mm	Lots of interfering modes	low
OCS	5%	270 mm	Simple design	low
OCSDTL	1.3%	270 mm		satisfactory

Table 8: Parameter study of Coupled Cavity structures for the LINAC III upgrade.

considered for the Linac III upgrade include: (1) mode spectrum without interfering modes in the vicinity of the operating mode, (2)a large value for the cell-to-cell coupling to ensure phase and amplitude stability in long rf-structures with many cells, (3) mechanical properties which allow simple fabrication, (4) simple tuning procedures and an acceptable vacuum conductivity. Table 8 presents a summary of the results. From table 8 one can see that the On-axis Coupled Structure, which has the simplest mechanical design, satisfies most requirements, apart from the strong coupling which is needed because of the large number of cells per structure. Nevertheless, the OCS has the highest potential to increase the coupling constant, because the shunt

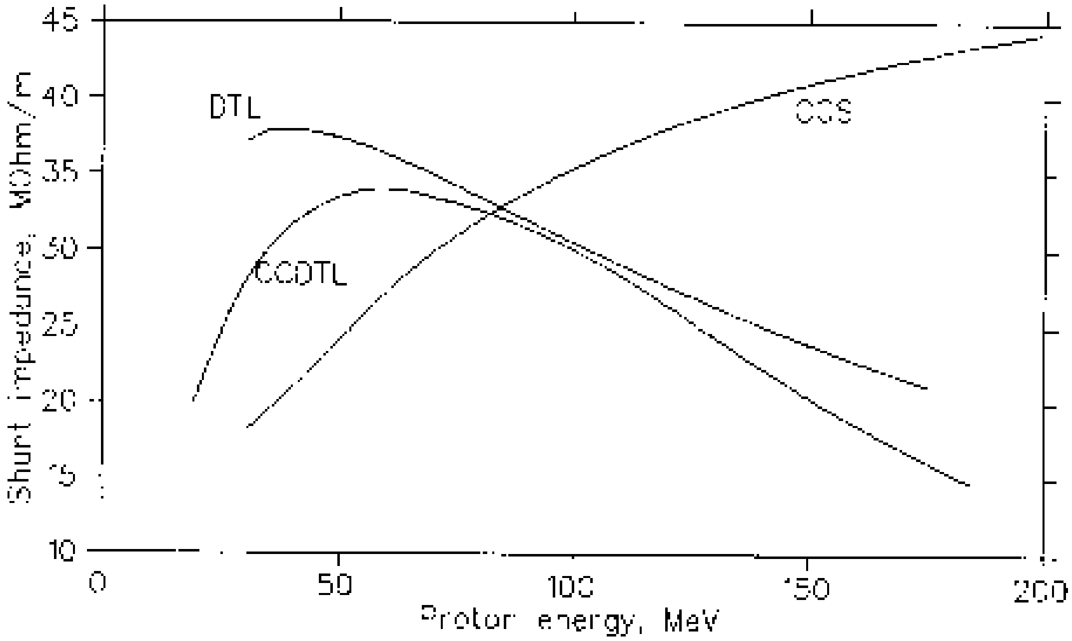

a)

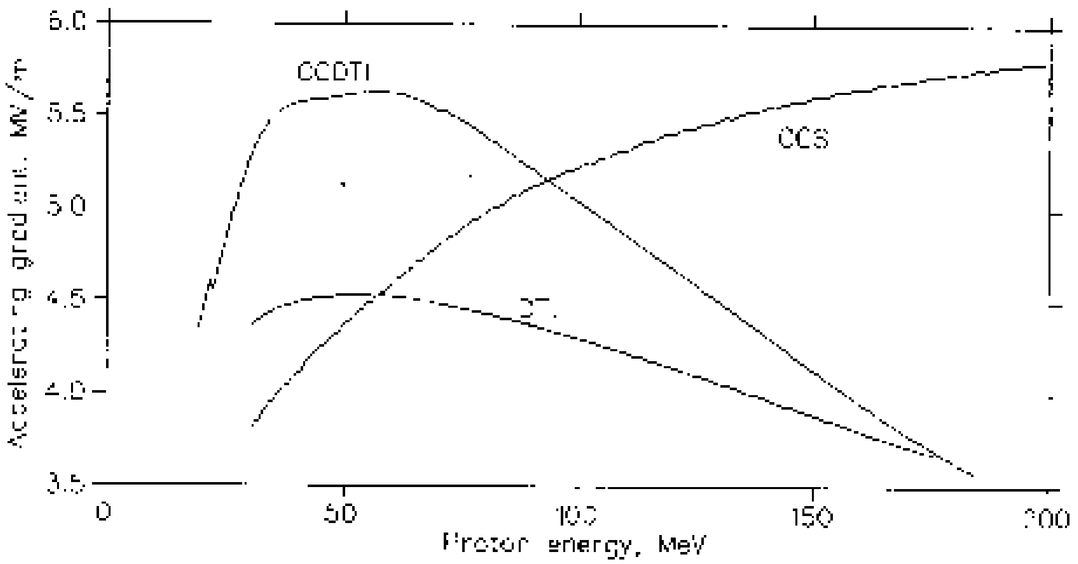

b)

Figure 44: The calculated dependencies of the effective shunt impedance ZT^2 (a) and the corresponding accelerating gradient E_0T for the DTL, CCS and CCDTL structure.

impedance both for the OCS and OCSDTL is a weak function of the coupling as compared to any other known CCS. Therefore the On-axis Coupled Structure is more flexible from this point of view. These reasons lead to the decision to investigate the OCS for the upgraded part of the LINAC III .

8.4.2 Optimization of the Accelerating Structure

The On-axis Coupled Structure has been used mainly for electron linacs at operating frequencies between 1000 - 3000 MHz and comparatively large heat load of a few kW per meter. For a low repetition rate ($\approx$ 60 W/m) of 1 Hz as being used for the LINAC III we do not need internal cooling of accelerating cells. The thickness of the iris can therefore be optimized for maximum coupling and only mechanical constrains have to be considered. A sketch of the OCS and OCSDTL is presented in figure 45. The length of the coupling cell 2 lc is reduced taking into account limitations from the coupling slots and the excitation of the coupling cells. Introduction of the coupling slots reduces the frequency of the cell. For the short coupling cells this influence can be very strong (300 - 400 MHz) and the radius of the coupling cell becomes smaller than radius of the optimal position of the coupling slot. A second point is related to the excitation of the coupling cell. Sparking in the structure can in principle take place in both the accelerating and the coupling cell [11]. The accelerating cells are normally optimized for high gradient operation. In the steady-state regime the coupling cell in a CCSs is not excited at all (or excited at a very low level to provide power flux along the structure for compensation of rf losses in structure walls and for beam acceleration). Nevertheless, significant excitation of coupling cells takes place during transients and may lead to sparking. The maximum electric field value in the coupling cell during such a transient is proportional to the normalized value of $E_{c,max}/\sqrt{(W_c)}$, where $E_{c,max}$ is the maximum electric field on the surface for a given value of the stored energy W_c. In the OCS structure $E_{c,max}/\sqrt{(W_c)}$ is large at two points, at the lower edge of the coupling slot and near the bore hole where the edges have to be rounded as shown in the figure. For both reasons, we have chosen $2\times\mathrm{lc} = 7$ mm for the OCS part and $2\times\mathrm{lc} = 6$ mm for the OCSDTL, keeping at least a reserve of a factor of two in comparison with ratio of $E_{c,max}/\sqrt{(W_c)}$ for the coupling cell in the FNAL SCS design. This has been verified based on 3 D calculations, using MAFIA. The total thickness is $2\times t+2\times\mathrm{lc} = 13$ mm and larger than 7.5 mm web thickness for SCS FNAL design, leading to a reduction in ZT^2 of 10 %. After preliminary optimization the shape of the accelerating cells (Figure 45) has been optimized with a 2 D approximation in more detail for both the OCS and the OCSDTL options. The inside diameter of the cell changes from section to section to compensate for the increasing β, which varies from $0.3 \leq 0.4$ for the OCSDTL and from $0.4 \leq 0.52$ for the OCS.

In order to estimate the required rf-power needed for the cavities, reduced values calculated from a 2 D model have been used. The total reduction of ZT^2 of 17 % for the OCS is given by: 5 % for surface imperfection, 5 % for rf losses in the coupling bridges and 7 % reduction due to coupling slots) and by 25 % (5 % + 4 % + 7 % + 9 %) for the OCSDTL part (with additional 9 % due to rf losses on the stems of the drift tubes). In the OCSDTL part the drift tube is supported by a single stem. At the intermediate tube 6 W of the rf power is dissipated, assuming 1 Hz repetition rate and 35 % from total value of rf losses in the full cell. To simplify the temperature control system and to reduce the rf losses in the stems, we have chosen a water cooled stem with 1.2 cm diameter. The coupling slots have been optimized using the 3 D MAFIA code (Figure 46 and 47). There are two coupling slots at each wall between an

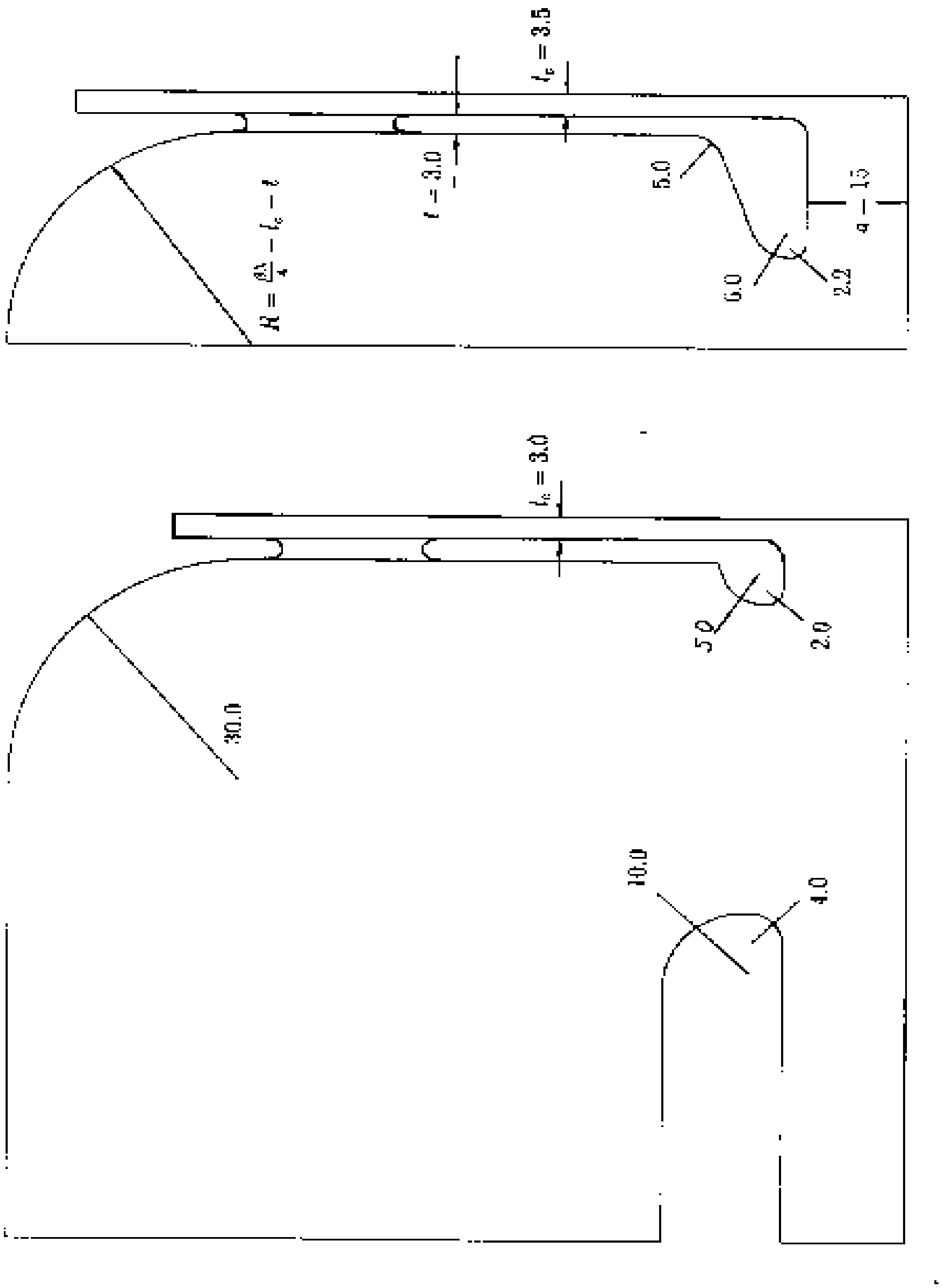

Figure 45: The optimized shape of the cells for the OCDTL structure and the OCS structure is shown. The final parameters od the geometry are given in mm.

accelerating and a coupling cell. The reduction in shunt impedance due to the comparatively large coupling slot is 5 to 7 % for the OCS and 6 to 7 % for the OCSDTL.

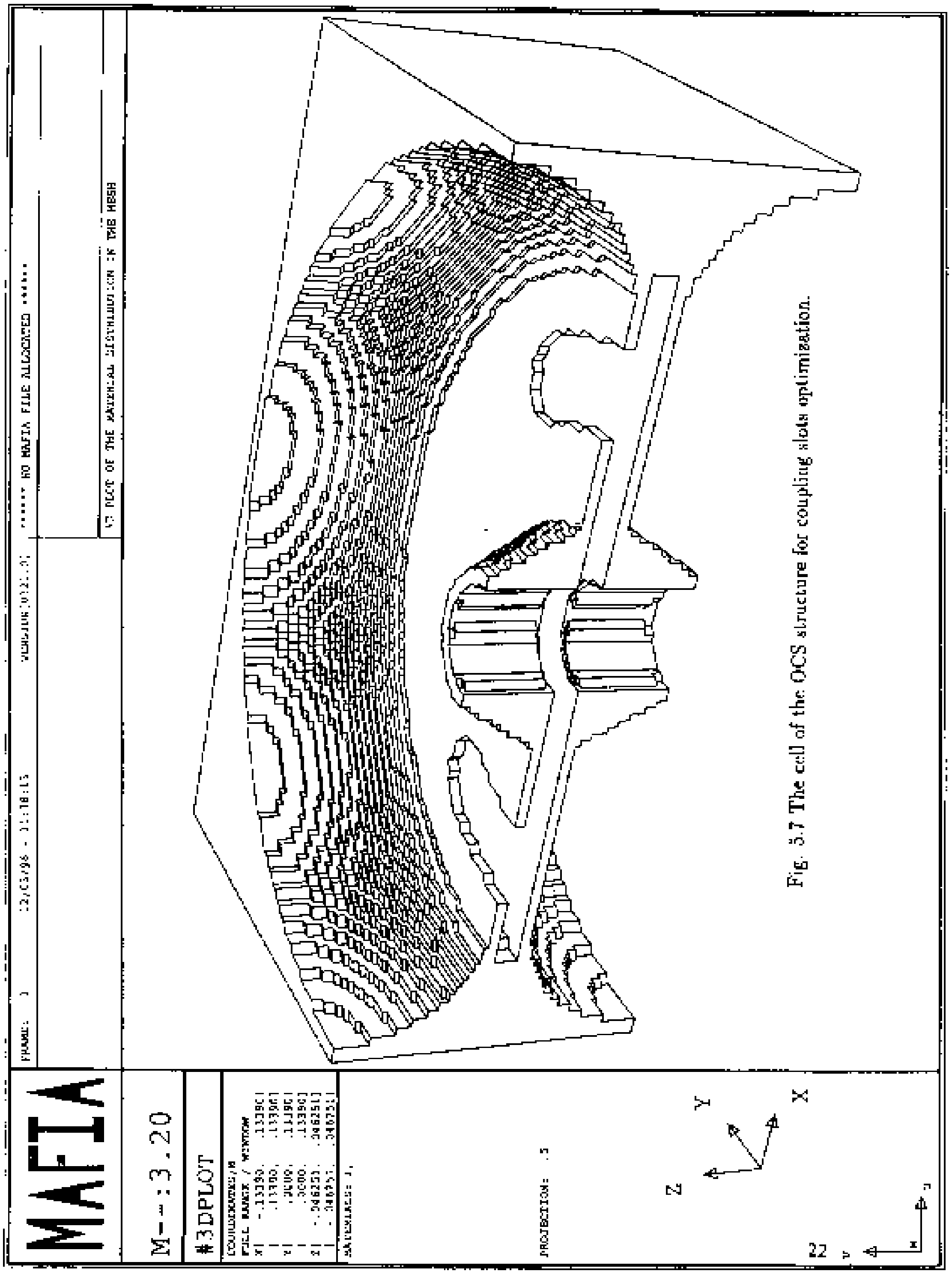

Figure 46: The geometry of the cell of the OCS structure with the coupling slots in a 3D MAFIA model.

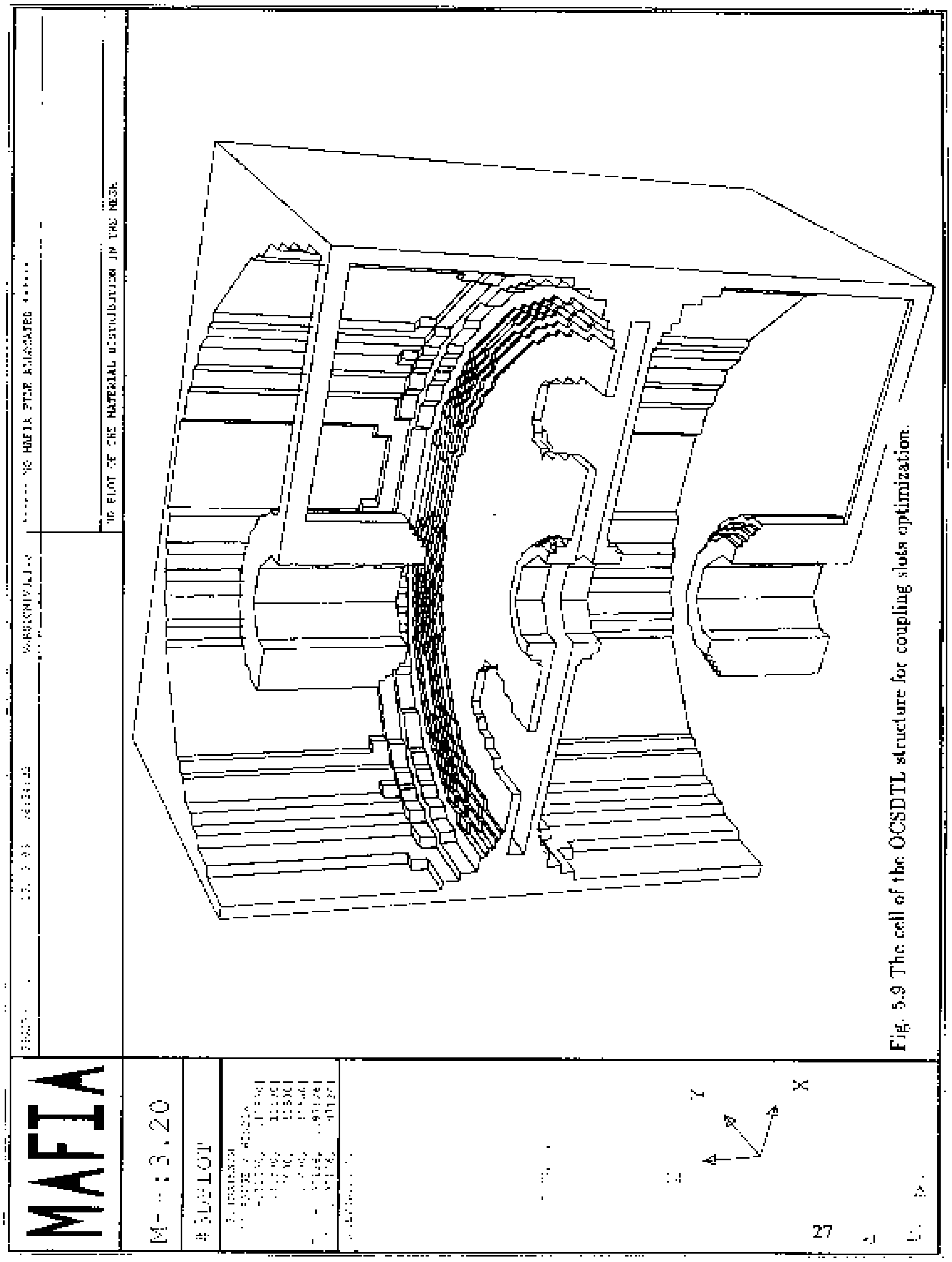

Figure 47: The geometry of the cell of the OCSDTL structure with the coupling slots in a 3 D MAFIA model.

8.4.3 Design of Coupling Bridges

Rectangular bridges operating in the TE_{11n} mode are foreseen to couple the accelerating sections installed in one cavity. This type of bridges was proposed for the accelerating structures of high energy proton linacs, tested at high rf power levels both with DAW and ACS structures [8] and successfully operated in the main part of the INR linac. The original design idea (compare 48) of a TE_{11n} bridge is to provide the space required for diagnostics equipment and can provide both π and $2 \cdot \pi$ phase shift between accelerating sections. The proposed bridges are made from standard rectangular waveguide WR975 and will have a total length of $\approx 2\lambda = 55.6$ cm for the first cavity ($2\beta\lambda$ space between sections, 2π phase shift, TE112 operating mode) and $3\lambda/2 = 83.4$ cm for the second and third cavity ($3\beta\lambda/2$ space between sections, π phase shift, TE113 operating mode). Here $\lambda = 55.6$ cm is the wavelength in a WR975 waveguide at the design operating frequency.

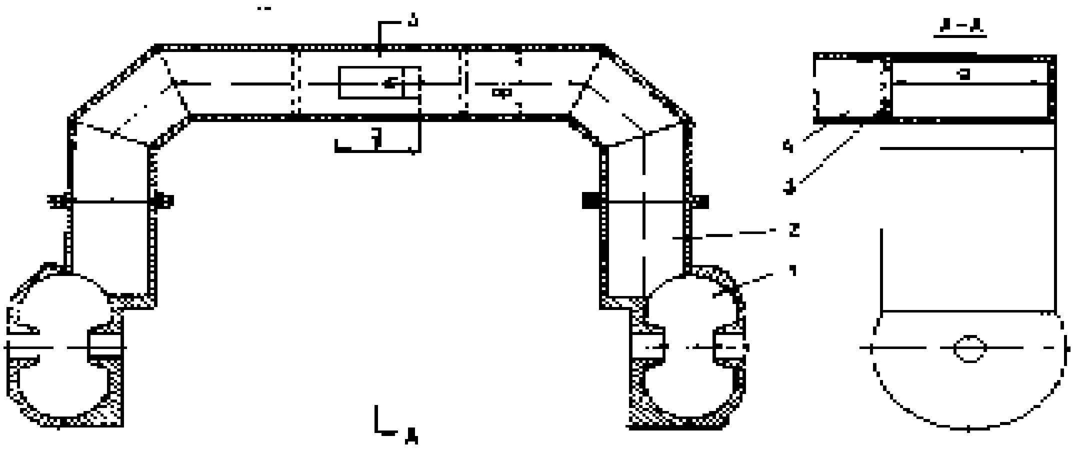

Figure 48: The rectangular bridge with a TE_{10n} operating mode. 1) - the accelerating cell, 2) - the bridge, 3) - matching iris, 4) - rf waveguide

The coupling bridge is attached directly to an accelerating cell and may be considered as an enlarged coupling cell. The additional rf power losses in the bridge is small and does not exceed 3- 5 % compared to the rf power loss in the accelerating sections. The power is fed from the klystron through the middle of on bridge into the cavities. For the tuning of the bridges the plungers which are required are similar to the ones described in [12]. Each bridge coupler is equipped with two plungers, placed symmetrically with respect to the middle of the bridge.

8.4.4 Accelerating Structure Tuning

The tuning of the accelerating cavity consisting of a number of sections connected by the bridges is divided into two more or less independent procedures: first the tuning of the single section and then the tuning of the cavity as a whole. The section tuning procedure involves setting the following values of the parameters: During the tuning procedure, the accelerating mode frequency has to be shifted to the design value under well controlled environmental conditions. Then the coupling mode frequency and the accelerating mode frequency have to tuned to the same value. Simultaneously the field flatness should be approximately 3 %. The complete method of tuning the section, the cavity and the cavity with the bridges as well as the results are described in [13, 14, 15] in more detail. Many of the methods proposed here, have been developed and tested for both the sections and the multi-section cavities during the construction and installation of the INR linac.

Parameter	Cavity 1	Cavity 2	Cavity 3
Initial kinetic energy	50 MeV	85.412 MeV	119.86 MeV
Final kinetic energy	85.412 MeV	119.86 MeV	159.75 MeV
Total length	10.630 m	9.112 m	10.084 m
Frequency	810.24 MHz	810.24 MHz	810.24 MHz
Repetition rate	1 Hz	1 Hz	1 Hz
Pulse length	30 μs	30 μs	30 μs
Beam pulse current	20 mA	20 mA	20 mA
Synchronous phase	-35°	-35°	-35°
Number of sections	10	6	6
Number of cells per section	4	16	16
Type of structure	OCSDTL	OCS	OCS
Transverse focusing structure	FODO	FODO	FODO
Intersection drift	$2\beta\lambda$	$3/2\beta\lambda$	$3/2\beta\lambda$
Section length	$6\beta\lambda$l	$8\beta\lambda$l	$8\beta\lambda$l
Length of focusing period	$16\beta\lambda$	$19\beta\lambda$	$19\beta\lambda$
Cavity bore radius	1.5 cm	1.5 cm	1.5 cm
Power consumption	9 MW	8.5 MW	9.0 MW
copper loss	8.288 MW	7.816 MW	8.196 MW
beam power	0.708 MW	0.689 MW	0.798 MW

Table 9: Main parameters of the upgraded linac.

8.4.5 The Beam Dynamics Study

The accelerating structure geometry has been generated using the functions of the effective accelerating gradient $\mathrm{E_0}T$, the shunt impedance $\mathrm{Z_{eff}}$ and the gap ratio α_{g} with respect to the relative beam velocity β as being obtained from the rf structure design calculations. The properties of the focusing structure have been compared for two different schemes: FODO and FDO. In Figure 49 a minimum for the maximum value of the transverse Courant-Snyder function β_{tr}, the transverse phase advances Φ_{tr} per focusing period and the required quadrupole gradients G are plotted versus the number of accelerating cells per section. The calculation have been done for a focusing period at the beginning of the upgraded part of the linac.

8.4.6 Segmentation of the Structure

Using the functions $\mathrm{E_0T}(\beta)$, $\mathrm{Z_{eff}}$ (b), $\alpha_{\mathrm{g}}(b)$ for the CCDTL and the OAS and taking into account the rf power consumption as well, the structure was divided into three cavities. A list of main parameters for each cavity is given in the table 9.

Due to the different transverse periodicity of the focusing structure in cavity 1 ($16\beta\lambda$) and cavity 2 ($19\beta\lambda$), transverse matching is necessary between these two cavities. The matching can be provided with the help of the four last quadrupole lenses of cavity 1.

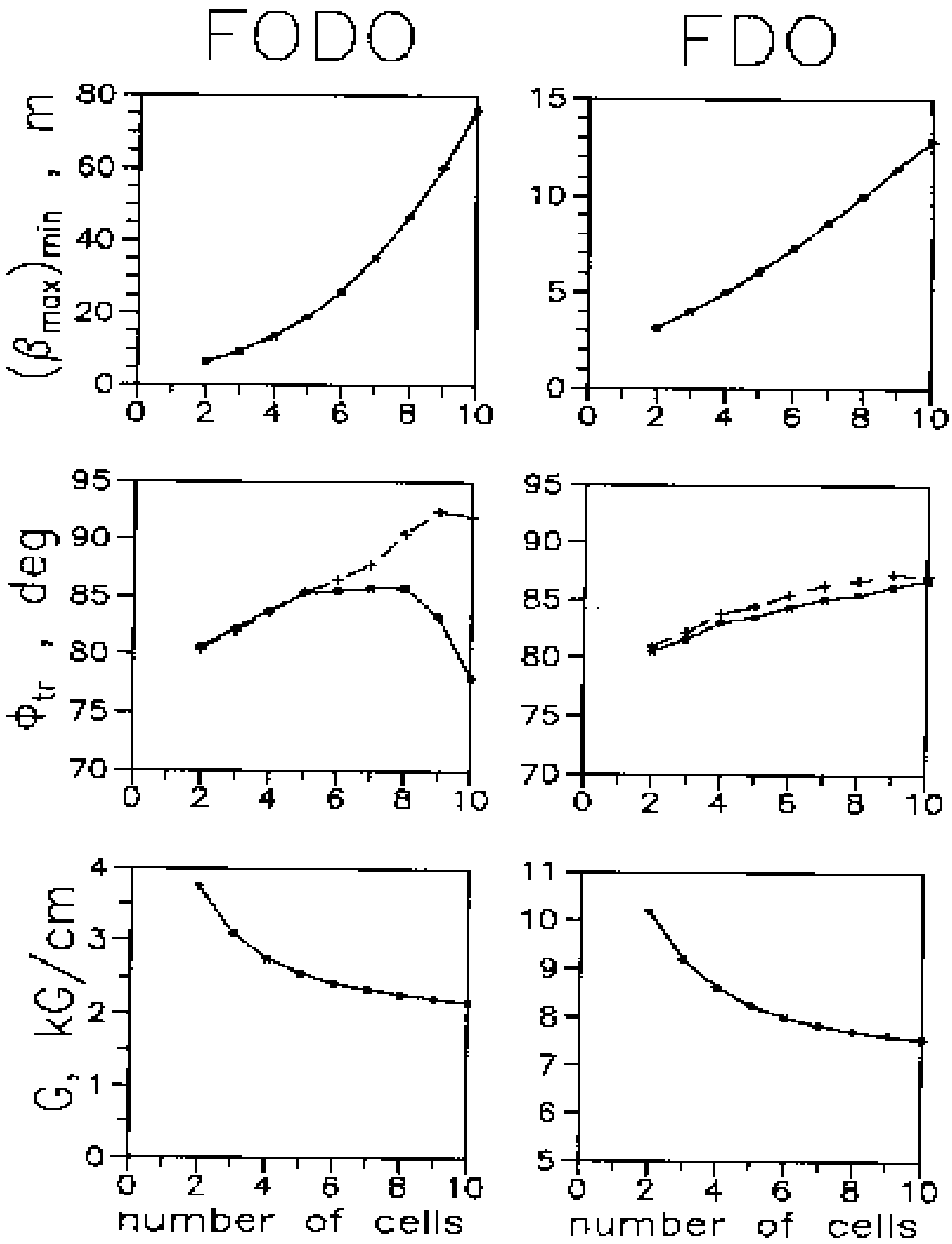

Figure 49: Comparison of FODO and FDO focusing structures.

Buncher parameters:	
number of cells	1
cell type	OCSDTL
effective field E_0T	4.6 MV/m
gap ratio α_g	0.3305
frequency	810.24 MHz
synchronous phase	- 90°
peak power	140.1 kW
drift length	2.335 m
Number of quads	4
Total transition region length	2.729 m

Table 10: Main parameters of the transition region.

8.4.7 Transition region

The main component in the transition region (TR) is a buncher cavity [16] followed by a drift space in order to reduce the phase spread of the 202.56 MHz bunches from ±13° to ±4° as it is required for the matching conditions at the entrance of the upgraded linac. The TR must contain at least four quadrupoles to match the transverse phase space parameters. The buncher length and its electric field strength are determined from the bunch length and longitudinal emittance of the 50 MeV beam. These values have been taken from experimental data (see table 7, first row). The general parameters of the transition region and the elements are listed in the table 10.

The buncher rf-power supply must have some reserve for the matching of unusual beam parameters. In our proposal the rf field can be increased approximately by 20 % which requires ≈200 kW peak power. In the table 51 the general beam matching specifications are presented.The longitudinal dynamics design of the transition region has been performed using the 90 % emittances in the 2-dimensional phase space ($\Delta\phi - \Delta W/W$). However the TR can transport 100 % of the incoming beam particles.

8.4.8 Generation of the Initial Particle Distribution

The present LINAC III beam emittance values found from experiments are presented in the first paragraph of this chapter. If we assume that real beam in the 6-dimensional phase space has an ellipsoidal structure, it is possible to reproduce this distribution using a 6- dimensional uniform distribution. Practically, for beams without intra-beam interaction two or three 6-dimensional uniform distributions will be enough to achieve a sufficiently smoothed 2-dimensional projected phase space. According to the above mentioned assumptions a model of the initial particle distribution has been created. The projections of the 6-dimensional distribution have the same value as compared to the two dimensional emittances mentioned which are listed in table reftab3n1. For further studies particle distributions consisting of the 90 % emittance is called a *main distribution*, whereas the particles outside of this ellipsoid are part of the *background distribution*. The total number of particles in the model distribution is ≈25.000.

Kinetic energy	50 MeV
Pulse current	20 mA
Longitudinal emittance (90 %) ϵ_{L}	$20.46\pi \times^{\circ} \times (810MHz) \times \%(\Delta\mathrm{W}/\mathrm{W})$
Transverse emittance (90 %, unnorm.) ϵ_{x}	$9.6\pi \times mm \times mrad$
ϵ_{y}	$4.1\pi \times mm \times mrad$
Drift tube linac	
frequency	202.56 MHz
effective gradient $\mathrm{E_0T}$ (exit)	1.57 MV/m
equilibrium phase ϕ_{s}	-25°
FODO half-period (linac exit)	46.46 cm
aperture radius	1.5 cm
structure parameters	
β_{x}	1.692 m/rad
α_{x}	- 0.01
β_{y}	0.636 m/rad
α_{y}	0.00
Upgrade linac	
frequency	810.24 MHz
effective gradient $\mathrm{E_0T}$ (entrance)	5.526 MV/m
equilibrium phase ϕ_{s}	-35°
FODO half-period (entrance)	94.62 cm
aperture radius	1.5 cm
structure parameters (entrance)	
β_{x}	3.716 m/rad
α_{x}	3.946
β_{y}	0.809 m/rad
α_{y}	- 0.908

Table 11: The 50 MeV beam matching specifications.

		Normalized emittance growth factor			
		x - x'		y - y'	
	$\beta\gamma$	rms	90 %	rms	90 %
TR exit	0.33069	1.00	1.00	1.00	1.00
Exit of cavity 1	0.43616	1.13	1.17	1.17	1.17
Exit of linac	0.60769	1.17	1.20	1.22	1.22

Table 12: Beam performance at the Upgrade Linac.

Parameter	Error range
Average accelerating field over a section	$\pm 3\,\%$
Non-uniform distribution of the	
accelerating field along a section	$\pm 3\,\%$
Inter-section distance	$\pm 100\,\mu$m
Quadrupole gradient	$\pm 3\,\%$
Quadrupole displacements:	
vertical and horizontal directions	$\pm 50\,\mu$m
longitudinal direction	$\pm 150\,\mu$m
Quadrupole axis tilt	$\pm 0.50°$

Table 13: The types of errors included in the studies.

8.4.9 Beam Dynamics Simulation

In figure 50 and figure 52 the beam envelopes (x-plane is solid line, y-plane is dashed line), the relative velocity spread $\Delta\beta/\beta$ and the phase spread $\Delta\phi$ are presented along the linac structure for the main and the total (*main + background*) distributions respectively. In figure 51 and figure 53 the phase space portraits for the main and the total distribution at certain characteristic points along the linac are plotted. The simulation has been done for all 100 % particles including the beam halo and the beam loss is less than 0.04 %. In tablereftab6n4 the beam emittance growth in the transverse phase planes is given. The main contribution to the beam emittance growth is caused by rf defocusing.

8.4.10 Accelerating Field Distortions and their Effect on Beam Parameters

The imperfections of the accelerating and focusing fields have some influence on the beam parameters. The beam dynamics has been simulated using a Monte Carlo technique for 1000 random seeds of possible deviations of linac parameters from the design values. The range of the deviations are shown in the table 13. The simulation results are shown in the Table 14, which shows that the tolerances given in the Table 13 can be achieved.

In this table the percentage of the particle loss, the emittance (90 % of particles) calculated from all random seeds for all three planes and the energy deviation of the bunch center (ΔW/W)c are listed. The subscript 0 corresponds to design values. Another source of accelerating field distortions in the long coupled cell structure is:1) a natural drop of the rf power

	Average values	The values obtained with 90 % probability
Particle loss, %	0.481	1.032
ϵ_x / ϵ_{x0} (90 %)	1.073	1.185
ϵ_y / ϵ_{y0} (90 %)	1.085	1.226
ϵ_L / ϵ_{L0} (90 %)	1.009	1.026
$(\Delta W/W)_c$, 10^{-3}	-0.176	3.819

Table 14: The results of the beam dynamics simulation.

along the long cavity containing large number of coupled cells and 2) transient beam loading and compensation. Under steady state condition a power drop along the cavity containing N cells produces accelerating field tilts which are given by [16]:

$$\frac{\Delta E}{E} = \frac{2N^2}{k^2 Q_a Q_c} \tag{9}$$

Where k is the coupling constant and Q_a and Q_c are the quality factors for the accelerating and coupling cells correspondingly. For the OCS the following ratio $Q_c \approx Q_a/4$ can be assumed. Therefore:

$$\frac{\Delta E}{E} = \frac{8N^2}{k^2 Q_a^2} \tag{10}$$

Using a MAFIA simulation a value of $Q_a \approx 2.110^3$ and $k = 0.15$ was calculated. From these values and the previous formulae we can conclude for the second and the third cavity of the linac, that the energy spread is:$\Delta E/E = 0.1\,\%$. This value is negligible for our application.

The transient beam loading causes electric field distortions on the cavity axis due to excitation of modes from the complete passband. The beam is turned on after the steady state condition of the accelerating field is achieved. In order to compensate the beam loading the generator power to resonator increases simultaneously with the beam pulse. During the transient the whole spectrum of the non-operating modes is excited while the beam loads the operating mode only. The total electric field distortion is determined as a complex sum of the electric fields of all excited modes. The total electric field on the axis and the distortions can be found analytically under the following assumptions [17]:

- for the beam loading compensation the generator power P_g is increased by the amount of power extracted from the beam P_b: $P_g = P_{g0} + P_b$
- a linear dispersion law in the range of 0 to π mode instead of sinusoidal law
- only consider a time scale larger than power propagation time along the cavity length L_c. The filling time is $\approx 1\,\mu$sec.

For the linac parameters we can obtain 2.7 % of maximum field distortion for 20 mA beam during the transient. A numerical simulation of the field distortion has been done on the base of a coupled oscillators model. The small field amplitude distortion from the cell to cell inside a section has been ignored and the average value of the field over the section has been calculated during the transient. This model shows 1.6 % for the distortion of the accelerating field amplitude. We expect that the filed distortion results in a small increase of the momentum spread for a very small part of the beam, but detailed studies of the beam dynamics are required.

Part	Section	E0T MV/m	β output	L_{sec} m	L_{dr} m	G kG/cm	P_{cu} kW	P_b kW
Transition region					0.200[1]			
	Buncher	4.6	0.31397	0.174	2.355	2.6158	140.1	-
						1.8620		
						2.2392		
						2.1529		
Cavity 1	1	5.526	0.31857	0.707	0.239	2.4800	757.7	64.03
	2	5.536	0.32765	0.727	0.246	2.4800	774.4	65.97
	3	5.538	0.33665	0.747	0.252	2.4800	793.3	67.81
	4	5.528	0.34555	0.767	0.259	2.4800	811.3	69.47
	5	5.501	0.35433	0.786	0.265	2.4800	827.4	70.90
	6	5.460	0.36297	0.806	0.272	2.4800	841.3	72.08
	7	5.428	0.37145	0.824	0.278	2.3949	858.4	73.33
	8	5.371	0.37978	0.843	0.284	2.2841	867.5	74.19
	9	5.310	0.38792	0.861	0.290	2.4000	875.4	74.92
	10	5.246	0.39588	0.879	0.296	2.2590	882.9	75.53
Cavity 2	1	5.344	0.40512	1.199	0.228	2.3700	1235	105.0
	2	5.400	0.41564	1.230	0.234	2.3700	1260	108.8
	3	5.458	0.42611	1.261	0.239	2.3700	1287	112.8
	4	5.524	0.43652	1.292	0.245	2.3700	1319	116.9
	5	5.574	0.44687	1.323	0.251	2.3700	1345	120.8
	6	5.622	0.45713	1.353	0.257	2.3700	1370	124.6
Cavity 3	1	5.491	0.46714	1.383	0.262	2.3700	1310	124.4
	2	5.521	0.48652	1.412	0.267	2.3700	1329	127.7
	3	5.566	0.48652	1.440	0.273	2.3700	1355	131.3
	4	5.603	0.49600	1.468	0.278	2.3700	1378	134.8
	5	5.631	0.50500	1.496	0.283	2.3700	1398	138.0
	6	5.675	0.51475	1.524	-	2.3700	1426	141.7

Table 15: Summary of parameters for the high energy part of the LINAC III .
(1) distance to the last quadrupole of the LINAC III .

8.4.11 Summary of Beam Dynamics Design

A detailed list of the parameters for the high energy part of the LINAC III above 50 MeV is presented in table 15.

In table 14 the following definitions are used: E_0T is the effective accelerating field; L_{sec} is the section length; L_{dr} is the drift space between the sections; G is the gradient of quadrupole located downstream of the section; P_{cu} is the power loss in the copper surface of the section; P_b is the power transmitted to the beam in the section. In order to keep the total power consumption in each cavity less than 9 MW the maximum possible electric field in the first and third cavity has been reduced by a factor of 0.984 and 0.967 respectively. The effective magnetic length for all quadrupoles is equal to 8.2 cm in the beam dynamics simulation. The total number of quads is 26.

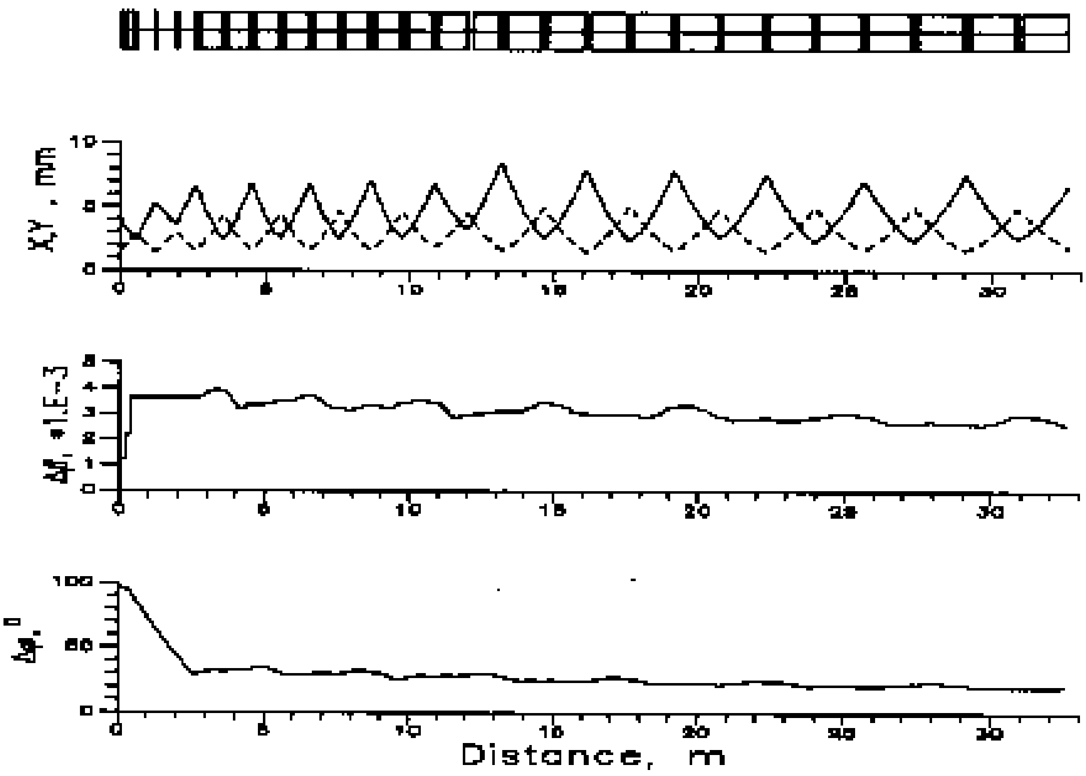

Figure 50: Beam envelopes along the linac (90 % emittance).

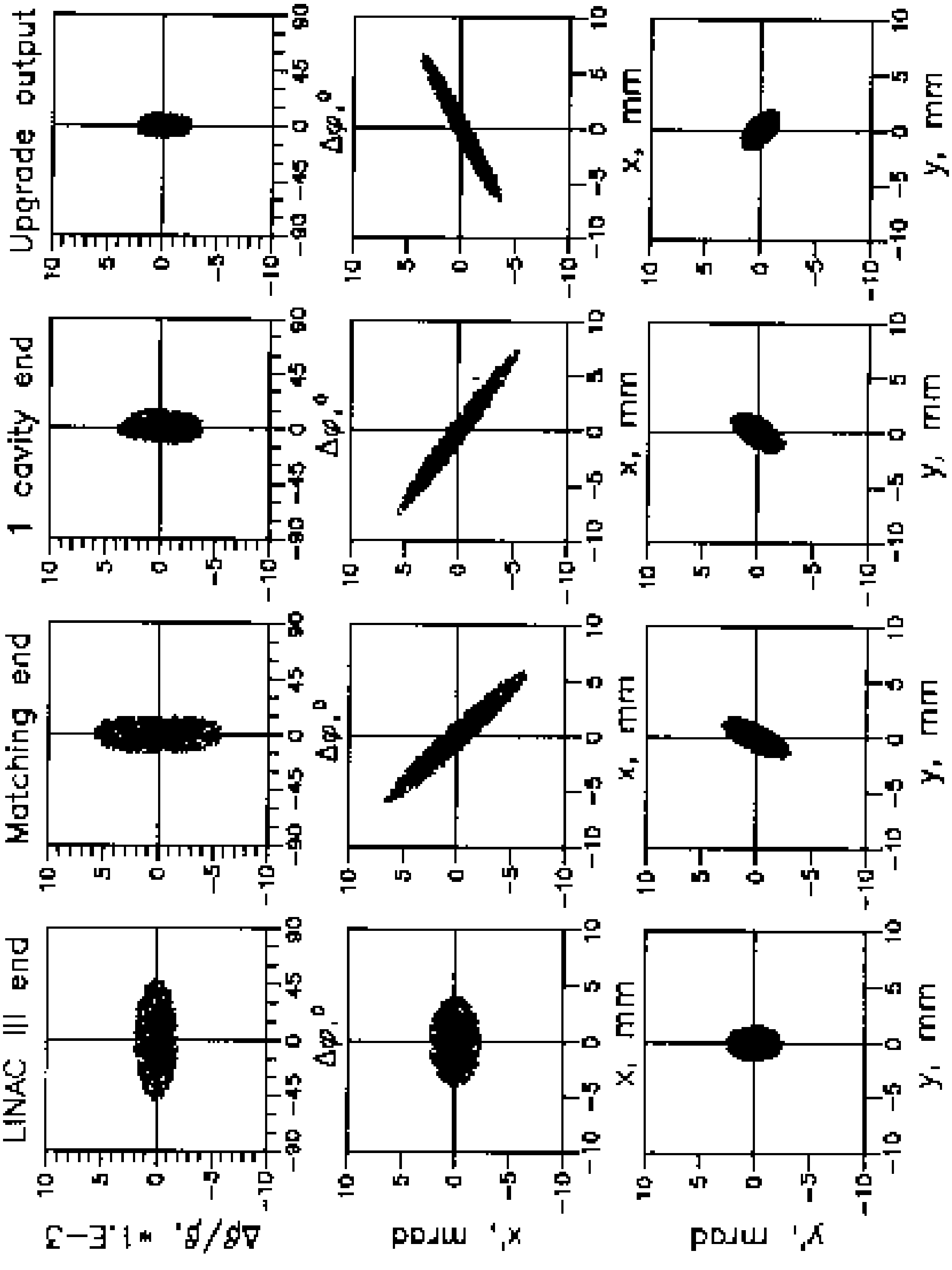

Figure 51: Beam Phase portraits (90 % emittance).

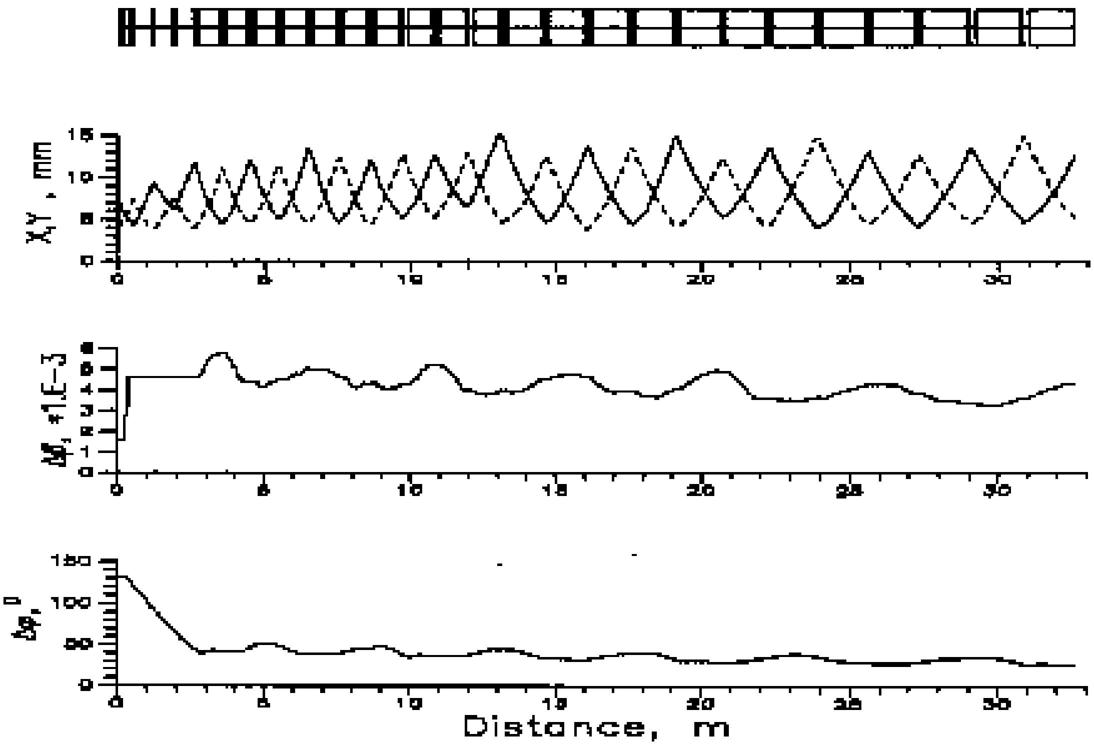

Figure 52: Beam envelopes along the linac (90 % emittance).

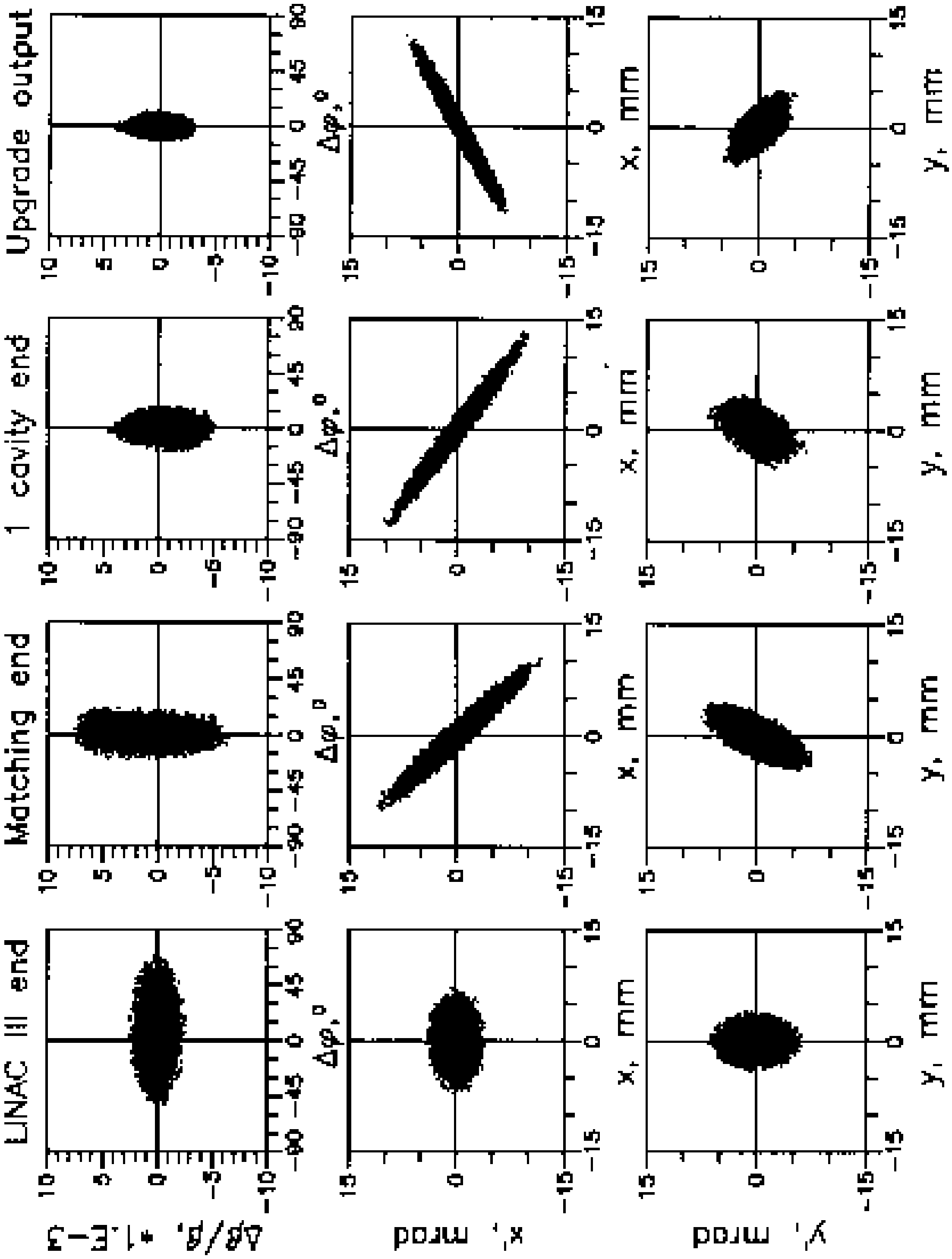

Figure 53: Beam envelopes along the linac (90 % emittance).

8.5 Radio Frequency Power System

8.5.1 Power Requirements

The 810 MHz Linac III upgrade high power rf system consists of three high power klystron and modulator systems. The copper loss and beam power for each of the three modules and the matching cavity are shown in table 15. Table 16 gives a more complete specification for the power requirements, which takes into account additional items (waveguide loss and reserve for feedback loop regulation). This adds up to 11.5 MW total peak power required for the present design. For example, a Litton L-5859 klystron specification together with the Linac III upgrade requirements are shown in Table 17. Since the peak power requirement for the Linac III upgrade is slightly below the nominal klystron rating, the Litton L-5859 klystron should be an adequate power tube. The RF power requirement for the transition section is only 200 kW which can be supplied by different today available tubes. The WR975 waveguide lines will

Typical power, accelerating 20 mA beam	9.8 MW
Waveguide run (WR 975), VSWR	0.65 MW
10 % for feedback loop regulation	1.05 MW

Table 16: Power specifications for the LINAC III upgrade program.

Parameter	Klystron specification	Linac requirements
Peak power output	12 MW	11.5 MW
Pulse length	125 msec	60 msec
Pulse repetition rate	15 Hz	1 Hz
Duty factor	0.1875 %	0.006 %
Average RF power	22.5 kW	0.69 kW
Efficiency	50	
Gain	50 db	
Voltage	170 kV	170 kV
Current	141 A	141 A
RF output	WR975 waveguide	

Table 17: L-5859 klystron specifications and linac requirements.

transport RF power from the klystron to the accelerator. A total length of the waveguide system for three RF stations is about 80 m. Waveguide lines include directional couplers and cavity vacuum windows. Careful design of the transmission line between the klystron and the cavity is necessary. Microwave windows should be placed at the minima of the VSWR in both the klystron and the coupler. The reflection during cavity field build-up should present a low impedance to the klystron output gap.

8.5.2 The RF Modulator

The Fermi lab RF modulator specifications along with the Linac III upgrade requirements are shown in Table 18. The main difference is the average power requirement which is approximately a factor of 30 lower, which decreases the DC power supply. The number of PFN (pulse forming network) sections can be reduced by a factor of two, due to the shorter RF pulse. The main

Parameter	Fermi lab modulator	Linac requirements
Peak power	24 MW	24 MW
Voltage	170 kV	170 kV
Current	141 A	141 A
Pulse repetition rate	15 Hz	1 Hz
Pulse length	125 μs	60 μs
Rise time	9 μs	7 μs
Fall time	18 μsec	12 μsec
Average power	50 kW	1.53 kW
Pulse flatness	$\pm 0.5\,\%$	$\pm 0.5\,\%$
Voltage regulation	$\pm 0.05\,\%$	$\pm 0.05\,\%$
DC power supply	9.0 kV	9.0 kV
DC average current	6.5 A	0.22 A
DC average power	58.5 kW	1.98 kW

Table 18: Modulator specifications and Linac requirement.

parameters calculated for the LINAC III upgrade are: 1) a load impedance of 1206 Ω; 2) a pulse transformer ratio of 20:1 and 3) a total capacitance of the PFN of 9.4 μF. The pulse transformer primary voltage is 9 kV, the charging voltage across the PFN capacitors is 18 kV and the primary current of pulse transformer is 2820 A. With L_P the primary inductance, T_{CH} the charging time of the PFN and ω the circuit resonance frequency the parameters for the charging circuit are given in table 19. The average charging current from the power supply is

I_{DC} / A	L_P / H	T_{CH} / ms	ω / 1/sec	R / Ω
2	194	135	23	225
4	48.6	68	46	110
6	21.6	45	69	75
8	12.2	34	92	56
10	7.8	27	115	45

Table 19: Calculated charging circuit parameters at different DC peak current.

0.18 A and the DC power consumption will only be 1.6 kW. The modulator consists of three main units: the PFN, the charging supply and the HV assembly, which includes the oil tank, the pulse transformer and the klystron. Figure 54 and 55 contain the schematics.

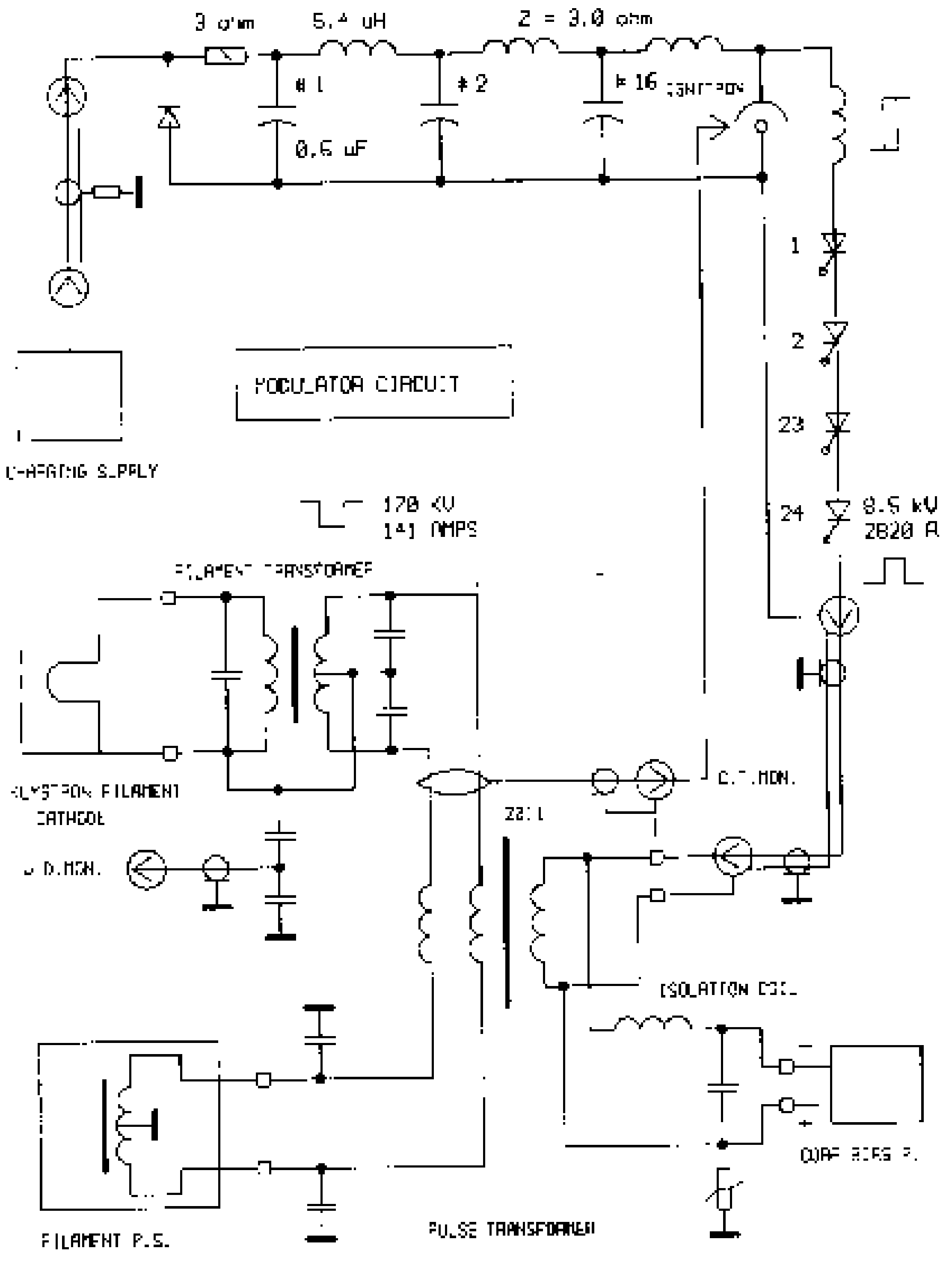

Figure 54: RF modulator circuit.

8.5.3 Low-Level RF System

The RF drive/distribution system consist of the 202.56 MHz master oscillator, a factor of four frequency multiplier, transistor preamplifiers and 810.24 MHz and 202.56 MHz reference lines. Special phase locking schemes and a motor driven mechanical, trombone type, phase shifter

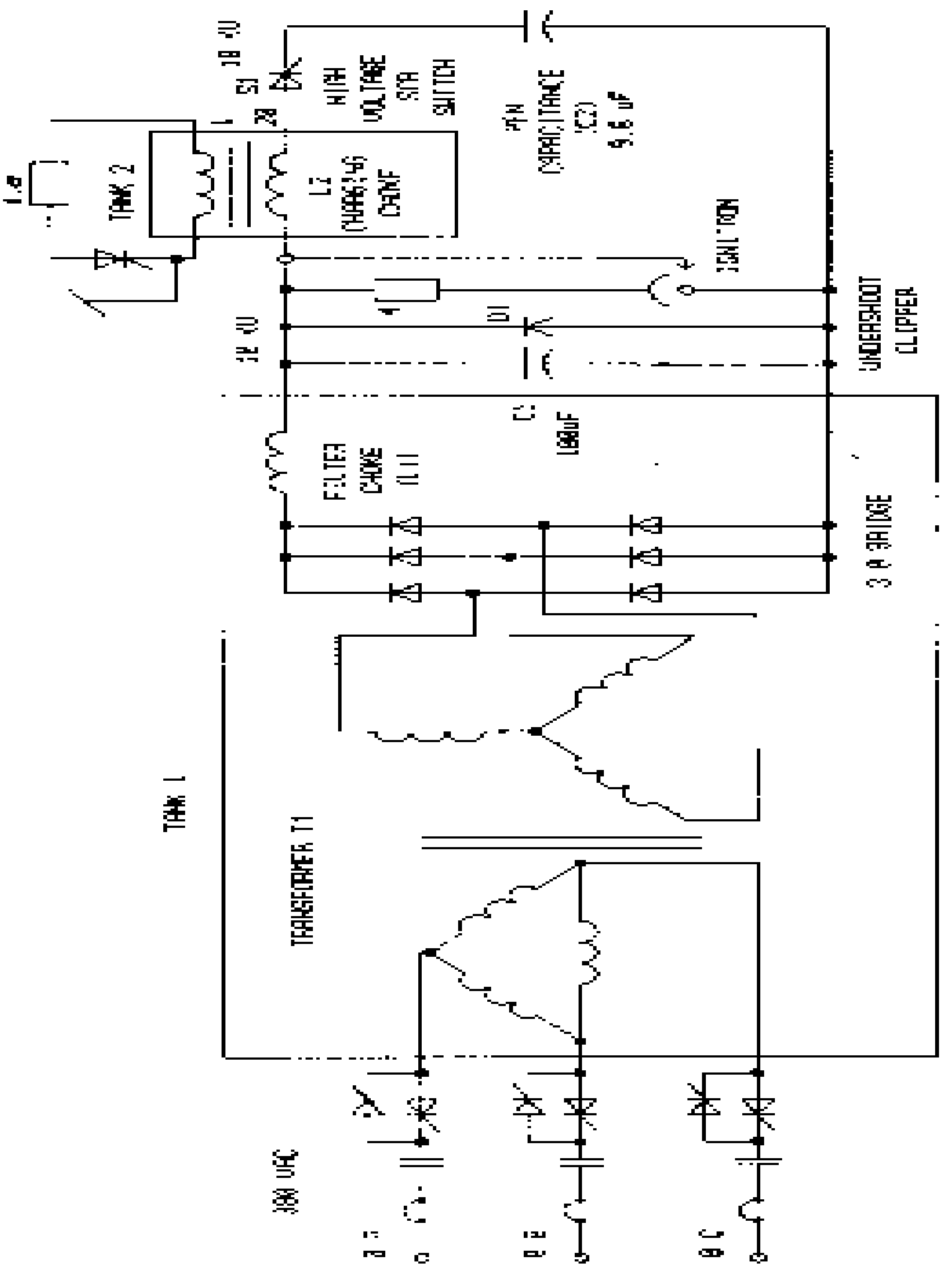

Figure 55: Simplified layout for the charging supply.

keeps the phase difference between RF signals in two reference lines constant. It provides a stable capture of the accelerated beam into the first 810.24 MHz accelerating tank. As mentioned above, the amplitude and phase of the accelerating fields within the cavities are regulated using a feedback control system. The system includes two feedback loops, one for the phase and another one for amplitude of cavity field. Both controlling loops use a feedback signal from a small measuring loop probe placed in one of the accelerating section. The system is compatible to the one installed at the LINAC III already and is described in more in [18].

8.5.4 The Cooling System

Each klystron dissipates ≈6.1 kW of heat (5 kW for the solenoid, 1 kW collector and 0.1 kW klystron body), which is 18.3 kW in total for the three stations. A separate cooling system for each station will be used for individual control of the stations. The main components are the heat exchanger, the electronically controlled valve to mix the required water temperature, water flow meters and thermometers. The full amount of heat from the secondary of the heat exchanger flows into the primary water circuit and is removed by the main laboratory cooling circuit. The temperature of the cooling water can be changed within a range of 23 - 30 C°. A temperature stabilization system is introduced into the cooling system to feedback on the measured temperature of the cavities. A remote controlled valve will keep the temperature at the output of the secondary of the heat exchanger at 33 C° with an accuracy of ±1 C°. Apart from the fast mixing valve and a comparatively fast and flexible temperature regulation system, this part is very conventional.

Aperture radius	2 cm
Beam pipe inside radius	1.7 cm
Beam pipe outside radius	1.8 cm
Maximum transversal size	20 cm
Iron core length	7.0 cm
Effective magnetic length	8.2 cm
Field gradient	3.1 kG/cm
Field nonlinearity at radius 1.5 cm	0.1 %
Number of turns per pole	20
Half-Sine pulse current	250 A
Resistance per quad	65 mW
Inductance per quad	1.0 mH
Peak voltage	600 V
Stored energy	36 J
Duty factor	0.14 %
Pulse power	2000 W
Average power	2.8 W

Table 20: Magnetic field parameters of the quadrupole lens.

8.6 Focusing System and Magnets

The focusing of the H^- beam will be provided with magnetic quadrupoles which are placed in each drift interval between the accelerating sections as well as between the cavities. The total number of quadrupoles is 26. Four of them are installed in the 50 MeV matching region between the existing LINAC III and the new part. The quadrupoles are powered with pulsed power supplies. Two options for the repetition rate are foreseen - 1 Hz for tuning and commissioning and 0.25 Hz for injection into the DESY III synchrotron.

Quadrupoles Due to the restricted space between sections and cavities the quadrupoles are operated with a gradient of 3 kG/cm with an aperture radius of 4 cm. Comparable designs have been realized for Fermi lab Linac Upgrade project [3]. Due to the significantly smaller duty cycle the design for the LINAC III upgrade could be even more compact. The main parameters for the quadrupole are shown in Table 20.

Equipment imperfections, instabilities, alignment errors and geometrical displacements will excite coherent oscillations. Overall nine standard type corrector magnets are foreseen to correct the beam orbit. With a maximum energy of 170 MeV the required dipole field is 0.026 T for a magnetic length of 7.5 cm.

8.7 Beam Instrumentation

For the successful commissioning and operation of the machine it is very important to have a good, reliable beam diagnostics. A rather delicate study should be done especially in the transition region (TR). Good beam matching has to be performed at the entrance of the upgraded part of the linac both in the transverse and the longitudinal phase space. New diagnostics for the upgraded linac will be arranged in the 2.6 m long transition region together with a buncher cavity and four regular quads, in the intersection drifts of the cavities and in the transfer line (TL) to the DESY III synchrotron (see Figure 56).

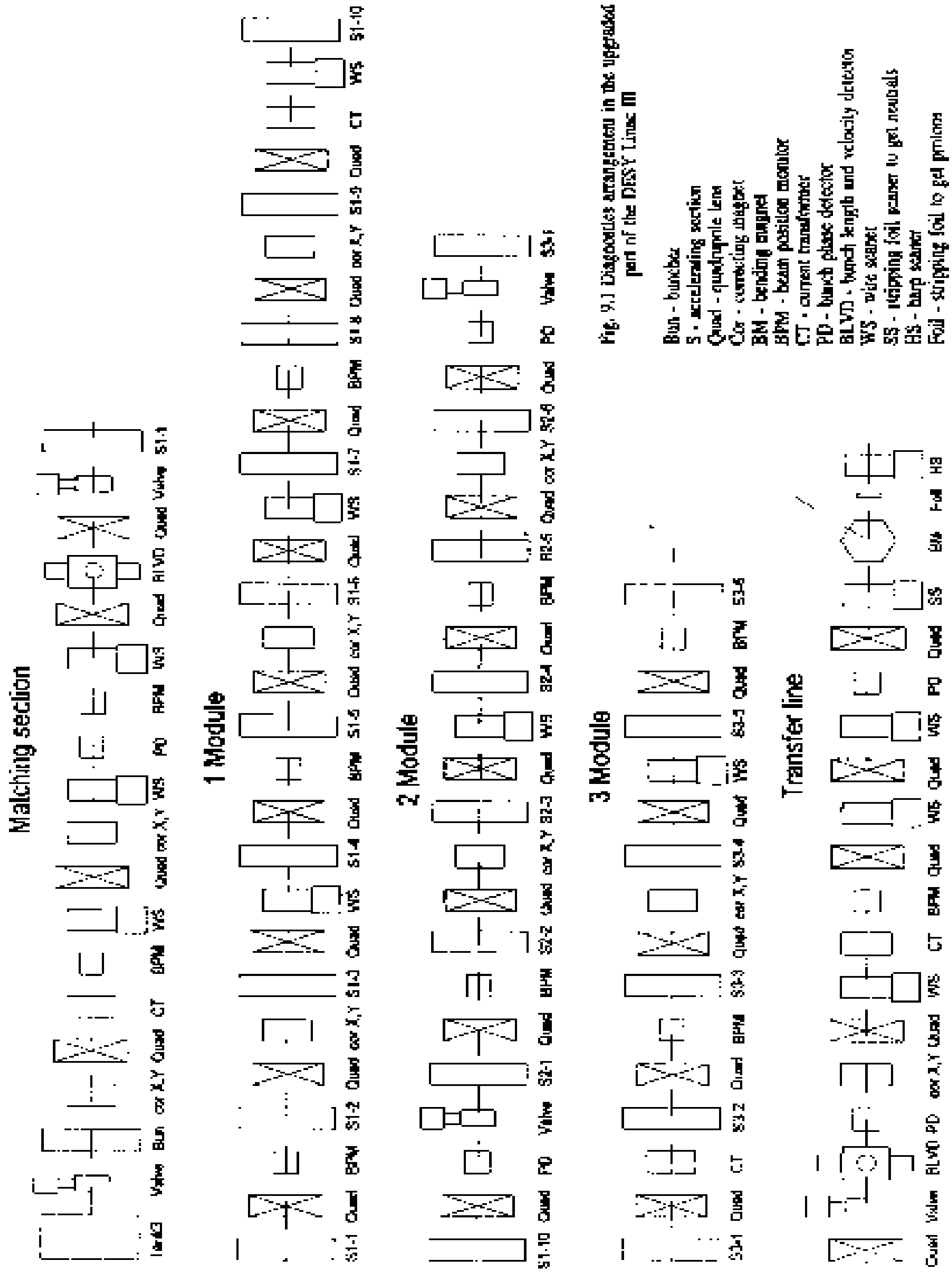

Figure 56: Diagnostics equipment in the upgraded part of the LINAC III .

N section	1-1	1-2	1-3	1-4	1-5	1-6	1-7	1-8	1-9	1-10	
L=$2\beta\lambda$/ mm	239	246	252	259	265	272	278	284	290	296	
L_{diag}/ mm	74	81	87	94	100	107	113	119	125	131	
N section	2-1	2-2	2-3	2-4	2-5	2-6	3-1	3-2	3-3	3-4	3-5
L=$3\beta\lambda/2$ / mm	228	234	239	245	251	257	262	267	273	278	283
L_{diag}/ mm	64	70	75	81	87	93	98	103	109	114	119

Table 21: The intersection drifts L and the possible length L_{diag} to be used for diagnostics equipment .

There will be 3 additional accelerating modules consisting of 10 and 2 times 6 sections. The intersection drifts of $2\beta\lambda$ are chosen for the first module and $2\beta\lambda/2$ for the second and the third module. The geometrical set-up leads to strict limitations for length of the diagnostics equipment along the beam line (see Table 21). The beam diagnostics equipment will serve for the following requirement:

- Beam current measurement;
- Beam center of mass position monitoring;
- Beam transverse position correction by means of steering magnets;
- Beam profile periodically observation along the linac in order to find out the quadrupole setting;
- Measurements aiming the transverse emittance evaluation;
- Measurement of the momentum spectrum at the linac output;
- Bunch width measurements and the longitudinal emittance restoration at the TR and TL;
- Beam-induced rf signals generation for the time-of-flight measurements.

8.7.1 Beam Diagnostics Equipment

Standard technology will be used for the beam position monitors, the wire scanners and the energy measurement. Overall nine BPM's are foreseen which are close to the nine correctors and allow to have approximately 4 corrections per 2π phase advance. The required resolution is $25\,\mu$m. The wire scanners could be similar to the harps installed right now in the LINAC III , although the resolution is not very good. Overall 11 wires are foreseen which are installed close to the waists in the horizontal or vertical plane. With the wires the transverse emittance can be determined.

A momentum spectrometer which is currently used for the 50 MeV beam provides very good momentum resolution: $\Delta p/p = 0.0526\times \Delta x$, where $\Delta p/p$ is in units of % and Δx is in units of mm. In the beam line a H^- ions are scattered on a wire and the positive ions are detected on screen behind the bending magnet. It is desirable to raise spatial resolution of the harp by adding wires or replacing the harp by wire scanners for precise detection of the momentum halo with the high energy beam.

In order to control the longitudinal emittance and matching, Beam Shape Monitors will be used [18]. In addition Bunch length and Velocity detectors will be installed, to determine the momentum of the particles [18]. This type of monitors has been successfully operated in many proton accelerators already and will be installed in the 50 MeV part of the LINAC III in 1996.

8.8 Vacuum System

Accelerating sections are combined in cavities using resonant bridge couplers. There are 10 accelerating sections, each having four resonant (accelerating + coupling) cells in the first cavity and 6 accelerating sections each having sixteen resonant (accelerating + coupling) cells in the second and third cavities 57. To decrease the number of titanium pumps a vacuum

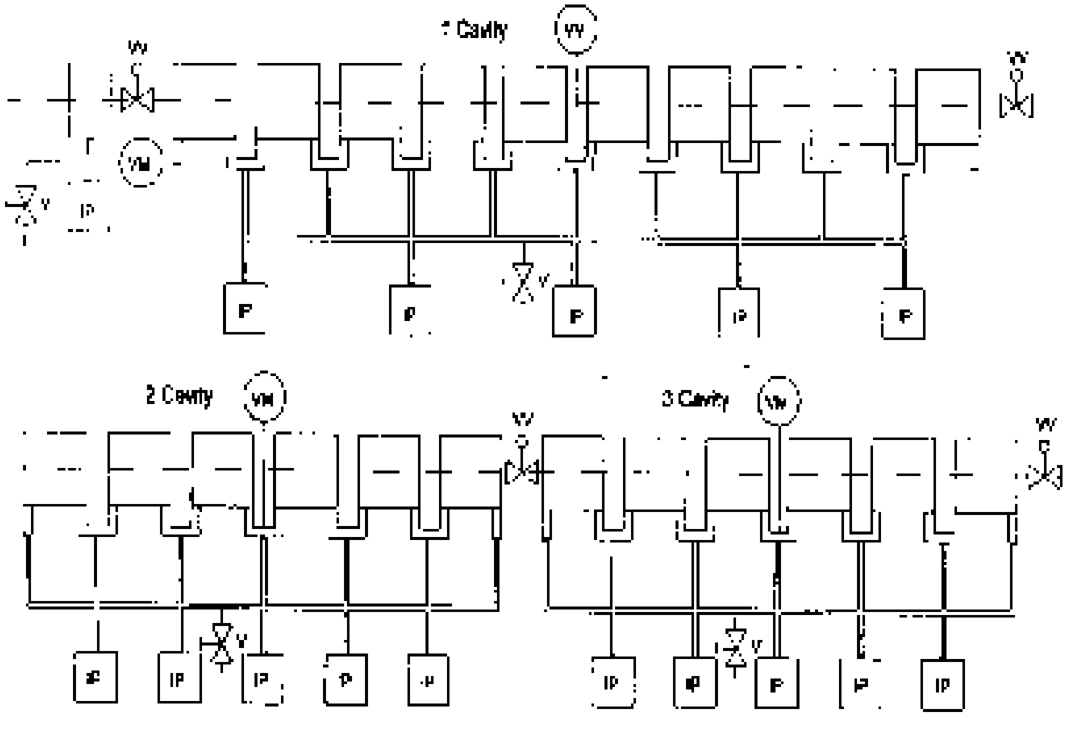

Figure 57: Vacuum system layout.

manifold will be used for each cavity. The vacuum manifold will be connected to the bridge couplers as well as to quarter wavelength shorts which have high vacuum conductivity. Five ion pumps are connected to each cavity plus one pump for the matching cavity. The manifold pipe diameter is 180 mm. The diameter of the pipes connected is 60 mm. Estimates for the vacuum conductivity of a single (accelerating + coupling) cell deliver a value 85 l/s. The effective pumping speed will therefore be ≈ 10.6 l/s. With the out gassing rate of a single cell of approximately $2.6 \cdot 10^{-7}$ l·torr/sec the calculated pressure is $2.5 \cdot 10^{-8}$ torr. The debuncher should operate at 202.54 MHz and allows to decrease the beam momentum spread approximately 10 times in order to fit to the ± 120 keV energy window of the synchrotron bucket.

8.9

The l… t and
matcl… large
energ… space
before… talled
after… ı-zero
disper… The
debur… pread
10 tir… n our
prelin… which
must

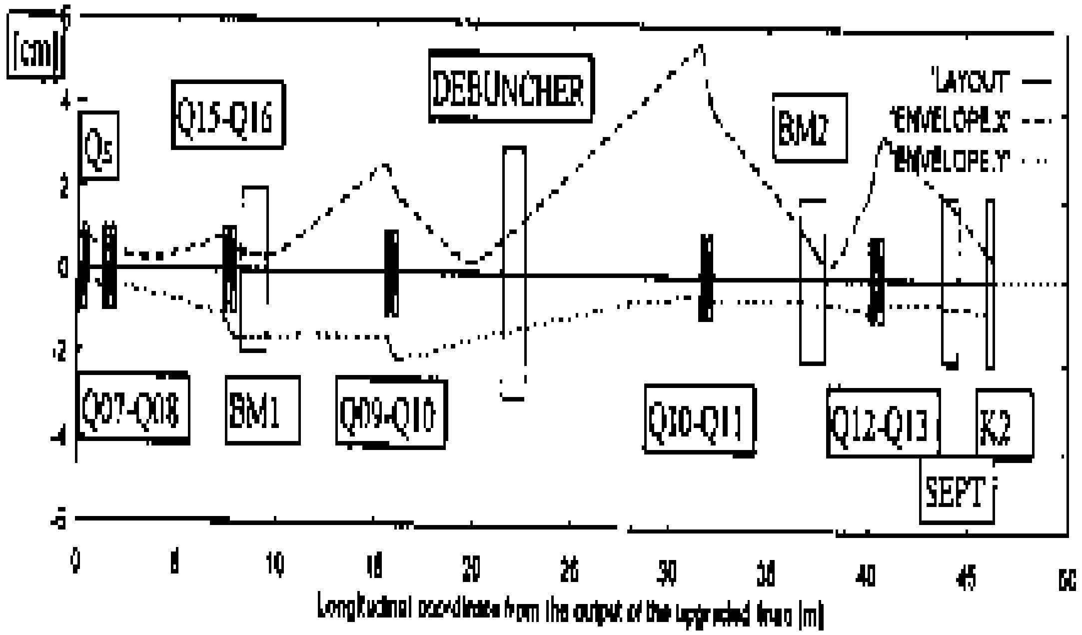

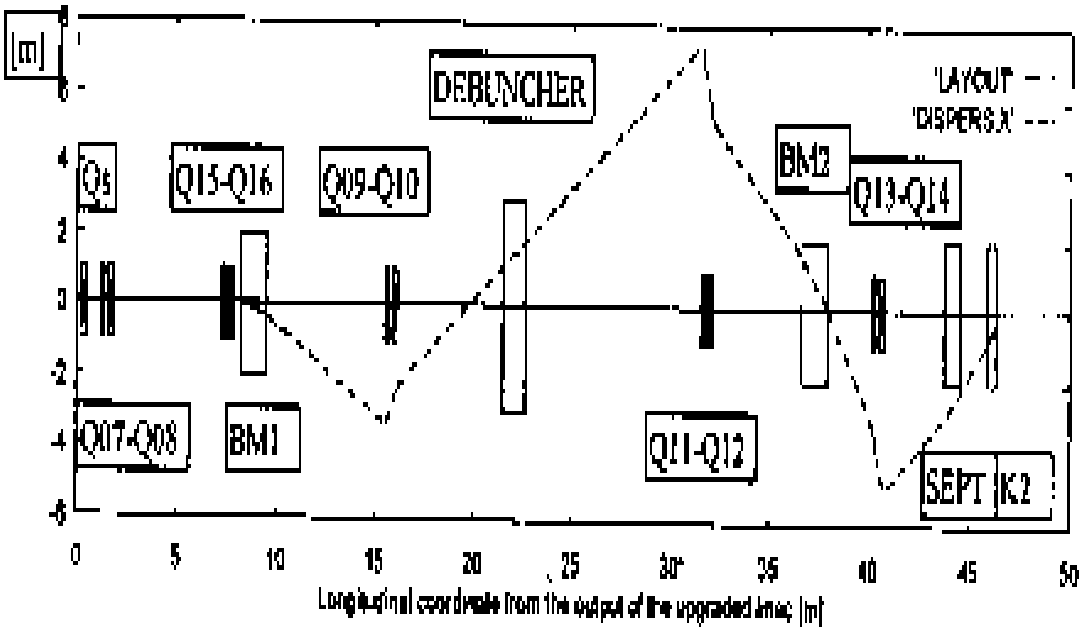

Figure 58: Beam envelopes and linear dispersion along the transport line to the synchrotron.

References

[1] *Commissioning/Operation of the Moscow Meson Factory Linac*, S.K. Esin, L.V. Kravchuk, V.A. Matveev, P.N. Ostromov and V.L. Serov, Proceedings of the 1994 Linac conference, August 1994, Tsukuba, Japan.

[2] J. H. Billen et al. A New rf Structure for Intermediate-Velocity Particles. Proc. of the 1994 Linac Conf., p. 341, 1994.

[3] Fermilab Linac Upgrade Conceptual Design Report, FNAL, November 1989.

[4] K. Jungk et al. Commissioning and First Operational Experience of the 400 MeV Linac at Fermilab. Proc. 1994 EPAC, v.1, p. 751, 1994.

[5] R. W. Garnett et al. Design and Simulation of a Bridge-Coupled DTL Structure for the 20-80 MeV Region of a Proton Linac for Accelerator Transmutation of Waste. Proc. of the 1992 Linac Conf. , p.802, 1992.

[6] Y. Yamazaki. Recent Technological Development in Accelerating Structures. Proc. of the 1992 Linac Conf., p 580, 1992.

[7] V. V. Paramonov. Accelerating Structures Study for Proton Linacs. INR Preprint (to be published).

[8] V. G. Andreev et al. The Test Results of the Experimental Module of the Second Part of the Meson Factory Linac. RTI AS USSR, Moscow, n. 25, 1976 (in Russian).

[9] S. Ignaki. Disk-and-Washer Cavities for an Accelerator. NIM A251, p. 47, 1986.

[10] V. Korchuganov et al. Status of the Siberia-2 Preinjector. Proc. of the 1994 EPAC, p.739, 1994.

[11] T. Kroc et al. Fermilab Linac Upgrade - Modul Conditioning Results. Proc. of the 1992 Linac Conf., p. 187, 1992.

[12] S. V. Isaenko et al. Preprint INR P-0372, Moscow, 1984 (in Russian).

[13] L. V. Kravchuk et al. Preprint INR P-0600, Moscow, 1989 (in Russian).

[14] S. V. Isaenko et al. Preprint INR P-0608, Moscow, 1989 (in Russian).

[15] Yu. V. Bylinski et al. Moscow Meson Factory Accelerating Structure Tuning. 1988 European Particle Accelerator Conference (Rome). Proc., Singapore, World Scientific Publishing Co. Plc. Ltd. Vol. 2, p. 1202, 1989.

[16] E. A. Knapp et al. Resonantly Coupled Accelerating Structure for High Current Proton Linacs. IEEE Transactions on Nuclear Sciences, p. 159 - 165, June 1965.

[17] L. L. Filipchikov. Beam Loading Study in Proton Linacs. Thesis for Candidate Degree. Moscow, 1974.

[18] Yu. V. Bylinski, A. V. Feschenko, P. N. Ostroumov. Longitudinal Emittance Measurement of the 100 MeV Proton Beam. Proc. of the PAC91, Chikago, Il, USA, 1991.

9 Conclusions

by F. Willeke

The studies performed in the last months may be summarizes as follows:
The layout of the HERA colliding beam interaction regions can be upgraded by means of new and unconventional magnets and focusing concepts. A first feasibilty study showed, that such magnets can be provided and operated with a reasonable effort. The maximum improvement factor compared to the luminosity which can be presently achieved amounts to about four. The most aggressive design requires machine magnets to be introduced in the available aperture inside the colliding beam detectors. The impact of such a magnet on the performance of the detector has been studied. The detector performance will be degraded but this will reduce the advantage of higher luminosity only slightly. The synchrotron radiation background conditions will become somewhat more stringent but are believed to be tolerable. The effect on auxiliary systems such as luminosity monitors are severe and optimum solutions remain to be found.

For the proposed new lattice, the design proton beam brightness parameters are assumed. The luminosity could profit -though only moderately- from an increase of the beam brightness by an upgrade of the accelerator chain to avoid space charge limitations in the DESYIII synchrotron. The studies of beam brightness limitation in DESYIII are inconclusive so far. Nevertheless, a feasibility study for an upgrade of LINACIII has been performed, which shows that the kinetic energy of the proton injection energy of DESYIII can be increased by a factor of three. In view of the large effort for such a linac upgrade it should be considered as an additional option which might become more important if the design beam brightness in HERA cannot be achieved.